

DIFFERENTIATED CHAOS IN PHASES AND  
PHASE BOUNDARIES,  
OVERFRUSTRATED/UNDERFRUSTRATED  
REPRESSED/INDUCED SPIN-GLASS ORDER,  
ASYMMETRIC PHASE DIAGRAMS, AND CRITICAL  
PHASES IN SPIN-GLASS SYSTEMS

by

EFE İLKER

Submitted to the  
Graduate School of Engineering and Natural Sciences  
in partial fulfillment of the requirements  
for the degree of

Doctor of Philosophy

in

Physics

Sabanci University

July, 2015

Sabancı University  
Graduate School of Engineering and Natural Sciences

This is to certify that I have examined this copy of a doctoral dissertation by

EFE İLKER

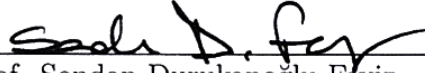
and have found that it is complete and satisfactory in all respects,  
and that any and all revisions required by the final  
examining committee have been made.

Chair of Supervisory Committee: Prof. A. Nihat Berker:

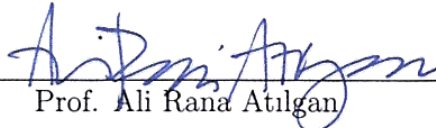
Reading Committee:



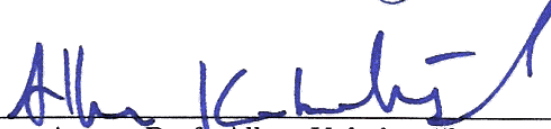
Prof. A. Nihat Berker



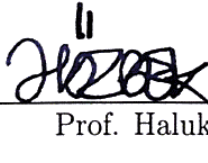
Prof. Sondan Durukanoglu Feyiz



Prof. Ali Rana Atilgan



Assoc. Prof. Alkan Kabakcioglu



Prof. Haluk Ozbek

Date: July 24, 2015

© EFE İLKER 2015  
All Rights Reserved

## ABSTRACT

Spin-glass problems continue to fascinate with new orderings and phase diagrams under frustration and ground-state entropy. In this thesis, new types of spin-glass systems are introduced resulting in a rich information on these complex structures and novel orderings. We realized that in spin-glass systems, frustration can be adjusted continuously and considerably, without changing the antiferromagnetic bond probability  $p$ , by using locally correlated quenched randomness, as we demonstrate on hypercubic lattices and hierarchical lattices. Such overfrustrated and underfrustrated Ising systems on hierarchical lattices in  $d = 3$  and  $d = 2$  are studied by a detailed renormalization-group analysis. A variety of information about the effects of frustration in spin-glass systems is obtained including evolution of phase diagrams, destruction of orderings, chaotic rescaling behavior, and thermodynamic properties. Our results are suggestive for hypercubic lattices.

Furthermore, spin-glass phases and phase transitions for  $q$ -state clock models and their  $q \rightarrow \infty$  limit the XY model, in spatial dimension  $d = 3$ , are studied. For even  $q$ , in addition to the now well established chaotic rescaling behavior of the spin-glass phase, each of the two types of spin-glass phase boundaries displays, under renormalization-group trajectories, their own distinctive chaotic behavior. We thus characterize each different phase and phase boundary exhibiting chaos by its distinct Lyapunov exponent, which we calculate. We show that, under renormalization group, chaotic trajectories and fixed distributions are mechanistically and quantitatively equivalent. The phase diagrams for arbitrary even  $q$ , for all non-infinite  $q$ , have a finite-temperature spin-glass phase. Furthermore, the spin-glass phases and the spin-glass-paramagnetic phase boundaries exhibit universal fixed distributions, chaotic trajectories and Lyapunov exponents, independent of  $q$ . In the XY model limit, our calculations indicate a zero-temperature spin-glass phase.

On the other hand, very distinctive orderings and phase diagram structures are found for odd  $q$ . These models exhibit asymmetric phase diagrams, as is also the case for quantum Heisenberg spin-glass models. No finite-temperature spin-glass phase occurs. For all odd  $q \geq 5$ , algebraically ordered antiferromagnetic phases occur. All algebraically ordered phases have the same structure, determined by an attractive finite-temperature sink fixed point where a dominant and a subdominant pair states have the only non-zero Boltzmann weights. The phase transition critical exponents quickly saturate to the high  $q$  value.

Finally, the diffusive dynamics on non-equilibrium systems are discussed. In general, the effects of microlevel motions are observed indirectly in the macroworld, hence observables that are less sensitive to microlevel randomness can be obtained with fewer parameters. Molecular dynamics simulations are extensively used on the investigation of many body systems or specific molecules interacting with many body environment under the effect of thermodynamics. We work on two different problems: In the first study, we demonstrate a scheme projecting continuous dynamical modes on to a discrete Markov State Model and analyze cw-ESR spectrum of a spin label attached to a macromolecule undergoing an arbitrary (but Markovian) rotational diffusion. In the second study, we generate the statistics and calculate the energetics of the dominant surface diffusion mechanisms and observe growth modes on nanoscale bimetallic synthesis.

Keywords: Spin glasses. Order in the presence of frozen disorder. Chaos under scale change. Critical phases and phase diagram reentrance. Renormalization-group theory. Macromolecule rotational diffusion. Nanoscale bimetallic synthesis.

## ÖZET

Spin camı problemleri, bunalım ve sıfır sıcaklık entropisinden kaynaklanan yeni düzenlerle ve faz diyagramlarıyla ilgi çekmeye devam etmektedir. Bu tezde, bu sistemlerin karmaşık yapılarıyla ilgili çeşitli bilgiler ve daha önce rastlanmamış düzenler ortaya koyan yeni spin camı sistemleri önerilmiştir. Spin camı sistemlerinde, çalışmamızda hiperkübik ve hiyerarşik örgülerde gösterdiğimiz gibi, bağ yoğunlukları değiştirilmeden yöresel olarak ilişkili bir biçimde dağıtılmış donmuş düzensizlik kullanılarak bunalım sürekli bir biçimde ve istenen düzeyde değiştirilebilir. Bu tarz altbunalımlı ve üstbunalımlı Ising spin camı sistemleri 3-boyutlu ve 2-boyutlu hiyerarşik örgülerde renormalizasyon grubu analiziyle incelemeye alınmıştır. Sonuç olarak, spin camı sistemlerinde bunalımın faz diyagramları, düzen, kaotik ölçeklenme davranışı ve termodinamik özellikler üzerindeki etkileriyle ilgili birçok yeni bulgu elde edilmiştir.

Ayrıca,  $q$ -durumlu saat modeli ve XY modeli limiti ( $q$  sonsuza giderken) spin camı fazları ve faz geçişleri incelenmiştir. Çift  $q$  değerleri için, spin camı fazındaki kaotik ölçeklenme davranışına ek olarak spin camı faz hudutlarında (spin camı-paramanyetik ve spin camı-ferromanyetik) farklı iki tip kaotik ölçeklenme davranışı gözlemlenmiştir ve her birinin Lyapunov üsteli hesaplanmıştır. Renormalizasyon grubu dönüşümleri altında ölçeklenen etkileşimlerin izlediği kaotik yolun ve bir ölçekte sistem üzerinde dağılımların mekaniksel ve niceliksel olarak eş olduğu gösterilmiştir. Hesaplanan faz diyagramlarına göre bütün sonlu çift  $q$  değerleri için bir sıfır üstü sıcaklık spin camı fazı var olmaktadır. Spin camı fazları ve spin camı-paramanyetik faz çizgileri bütün  $q$  değerleri için evrensellik göstermektedir. XY modeli limitindeki davranış ise sıfır derece spin camı fazını işaret etmektedir.

Öte yandan, tek  $q$  değerleri için, birçok kendine özgü faz davranışları ve faz diyagramları gözlemlenmiştir. Bu modeller için faz diyagramları kuantum Heisenberg spin camı sistemlerinde olduğu gibi asimetrik ve sıfır üstü sıcaklık spin camı fazı oluşmamaktadır. Bütün tek  $q \geq 5$  değerleri için, cebirsel antiferromanyetik fazlar

oluşmaktadır. Bütün bu fazlar iki farklı komşu etkileşme enerjisinin kademeli olarak baskın olduğu bir sıfır üstü sıcaklık sabit noktasıyla belirlenmektedir. Kritik üsteller  $q$  artarken hızlı bir biçimde yüksek  $q$  değerlerine ulaşmaktadır.

Son olarak, dengede olmayan sistemlerin dinamiği incelenmiştir. Mikro düzeydeki hareketler makro dünyada genel olarak dolaylı yoldan gözleendiği için, mikro düzeydeki raslantısallığa daha az hassas olan gözlemlenebilir özellikler daha az parametreyle elde edilebilir. Moleküler dinamik benzetimleri çok parçacıklı sistemlerde ve bazı özel moleküllerin çok parçacıklı çevre ile etkileşimini incelemek adına yaygın olarak kullanılmaktadır. Bu bölümde iki farklı problem ele alınmıştır: İlk çalışmada uzayda sürekli olan dinamik modlar kesikli Markov modeline çevirilerek difüzyon halindeki bir makromolekül üzerindeki spin etiketinin Elektron Spin Rezonans spektrumunun benzetimi ve analizi yapılmıştır. İkinci çalışmada ise, nano ölçekli bimetalik sentezlerdeki büyüme modları ve baskın difüzyon mekanizmalarının istatistikleri ve etkin enerji değerleri elde edilmiştir.

## ACKNOWLEDGMENTS

It is a great honor to work with and complete this thesis under the supervision of Prof. A. Nihat Berker. Starting from my undergraduate years, I have benefited from his teachings, and philosophy on both science and life. Surely, his impact on my scientific understanding has been the greatest. Moreover, his encouragement, enthusiasm and personality influenced my perspective on life and on other matters, even on social sciences, social relationships, etc., therefore I would like to express my sincere gratitude for his support and mentorship.

During my doctoral studies, I also had a chance to collaborate with Prof. Söndan Durukanoglu Feyiz and learned a lot from her experience and critical thinking. I am deeply grateful to her for her support and advice whenever I needed. I would like to thank Assoc. Prof. Alkan Kabakçiođlu (Koç University) for inspiring lectures and valuable dialogues and for insightful comments on my work. I would also like to thank Prof. Alphan Sennaroglu (Koç University) for his influence on my undergraduate career, Prof. Cihan Saçlıoglu for our intriguing discussions on philosophy and science, and Asst. Prof. Deniz Sezer for the knowledge that I have gained from his lectures and private discussions.

As a PhD student at Sabancı University, I have shared many experiences and developed strong friendships with my colleagues Onur Akbal, Onur Benli, Tolga Çađlar, and İskender Yalçınkaya. I also benefited from fruitful discussions with my colleague Barış Pekerten on various subjects. Besides, it has always been a pleasure to meet and have discussions with former members of Berker group, Dr. Ozan Sarıyer, Dr. Aykut Erbaş, Dr. C. Nadir Kaplan, Dr. Burcu Yücesoy, and Dr. Can Güven. I would like to thank them for their valuable advice.

I should commemorate my grandfather, a world traveler merchant whose personality and vision has always inspired me in many aspects. And of course, I should express my gratitude to my family, my mother, my father, my brother and my extended great family for always being supportive in my decisions and everything. Finally, for Ayşe Irmak Şen, I thank you again for being the best friend.



# TABLE OF CONTENTS

<b>List of Tables</b>	<b>xii</b>
<b>List of Figures</b>	<b>xiii</b>
<b>Nomenclature</b>	<b>xix</b>
<b>Chapter 1: Introduction</b>	<b>1</b>
1.1 Critical phenomena . . . . .	2
1.1.1 Orderings and phase transitions . . . . .	2
1.1.2 Critical exponents and universality . . . . .	3
1.2 Spin glasses . . . . .	4
1.2.1 Complexity in spin glasses . . . . .	5
1.2.2 Systems with quenched randomness . . . . .	7
1.3 Renormalization-Group (RG) transformation . . . . .	10
1.3.1 RG transformation in $d = 1$ . . . . .	11
1.3.2 Migdal-Kadanoff approximation and hierarchical lattices . . . . .	14
1.3.3 Calculation of phase diagrams . . . . .	16
1.3.4 Calculation of thermodynamic properties . . . . .	16
1.3.5 RG transformation of systems with quenched randomness . . . . .	18
1.4 Overview of thesis . . . . .	20
<b>Chapter 2: Controlling Frustration and Chaos in Spin Glasses</b>	<b>22</b>
2.1 Introduction . . . . .	23
2.2 Overfrustrated and underfrustrated spin-glass systems on hypercubic lattices and hierarchical lattices . . . . .	26
2.2.1 Stochastic Frustration, Overfrustration, and Underfrustration on Hypercubic Lattices . . . . .	26

2.2.2	Renormalization-Group Transformation, Quenched Probability Convolutions by Histograms and Cohorts . . . . .	27
2.2.3	Stochastic Frustration, Overfrustration, and Underfrustration on Hierarchical Lattices . . . . .	29
2.2.4	Determination of the Phase Diagrams and Thermodynamic Properties . . . . .	32
2.3	Calculated phase diagrams for overfrustration and underfrustration in $d = 3$ and $d = 2$ . . . . .	32
2.4	Chaos in the Spin-Glass Phase Triggered by Infinitesimal Frustration	35
2.5	Entropy, Short- and Long-Range Order in Overfrustrated and Underfrustrated Spin Glasses . . . . .	41
2.6	Conclusion . . . . .	44
<b>Chapter 3: High <math>q</math>-State Clock Spin Glasses</b>		<b>50</b>
3.1	Introduction . . . . .	51
3.2	The $q$ -state clock spin-glass model and the renormalization-group method . . . . .	52
3.3	Calculated phase diagrams for $d = 3$ $q$ -state clock and XY spin glasses . . . . .	55
3.4	Stable fixed distribution and chaotic renormalization-group trajectory of clock spin-glass phases . . . . .	57
3.4.1	Stable fixed distribution . . . . .	57
3.4.2	Chaotic renormalization-group trajectory . . . . .	59
3.4.3	Equivalence of the chaotic renormalization-group trajectory and the quenched probability fixed distribution . . . . .	61
3.5	Unstable fixed distributions and chaotic renormalization-group trajectories of the clock spinglass-paramagnetic and spinglass-ferromagnetic boundaries . . . . .	61
3.5.1	The spinglass-paramagnetic phase boundary . . . . .	62
3.5.2	The spinglass-ferromagnetic phase boundary . . . . .	62
3.6	Conclusion . . . . .	65

<b>Chapter 4:</b>	<b>Odd <math>q</math>-State Clock Spin Glasses</b>	<b>69</b>
4.1	Introduction . . . . .	70
4.2	The odd $q$ -state clock spin-glass model and the renormalization- group method . . . . .	70
4.3	Calculated phase diagrams for odd $q$ -state clock spin glasses in $d=3$	74
4.4	Algebraically ordered phases, finite-temperature renormalization- group sinks, and ground-state entropy . . . . .	78
4.5	Conclusion . . . . .	82
<b>Chapter 5:</b>	<b>Diffusive Dynamics in Non-equilibrium Systems</b>	<b>87</b>
5.1	Simulating cw-ESR Spectrum Using Discrete Markov Model of Sin- gle Brownian Trajectory . . . . .	89
5.1.1	Introduction . . . . .	89
5.1.2	Markov State Model for diffusion . . . . .	91
5.1.3	Isotropic rotational diffusion in discrete form . . . . .	93
5.1.4	Isotropic rotational diffusion in continuous form . . . . .	94
5.1.5	Reduction from continuous space to discrete coordinates . . . . .	96
5.1.6	Extension to other coordinates . . . . .	98
5.1.7	Application to short Brownian trajectories . . . . .	103
5.1.8	Discussion and conclusions . . . . .	105
5.1.9	Appendix . . . . .	107
5.2	Growth of Bimetallic Nanoparticles: Cu-Ni . . . . .	116
5.2.1	Introduction . . . . .	116
5.2.2	Computational Details . . . . .	117
5.2.3	Results . . . . .	119
5.2.4	Relaxation of non-equilibrium nanostructure . . . . .	130
5.2.5	Conclusion . . . . .	132
5.2.6	Supporting Information . . . . .	133
<b>Chapter 6:</b>	<b>Conclusion</b>	<b>139</b>
<b>Vita</b>		<b>142</b>

## LIST OF TABLES

3.1	Dominant potentials in the asymptotic fixed distribution of the phase boundary between the spin-glass and ferromagnetic phases of the $q = 6$ clock model in $d = 3$ . . . . .	64
4.1	Antiferromagnetic critical fixed-point potentials $V(\pi(q-1-2n)/q)$ , critical exponents $y_T$ , and corresponding relevant eigenvectors of different odd $q$ -state clock models. . . . .	82
5.1	Average computation times $t_{av}$ and standard deviations $\sigma_t$ over 5 runs for calculation of spectra with $(\theta, \phi)$ diffusion. . . . .	111
5.2	Average computation times $t_{av}$ and standard deviations $\sigma_t$ over 5 runs for calculation of spectra with $(\theta, \phi, \psi)$ diffusion. . . . .	112
5.3	Energetics of adsorption (in eV) on the corner of nanocrystal, i.e., (111) facet, with main sites of adsorption (fcc). . . . .	124
5.4	Calculated activation energy barriers (in eV) on the corner of nanocrystal and at the intersection of (111) and (100) facets with main exchange sites. . . . .	124
5.5	Calculated activation energy barriers (in eV) on the corner of Ni nanocrystal when its (111) facets are covered by a monolayer of Cu. . . . .	125
5.6	Calculated activation energy barriers (in eV) for hopping of Cu atoms on Ni(100) surface for nano crystal. . . . .	131

## LIST OF FIGURES

1.1	The complex structure of spin glasses. . . . .	4
1.2	Frustration a) caused by geometry of the lattice in which a system with only AF interactions in a unit triangle, and b) due to competition between bonds, when there is an odd number of F bonds in a unit square. . . . .	5
1.3	A bipartite lattice divided into two sublattices A and B. . . . .	6
1.4	Sample illustration of RG flows. . . . .	11
1.5	RG transformation in $d = 1$ , with length rescaling factor $b = 2$ . . . . .	12
1.6	RG flow for $d = 1$ Ising model at zero external field. . . . .	13
1.7	The Migdal-Kadanoff RG scheme on a square lattice with $b = 2$ . . . . .	14
1.8	Construction of a hierarchical lattice with $b = 2$ , $d = 2$ [8]. . . . .	15
1.9	RG flow for $d > 1$ Ising model at zero external field. . . . .	16
2.1	Illustration of stochastic frustration, overfrustration and underfrustration in square lattices. . . . .	24
2.2	(a) Migdal-Kadanoff approximate renormalization-group transformation for the $d = 3$ cubic lattice with the length-rescaling factor of $b = 3$ . (b) Exact renormalization-group transformation for the equivalent $d = 3$ hierarchical lattice with the length-rescaling factor of $b = 3$ . (c) Pairwise applications of the quenched probability convolution. . . . .	27

2.3	(a) Migdal-Kadanoff approximate renormalization-group transformation for the $d = 2$ square lattice with the length-rescaling factor of $b = 3$ . (b) Exact renormalization-group transformation for the equivalent $d = 2$ hierarchical lattice with the length-rescaling factor of $b = 3$ . (c) Pairwise applications of the quenched probability convolution. . . . .	28
2.4	$p_{effective}$ versus $p$ for the range of underfrustration and overfrustration used in our study. . . . .	31
2.5	Calculated phase diagrams of the overfrustrated, underfrustrated, and stochastically frustrated Ising spin-glass models on hierarchical lattices in $d = 3$ and $d = 2$ . . . . .	33
2.6	Interaction at a given position in the lattice at successive renormalization-group iterations, for $d = 3$ systems with different frustrations. . . . .	36
2.7	Interaction at a given position in the lattice at successive renormalization-group iterations, for $d = 2$ systems with different frustrations. . . . .	37
2.8	The chaotic visits of the consecutively renormalized interactions $J_{ij}$ at a given position of the system, in the spin-glass phase of underfrustrated Ising models in $d = 2$ . . . . .	38
2.9	The chaotic visits of the consecutively renormalized interactions $J_{ij}$ at a given position of the system, in the spin-glass phase of underfrustrated Ising models in $d = 2$ . . . . .	39
2.10	Lyapunov exponent $\lambda$ and runaway exponent $y_R$ of the spin-glass phases of overfrustrated, underfrustrated, and stochastically frustrated Ising models in $d = 3$ and $d = 2$ . . . . .	40

2.11	The calculated entropy per site $S/kN$ and specific heat per site $C/kN$ as a function of temperature $1/J$ at fixed antiferromagnetic bond concentration $p = 0.5$ , for $d = 3$ systems with underfrustration ( $f = 0.02, 0.2, 0.5$ ), the stochastic frustration ( $f = 1 = g$ ), and overfrustration ( $g = 0.7$ ). . . . .	42
2.12	The calculated entropy per site $S/kN$ as a function of the antiferromagnetic bond concentration $p$ at fixed temperature $1/J = 0.5$ , for systems with no frustration ( $f = 0$ ), underfrustration ( $f = 0.5, 0.8$ ), the stochastic frustration ( $f = 1 = g$ ), and overfrustration ( $g = 0.8$ ) and the calculated derivative of the entropy per site $(1/kN)(\partial S/\partial p)$ as a function of the antiferromagnetic bond concentration $p$ at temperature $1/J = 0.5$ , for the stochastic frustration system ( $f = 1$ ) in $d = 3$ . . . . .	43
3.1	(a) Migdal-Kadanoff approximate renormalization-group transformation for the $d = 3$ cubic lattice with the length-rescaling factor of $b = 3$ . (b) Exact renormalization-group transformation for the equivalent $d = 3$ hierarchical lattice with the length-rescaling factor of $b = 3$ . (c) Pairwise applications of the quenched probability convolution. . . . .	53
3.2	Calculated phase diagrams of the $q = 2, 4, 6, 12$ clock spin-glass models in $d = 3$ dimensions. . . . .	55
3.3	Phase diagrams of the $q = 12, 18, 36$ clock spin-glass models in $d = 3$ dimensions. . . . .	56
3.4	The calculated transition temperatures between the spin-glass phase and the paramagnetic phase, at $p = 0.5$ , as a function of $q$ , up to very large values of $q = 720$ . . . . .	57
3.5	Asymptotic fixed distribution, under renormalization-group transformations, of the interactions in the spin-glass phase. . . . .	58

3.6	Comparison, showing the coincidence, of the chaotic visits of the consecutively renormalized interactions at a given position of the system and of the asymptotic distribution of the interactions across the system at a given renormalization-group step, for the spin-glass phase. . . . .	60
3.7	The fixed distribution and, equivalently, chaotic renormalization-group trajectory onto which the phase boundary between the spin-glass and paramagnetic phases renormalizes, for the $q = 2$ and $q = 6$ -state clock models in $d = 3$ . . . . .	62
3.8	Two different, non-coinciding strong-coupling fixed distributions: The fixed distribution and, equivalently, chaotic renormalization-group trajectory onto which the spinglass-ferromagnetic phase boundary of the $q = 2$ -state model in $d = 3$ renormalizes. . . . .	63
3.9	The fixed distribution and, equivalently, chaotic renormalization-group trajectory onto which the spinglass-ferromagnetic phase boundary of the $q = 6$ -state clock model in $d = 3$ renormalizes. . . . .	64
4.1	(a) Migdal-Kadanoff approximate renormalization-group transformation for the $d = 3$ cubic lattice with the length-rescaling factor of $b = 3$ . (b) Exact renormalization-group transformation for the equivalent $d = 3$ hierarchical lattice with the length-rescaling factor of $b = 3$ . (c) Pairwise applications of the quenched probability convolution. . . . .	71
4.2	Calculated phase diagrams of the odd $q$ -state clock spin-glass models on the hierarchical lattice with $d = 3$ dimensions. . . . .	75
4.3	Lower temperature details of the phase diagrams shown in Fig. 4.2. . . . .	77
4.4	Evolution of the quenched probability distribution under successive renormalization-group transformations. . . . .	79
4.5	Critical temperatures $1/J_C$ and critical exponents $y_T$ of the ferromagnetic and antiferromagnetic $q$ -state clock models in $d = 3$ . . . . .	80



5.1	Derivative spectra (for three different rotational diffusion rates) generated from 100,000 Brownian trajectories (for angle $\theta$ ), and calculated from MSM model are compared. . . . .	95
5.2	Simple reduction scheme from continuous to discrete coordinates for a Brownian trajectory for the s=4 MSM model. . . . .	96
5.3	Derivative spectra generated from 100,000 Brownian trajectories same as in Fig. 5.1 and calculated from MSM model with transition matrix obtained from a single Brownian trajectory are compared. . . . .	98
5.4	Derivative spectra (for three different rotational diffusion rates) generated from 20,000 Brownian trajectories (for angles $\theta, \phi$ ), and calculated from MSM model of single Brownian trajectory are compared.	101
5.5	Derivative spectra (for three different rotational diffusion rates) generated from 20,000 Brownian trajectories (for angles $\theta, \phi, \psi$ ), and calculated from MSM model of single Brownian trajectory are compared. . . . .	102
5.6	Derivative spectra (for anisotropic diffusion) generated from 25,000 Brownian trajectories (for angles $\theta, \phi, \psi$ ), and calculated from MSM model of single Brownian trajectory are compared. . . . .	103
5.7	Derivative spectra (for rotational diffusion rate $D = 10^8$ rad/s) generated from 20,000 Brownian trajectories (for angles $\theta, \phi$ ), and calculated from MSM model of single Brownian trajectory until 100 ns are compared. . . . .	104
5.8	Derivative spectra (for rotational diffusion rate $D = 10^8$ rad/s) generated from 20,000 Brownian trajectories (for angles $\theta, \phi$ ), and calculated from MSM model of 5 independent Brownian trajectories until 100 ns are compared. . . . .	105
5.9	Cu nanocrystal with (111) facets at T=0 K and T=500 K. . . . .	119
5.10	Occurrence probabilities of exchange to (100) surfaces from (111) facets for Cu-Cu, Ni-Ni, Cu-Ni synthesis. . . . .	121

5.11 Occurrence probabilities of exchange to (100) surfaces from (111) facets for Ni-Cu* synthesis. . . . .	122
5.12 Cu deposition on Cu nanocrystal with injection period a) $\Phi=10$ ps b) $\Phi=100$ ps c) $\Phi=500$ ps at $T=500$ K. Similar growth modes are obtained for Ni deposition on Ni nanocrystals (data not shown). . . . .	127
5.13 Cu deposition on Ni nanocrystal with injection period $\Phi=10$ ps and $\Phi=100$ ps at $T=500$ K. . . . .	129
5.14 Ni deposition on Cu nanocrystal with injection period a) $\Phi=10$ ps b) $\Phi=100$ ps c) $\Phi=250$ ps at $T=500$ K. . . . .	130
5.15 Dynamic transition from octopus shape to concave one and finally to fully covered original-like structure for Cu deposited Ni nanocrystals. . . . .	132
5.16 Relaxation at $T=300$ K: right after deposition process and after 180 ns. . . . .	133
5.17 Average diffusion times and standard deviations as a function of number of simulations. . . . .	134
5.18 Cumulative distribution of ratio of diffused atoms as a function of time. . . . .	135
5.19 An example of energy landscape for several atom positions. . . . .	136
5.20 Optimized energy path of a kinetic process in Cu-Cu synthesis and specified by the initial and final configurations on the right. . . . .	136
5.21 Optimized energy path for a kinetic process in Ni-Ni synthesis and specified by the initial and final configurations on the right. In this case, initial configuration is forced to be hcp by the unstability of the presumed fcc site. . . . .	137

## NOMENCLATURE

F	ferromagnetic
AF	antiferromagnetic
SG	spinglass
RG	renormalization-group
cw-ESR	continous-wave electron paramagnetic spin resonance
MD	molecular dynamics
MSM	markov state model

Chapter 1

**INTRODUCTION**

## 1.1 Critical phenomena

### 1.1.1 Orderings and phase transitions

The sudden change in the macroscopic picture of a system is known as a phase transition. In thermodynamics, this incident is observed as a singularity in the free energy and its derivatives. If a discontinuity is in the first derivative of the free energy, it is called a first-order phase transition and if a discontinuity is in higher-order derivatives of the free energy it is referred as a second-order - or critical - phase transition. The most striking reflections such as destruction of ordering, large-scale fluctuations and universality is seen in critical phenomena and thus it has become a topic of various disciplines. Liquid-gas systems, magnetic systems, and numerous other systems including connectivity between degrees of freedom can be solved in an analogy if the relevant interaction and order parameters are introduced.

Considering magnetic materials in a perfect lattice structure having an atom at each site of the lattice with an independent spin, it is clear that at sufficiently high external fields, overall spins will point the same direction, i.e., parallel to the external field. Surprisingly, collective behavior of large clusters is also seen at zero field, and this fact is understood through the phenomena of *spontaneous magnetization* which is caused by magnetic interactions between individual spins. Starting from short-range interactions, various spins may participate to a collective behavior that exhibits long-range ordering. In effect, when surveying a two-level system in which only spin states are up and down directions, the equilibrium configuration will favor a non-zero magnetization treating up and down magnetizations equivalently. Applying an infinitesimal external field will break the symmetry of spin states, hence the system will obey to be in magnetic direction forced by the external field. However, this property is lost above the critical temperature  $T > T_c$  which is also known as the Curie temperature where the double-well structure of free energy as a function of magnetization collapses into a single-well structure. Although the densities evolve continuously upon passing the critical temperature from  $T < T_c$  to  $T > T_c$  or vice versa, right at the critical point  $T = T_c$  where

the phase transition occurs, fluctuations at all length scales are observed, indicating *scale invariance* of correlations resulting in discontinuities in thermodynamic response functions.

### 1.1.2 Critical exponents and universality

Since in a phase transition thermodynamic functions exhibit singularities, it is proper to study asymptotic behaviors as power laws of its parameters. The exponents defining the asymptotic behaviors are called the *critical exponents*. Universality denotes similar critical behaviors, identical critical exponents in diverse systems. In fact, this observation is not a coincidence and can be better understood with a categorization of universality classes depending on several physical properties of the system. These properties are: *i*) symmetry of the order parameter *ii*) dimensionality of the lattice *iii*) range of interactions. Hence, regarding such effects of its constituents, it is useful to work with the simplest model in a universality class. On the other hand, the critical temperature is highly dependent on the details of interatomic interactions and cannot be categorized in such a simple manner. While the above properties determine universality classes for critical phenomena they also strongly effect long-range ordering behaviors but not necessarily in the same subcategories. In this thesis, we will be mentioning such effects by changing local structure, dimensionality, spin order parameters and observing new universality classes and diversities for spin-glass orderings and spin-glass transitions.

## 1.2 Spin glasses

Spin-glass theory came into life to validate a physical basis for problems raised by experimental peculiarities in magnetic systems. While answering some of the major concerns, its applications grew beyond its original purpose and became a new topic in statistical physics representing collective complex structures, even posing now its own questions and being innovative in its understanding. Control over these magnetic systems would mean a grand innovation on memory storage and nanotechnology. Apart from its indications on magnetic systems, spin-glass systems also provide information about similar glassy dynamics in liquid systems which have more experimental applications. In addition to that, by also being an abstract theory applicable to complex structures and networks, it is widely used in biological and neural networks, information theory, optimization problems, applications to sociology and economy, etc.

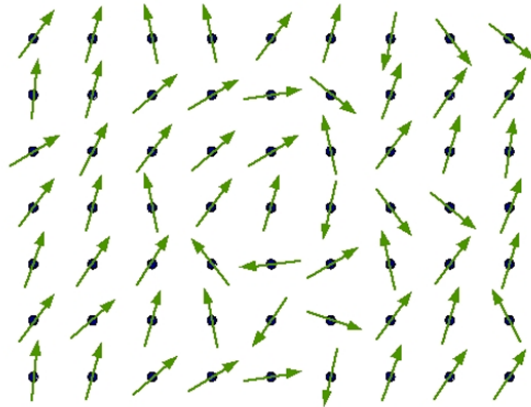


Figure 1.1: The complex structure of spin glasses.

In the figure above, we show an illustration of complex spin structure, displaying different patterns of alignments on different regions. In fact, the spin configuration is dynamic, slowly changing in time, due to large relaxation times even larger than experimental observation timescales. In return, slowly relaxing magnetization can be observed. Furthermore, these systems may have very dissimilar equilibrium configurations, also with different portions of the system being not alike. The degeneracy in free energy minima can be better seen with the notion of

ground-state entropy which can be injected into the system by bond randomness.

### 1.2.1 Complexity in spin glasses

#### Frustration and ground-state entropy

Frustration is caused by competition between interactions. Competition between interactions can emerge from geometry of the lattice itself (e.g., AF interactions in a non-bipartite lattice) or having multiple interactions which oppose in behavior. In Fig. (1.2) we have examples for such cases: frustration in a unit triangle with only AF interactions (Fig. (1.2a)) and unit squares including F and AF interactions together (Fig. (1.2b)). Evidently, these systems have many energy minimizing configurations and thus ground-state entropy. The corresponding free energy landscape with many minimum points and complicated structure is responsible for slow dynamics on reaching equilibrium, and non-equilibrium aging effects at low temperatures. In other words, the system can be trapped in a valley due to relatively high energy barriers between local minima and it can take long time to reach equilibrium state. As a consequence, we observe glassy dynamics experimentally, large relaxation times on simulational studies. Since not all bonds are satisfied due to frustration in these structures, we can only achieve a total energy  $E > N_b K$ , where  $N_b$  is the total number of bonds and  $K < 0$  is the bond energy. On the other hand, ground-state entropy can also be obtained in systems

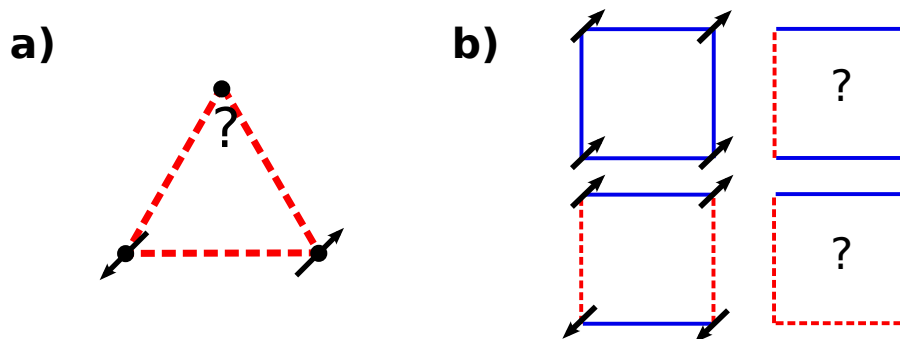


Figure 1.2: Frustration a) caused by geometry of the lattice in which a system with only AF interactions (dashed red) cannot satisfy all bonds in a unit triangle, and b) due to competition between bonds, when there is an odd number of F bonds (blue) in a unit square.



favoring all short-range interactions and  $E = N_b K$ . The Potts models and odd  $q$ -state clock models with only AF interactions in which the ground-state entropy is injected due to not having sublattice spin-reversal ( $\theta_i \rightarrow \theta_i + \pi$ ) symmetry, are examples for such systems. In addition to these, continuous spins such as XY and Heisenberg models despite having zero entropy at zero temperature, are also exhibiting high entropy once a little amount of thermal energy is introduced, i.e., a high low-temperature entropy. The amount of low-temperature entropy is one of the key figures in understanding different types of long-range ordering behaviors in these models. However, for all of these systems, the ordering behavior becomes much stronger with the increase of dimensionality of the lattice (or coordination number).

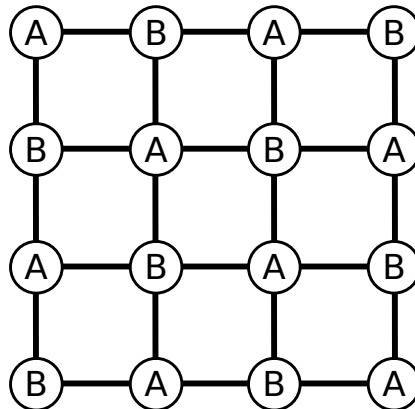


Figure 1.3: A bipartite lattice divided into two sublattices A and B. Short-range interactions are only between a site at A and a site at B. In general, for AF systems the order parameter is considered to be sublattice magnetization in which all spins are expected to be firmly aligned at ground-state. In systems lacking sublattice spin-reversal ( $\theta_i \rightarrow \theta_i + \pi$ ) symmetry, the symmetry of the order parameter is also destroyed.

### Chaos in spin glasses

Although exhibiting a collective ordering behavior, the different portions of a spin glass system do not seem alike. Accordingly, dominant interaction mechanisms for long-range ordering differ in nature on different length scales. As we will see later on, we can better understand this phenomena by *chaotic rescaling* behavior [10, 11]. This characteristic suggests that while remaining in spin-glass order,

introducing a little amount of thermal energy results complete reorganization of the overall structure. This property of spin glasses which is also known as *temperature chaos* is caused by having dissimilar configurations on a small range of free energy.

### 1.2.2 Systems with quenched randomness

In order to establish a model by concentrating on the notion of frustration through competition between bonds, quenched bond randomness on the lattice can be introduced. Evidently, in these systems there will be non-uniform interactions. A simple case can be by having randomly distributed F and AF interactions throughout the lattice equal in strength. To understand the basic features which will be implemented by such a case in contrast to uniform magnetic systems, we should first briefly overview most commonly used magnetic model, i.e., the Ising model.

#### The Ising model

Consider a lattice in which each atom is perfectly located at lattice sites in crystal structure. In magnetic systems, these atoms have an independent spin which interacts with its environment, bonding with other spins and coupling with the external field. A basic example of these systems is Ising model with nearest neighbor interactions. The Ising model Hamiltonian is given by

$$-\beta\mathcal{H} = J \sum_{\langle ij \rangle} s_i s_j + H \sum_i s_i \quad (1.1)$$

where  $H$  is the external magnetic field,  $\beta = 1/kT$ , at each site  $i$  of a lattice the spin  $s_i = \pm 1$  and  $\langle ij \rangle$  denotes that only the nearest-neighbor pair of sites are included in the summation. The exchange interaction between spins is an internal characteristic of the system and may differ in materials but what we care is its proportionality with temperature and in fact with  $-\beta$  since we deal with Boltzmann weights in equilibrium statistical physics. Thus, in our definition, the coupling coefficient  $J$  is uniform and inversely proportional to temperature. The

partition function which defines this model at equilibrium is

$$Z = \sum_{\{s\}} e^{-\beta \mathcal{H}} \quad (1.2)$$

where  $\sum_{\{s\}} = \sum_{s_1=\pm 1} \sum_{s_2=\pm 1} \dots \sum_{s_N=\pm 1}$  is the summation over all configurations. Once the partition function is determined, we may obtain thermodynamic properties as a function of  $J$  and  $H$ . We may acquire equivalent AF model for bipartite lattices, by taking  $J \rightarrow -J$  and  $H \rightarrow H^\dagger$  where  $H^\dagger$  is staggered field exerting differently on sublattices A and B (see Fig. (1.3)), i.e., applying H on sites in sublattice A while applying -H on sites in sublattice B. Now it is also clear that a spin from sublattice A has nearest-neighbor coupling with a spin from sublattice B, hence, we may consider our Hamiltonian as

$$-\beta \mathcal{H} = -J \sum_{\langle ij \rangle} s_i^{(A)} s_j^{(B)} + H \sum_i^{\{A\}} s_i - H \sum_j^{\{B\}} s_j \quad (1.3)$$

where  $\{A\}$  and  $\{B\}$  denote the summation is only over sublattices A and B. Now, taking the whole spin set  $\{s_j^B\} \rightarrow -\{s_j^B\}$  in Hamiltonian would not change anything in the partition function since  $\sum_{s_j=\pm 1} = \sum_{s_j=\mp 1}$ , thus we recover Eq. (1.1) which represents the ferromagnetic Ising model. Accordingly, we conclude that these two systems are equivalent, and will have identical thermodynamic properties, transition temperatures and critical exponents.

### The Edwards-Anderson spin-glass model

Considering the same model with quenched bond randomness, we have

$$-\beta \mathcal{H} = \sum_{\langle ij \rangle} J_{ij} s_i s_j \quad (1.4)$$

where the bonds  $J_{ij}$ 's are placed independently on the lattice according to a probability distribution. The simplest case is a bimodal distribution consisting of  $J_{ij} = J$  with probability  $1 - p$  and  $J_{ij} = -J$  with probability  $p$  where  $J > 0$ . Since bonds are randomly distributed across the lattice without any correlation, frustration will occur as presented in the previous section.

---

This model has been solved previously by RG treatment and Monte Carlo studies indicating destruction of order due to frustration at relatively lower temperatures than fully F/AF system, reentrance of phase diagrams, spin-glass phase in  $d=3$ , and no spin glass order in  $d=2$ , etc. Comparison with newly discovered spin-glass phases and novel orderings in spin-glass systems will help to understand the effects on ordering caused by microscopic properties such as types of interactions and accessible spin states and lattice structure.

### 1.3 Renormalization-Group (RG) transformation

The basic idea is to bring a mathematical tool to solve for thermodynamical properties of large systems by invariant transformations. These transformations are simply mapping of interaction parameters onto different or rescaled lattice structure while keeping macroscopic characteristics unchanged. Thus the transformation is done on the degrees of freedom by a projection operator  $\mathbf{P}(\{\mathbf{x}'_i\} | \{\mathbf{x}_i\})$  which should satisfy the condition that the partition function of two systems are equal to each other, i.e.,  $Z(\vec{\mathbf{K}}') = Z(\vec{\mathbf{K}})$  where  $\{x'_i\}$  and  $\{x_i\}$  are the set of coordinates respectively in renormalized and original systems. During a scale transformation, some of the coordinates are taken out resulting in a change in total number of particles in the system  $N \rightarrow N'$ , change in coordinates, and change of interaction strengths. The equivalence of partition functions can be written in detail as

$$\sum_{\{x\}} e^{-\beta \mathcal{H}(\vec{\mathbf{K}}, \{x\})} = \sum_{\{x'\}} \sum_{\{\sigma\}} e^{-\beta \mathcal{H}(\vec{\mathbf{K}}, \{x'\}, \{\sigma\})} \quad (1.5)$$

and performing a summation over set of degrees of freedom  $\{\sigma\}$  results in the functional form with rescaled interactions

$$\sum_{\{x\}} e^{-\beta \mathcal{H}(\vec{\mathbf{K}}, \{x\})} = \sum_{\{x'\}} e^{-\beta \mathcal{H}(\vec{\mathbf{K}}', \{x'\})}. \quad (1.6)$$

In general, the set of interactions  $\vec{\mathbf{K}}$  may grow in number when transforming into  $\vec{\mathbf{K}}'$  with unavoidable additive interactions or constants in the new functional form which is defined by

$$R(\vec{\mathbf{K}}', \{x'\}) = e^{-\beta \mathcal{H}(\vec{\mathbf{K}}', \{x'\})} = \sum_{\{\sigma\}} e^{-\beta \mathcal{H}(\vec{\mathbf{K}}, \{x'\}, \{\sigma\})} \quad (1.7)$$

Accordingly by introducing the values for the set of variables  $\{x'_i\}$  one would get a set of equations for energy parameters. Solving these equations for energy parameters will give us the so-called *recursion relations* for the RG transformation. RG recursion relations provide the topology of the flows on multidimensional parameter space (see Fig. (1.4) for sample illustration) in which some specific points

gain much importance by being invariant under these transformations and are called *fixed points*. We will be dealing in the upcoming chapters with categorizing the fixed points and their relation in determining ordering behaviors, criticality, and phase diagrams. Before that, we start by formulating RG transformation in  $d = 1$  and on higher dimensions.

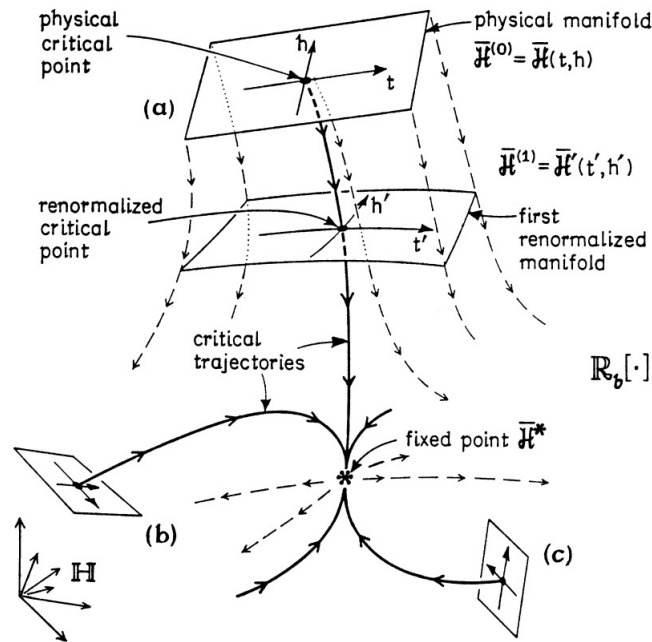


Figure 1.4: Sample illustration of RG flows from Ref [7].

### 1.3.1 RG transformation in $d = 1$

Considering a one-dimensional chain with well-localized sites, an exact scaling procedure can be done by decimation. As an example, let us apply the  $b = 2$  RG transformation on the Ising model considering the Hamiltonian in Eq.(1.1) at  $H = 0$ , with  $N$  lattice sites

$$-\beta\mathcal{H} = J \sum_i s_i s_{i+1} \quad (1.8)$$

In  $b=2, d=1$  the RG transformation as shown in Fig. (x), it is convenient to project lattice coordinates in rescaled coordinates by taking  $i' \equiv j - 1, i' + 1 \equiv j + 1$  where  $j = 2i$  and  $j \leq N$ . With respect to the condition  $Z(J) = Z(J')$ , we may write the

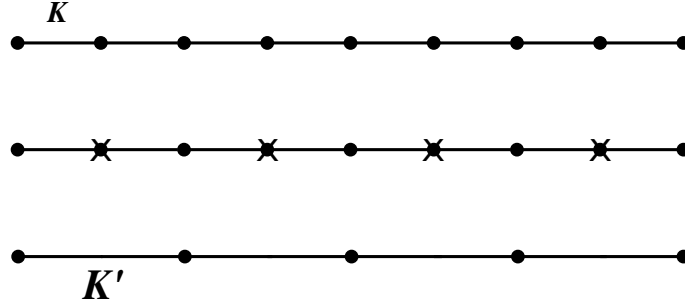


Figure 1.5: RG transformation in  $d = 1$ , with length rescaling factor  $b = 2$ . The degrees of freedom with cross mark have been eliminated and new interactions are obtained in the rescaled picture.

equivalence as

$$e^{J' \sum_{i'} s'_i s'_{i+1} + \tilde{G}} = \sum_{\{\sigma\}} e^{J \sum_i s_i s_{i+1}} \quad (1.9)$$

where  $\tilde{G}$  is an additive constant, prime variables denoting the rescaled system and  $\{\sigma\}$  is the set of eliminated spins which in the case of the  $b = 2$  transformation is  $\{s_2, s_4, s_6, \dots, s_N\}$ . To simplify the above equation, we should rewrite the summation in exponential factors,

$$\prod_{i'} e^{J' s'_i s'_{i+1} + \tilde{G}} = \sum_{\{\sigma\}} \prod_i e^{J s_i s_{i+1}} \quad (1.10)$$

Using  $\sum_{\{\sigma\}} = \sum_{s_2=\pm 1} \sum_{s_4=\pm 1} \dots \sum_{s_N=\pm 1}$  and projecting  $i \rightarrow j$  with relevant transformations, we will have,

$$\prod_{i'} e^{J' s'_i s'_{i+1} + \tilde{G}} = \prod_j \sum_{s_j=\pm 1} e^{J s_j (s_{j-1} + s_{j+1})} \quad (1.11)$$

Hence, the transformation is equivalent at each portion, and we may define functions as

$$R(J', \tilde{G}, s_{j-1}, s_{j+1}) = e^{J' s_{j-1} s_{j+1} + \tilde{G}} = \sum_{s_j=\pm 1} e^{J s_j (s_{j-1} + s_{j+1})} \quad (1.12)$$

Solving the set of equations by introducing the spin variables, we obtain the recursion relations,

$$J' = \frac{1}{2} \ln \cosh(2J), \quad (1.13)$$

$$\tilde{G} = \frac{1}{2} \ln 4 \cosh(2J). \quad (1.14)$$

Solving Eq. (1.13) for  $J' = J = J^*$  will reveal fixed points for that transformation. The overall flow diagram of the RG transformations is given in Fig. (1.6) with fixed points in temperature  $1/J^* = 0, \infty$  are shown in asterisk. As we see in the figure, all finite temperature  $1/J > 0$  points flow to the high-temperature fixed point  $1/J^* = \infty$  indicating that they all belong to the disordered phase. Hence, we conclude that there is no long-range order and accordingly no phase transition at finite temperature.

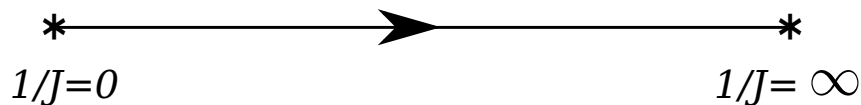


Figure 1.6: RG flow for  $d = 1$  Ising model at zero external field. Successive RG transformations at finite temperatures display this pattern, while fixed points (in asterisk) remain unchanged.

For systems with only nearest-neighbor interactions, the transformation in Eq.(1.12) can be used by generalizing the summation to a summation over all possible spin states. As a last remark, for exact transformations, the results determining thermodynamic and critical properties are independent of the rescaling factor  $b$ . In other words, for the model presented above we will have the same exact result with arbitrary  $b$ . However notice that for AF systems,  $b = 2$  transformation on a bipartite lattice would mean the removal of one of the sublattices and result loss of AF interactions unnecessarily at the first RG transformation. Therefore, for AF models, it is convenient to take an odd value for  $b$ .



### 1.3.2 Migdal-Kadanoff approximation and hierarchical lattices

In higher dimensions, since lattice structures hold higher connectivity it is not easy to suggest an exact scheme due to overbonding of local degrees of freedom when rescaling. However, approximation schemes can be introduced in a consistent basis regarding physical properties put into effect by lattice geometry. The Migdal-Kadanoff approximation is a generalization of RG transformation in  $d = 1$  onto higher dimensions by strengthening local interactions according to a rule in order to account for higher connectivity. The RG transformations on higher dimensions with the Migdal-Kadanoff RG scheme consisting of bond-moving and decimation steps is shown in Fig. (1.7) on a square lattice with length rescaling factor  $b = 2$ .

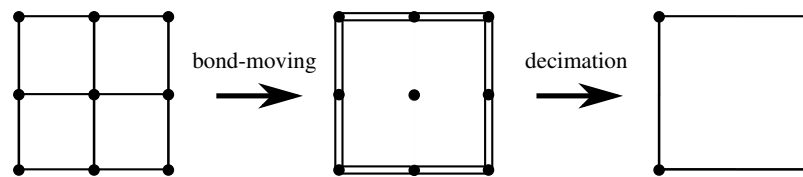


Figure 1.7: The Migdal-Kadanoff RG scheme on a square lattice with  $b = 2$ .

The formulation of Migdal-Kadanoff RG transformation on a  $d$ -dimensional lattice with arbitrary  $b$  will be shown later in this thesis with applications. These transformations are approximate on hypercubic lattices. One can always construct a lattice in which Migdal-Kadanoff procedure becomes exact. Such lattices are referred as hierarchical lattices [8] since they are constructed in a hierarchically growing manner. An example of hierarchical lattice is shown in Fig. (1.8) with  $b = 2$ ,  $d = 2$ . Scaling on these lattices with the same parameters  $b = 2$ ,  $d = 2$  is simply going on the reverse direction in the illustration. While hierarchical lattices have many applications on network science, they also give a pretty much consistent analysis on the effects of dimensionality being strongly suggestive for hypercubic lattices. Thus, maintaining an exact RG analysis on diverse models with a wide scope of physical implementations on these structures is highly valuable for experimental and simulational studies.

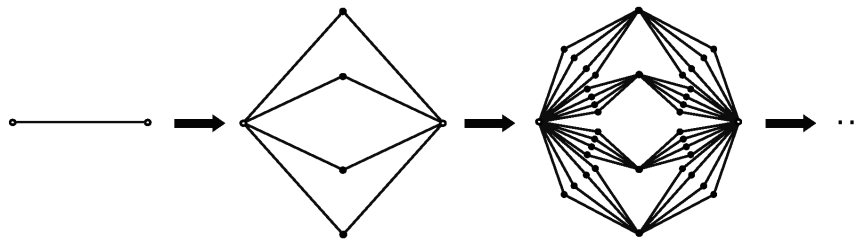


Figure 1.8: Construction of a hierarchical lattice with  $b = 2$ ,  $d = 2$  [8].

### 1.3.3 Calculation of phase diagrams

The unstable fixed points from which the flows are outwards are the critical fixed points. If we start rescaling at this point  $\vec{\mathbf{K}} = \vec{\mathbf{K}}^* = \vec{\mathbf{K}}_c$ , we have scale invariance and thus stay at that point under successive RG transformations. The flows going outwards of this point should reach other fixed points, i.e., stable fixed points, and these are generally the sink of a phase. We have an example in Fig. (1.9) illustrating common flow diagram for the Ising model in  $d > 1$  at zero field. Using the above facts, if the analytical approach is not sufficient for obtaining fixed points, it is feasible to implement numerical techniques. In general, if the interaction set  $\vec{\mathbf{K}}$  consists of  $m$  independent parameters, the RG flows are represented on  $m$ -dimensional space, while the phase diagram is shown as a function of initial (physical) interaction parameters. Therefore, investigation of RG flows and categorization of fixed points should be carried out with a proper analysis.

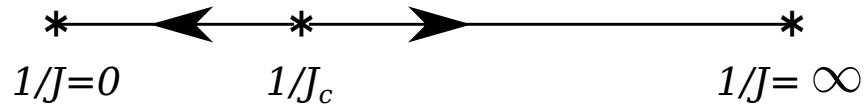


Figure 1.9: RG flow for  $d > 1$  Ising model at zero external field. Successive RG transformations at finite temperatures display this pattern, while fixed points (in asterisk) remain unchanged.

### 1.3.4 Calculation of thermodynamic properties

#### Free Energy

In order to get rid of asymptotic behaviors in thermodynamic limit  $N \rightarrow \infty$ , it is much more convenient to consider thermodynamic functions per site or per bond. The additive constants on each interaction in Eq.(1.14) indeed help in solving for dimensionless free energy per bond for the system,

$$f_b = -\frac{1}{JN_b} \ln Z. \quad (1.15)$$

since in general we set the dimensionless temperature as  $1/J$ . As we see from the above equation  $f_b$  is proportional to  $\ln Z$ . Thus, our aim is to solve  $\ln Z$  using RG

transformations until reaching the asymptotic limit  $n \rightarrow \infty$ , where  $n$  is the RG iteration number. The formalism in Eqs.(1.10-1.12) gives us a clue on the use of additive constants. Remembering the form of partition function we have

$$\begin{aligned} \ln Z &= \ln \sum_{\{s\}} e^{-\beta \mathcal{H}} \\ &= \ln \sum_{\{s'\}} e^{-\beta \mathcal{H}' + N'_b \tilde{G}} \\ &= \ln \sum_{\{s'\}} e^{-\beta \mathcal{H}'} + N'_b \tilde{G} \end{aligned} \quad (1.16)$$

which becomes, continuing recursively until last RG transformation  $n$ ,

$$= \ln \sum_{\{s^{(n)}\}} e^{-\beta \mathcal{H}^{(n)}} + \sum_{k=1}^n N_b^{(k)} \tilde{G}^{(k)} \quad (1.17)$$

with superscripts denoting belonging to that RG iteration. When taking  $n \rightarrow \infty$ , we would be expecting to have a finite set of coordinates  $\{s^{(n)}\}$  and to be at a fixed point for the term  $\beta \mathcal{H}^{(n)}$ . Accordingly, for all values of the expression in the logarithmic term, the first term cannot survive when divided by factor  $JN_b$ , since at least  $N_b \rightarrow \infty$  much faster in the thermodynamic limit. As a result the Eq. (1.15) becomes,

$$\begin{aligned} f_b &= -\frac{1}{JN_b} \sum_{k=1}^n N_b^{(k)} \tilde{G}^{(k)} \\ &= -\frac{1}{J} \sum_{k=1}^n \frac{\tilde{G}^{(k)}}{b^{kd}} \end{aligned} \quad (1.18)$$

using  $N_b^{(k)}/N_b = b^{-kd}$  for decimation in  $d = 1$  and Migdal-Kadanoff transformations.

### Critical exponents

Critical exponents are used for understanding the critical behavior of systems near a phase transition (second-order - or critical - phase transition). In general, thermodynamic functions exhibit a singularity near criticality, thus are no longer

analytical functions. However, we may obtain dependence on relevant parameters such as temperature and external field as a power law in the asymptotic limit. In scaling analysis, we may obtain critical behavior from the flows of the interaction parameters near a critical point. The calculation of critical exponents is done by a linearization around the critical point. In a case where only interaction parameters are  $J$  and  $H$ , as in Eq. (1.1), the related critical exponents are obtained from

$$\begin{aligned} \frac{\partial J'}{\partial J} \Big|_{J=J_c, H=H_c} &= b^{y_T}, \\ \frac{\partial H'}{\partial H} \Big|_{J=J_c, H=H_c} &= b^{y_H}. \end{aligned} \quad (1.19)$$

where  $b^{y_T}, b^{y_H}$  give the scaling of relevant fields and  $y_T, y_H$  are the critical exponents. Since thermodynamic properties are functions of these parameters, we may accordingly calculate all other critical exponents with scaling analysis (Kadanoff construction). For ferromagnetic systems, the critical fixed point is found when  $H = H_c = 0$  due to symmetry. In general, if we have RG flows in phase space with multiple interaction parameters, i.e., with  $s$  interaction parameters  $\vec{\mathbf{K}} = \{K_1, K_2, \dots, K_s\}$ , then the critical exponent can be obtained from eigenvalues of the recursion matrix with elements  $\partial K'_l / \partial K_m$ ,

$$\frac{\overleftrightarrow{\partial \mathbf{K}'}}{\partial \mathbf{K}} = \begin{pmatrix} \frac{\partial K'_1}{\partial K_1} & \frac{\partial K'_1}{\partial K_2} & \cdots & \frac{\partial K'_1}{\partial K_s} \\ \frac{\partial K'_2}{\partial K_1} & \frac{\partial K'_2}{\partial K_2} & & \\ \vdots & & \ddots & \\ \frac{\partial K'_s}{\partial K_1} & & & \frac{\partial K'_s}{\partial K_s} \end{pmatrix} \quad (1.20)$$

at the critical fixed point  $\vec{\mathbf{K}} = \vec{\mathbf{K}}_c$ . As we seek an eigenvalue in the form  $b^{y_T}$ , the one being larger than unity will be our critical exponent.

### 1.3.5 RG transformation of systems with quenched randomness

The bimodal probability distribution implementing quenched randomness on types of bonds across the lattice as introduced in Section 1.2.2, can be written in func-

tional form with

$$P(J_{ij}) = p\delta(J_{ij} + J) + (1 - p)\delta(J_{ij} - J). \quad (1.21)$$

As we will see later on in this thesis, the probability distribution of renormalized interactions are represented by a renormalized quenched probability distribution. Furthermore, the renormalized probability distribution evolves to a more complex one in the upcoming steps. After applying a sufficient number of RG iterations until reaching the asymptotic trend of the distribution, we may have information about the ordering behavior of the system for given initial (physical) parameters. Without loss of generality, it is convenient to represent the relevant parameters to classify the distribution as the normalized distribution  $P(J_{ij}/\langle |J_{ij}| \rangle)$  and the average magnitude of interactions  $\langle |J_{ij}| \rangle$ . As a matter of fact, the asymptotic distribution is the fixed distribution  $P^*(J_{ij}/\langle |J_{ij}| \rangle)$  and defines the ordering behavior or criticality of the system along with the asymptotic behavior of  $\langle |J_{ij}| \rangle$ .

Along with the large scale flow analysis of all local interactions in a system, the characteristic behavior of interactions at a single location under rescaling can be maintained by RG transformations. As previously discussed in Section (1.2.1) spin glasses exhibit diversity in correlations (weak/strong and F/AF) upon changing length scale. The behavior is observed to be in a chaotic sequence under successive RG transformations of local interactions at a specific point in the lattice. As we will show in the upcoming chapters, the distribution of chaotic visits of interactions at a specific location under rescaling trajectories is indeed equivalent to the fixed distribution of interactions at different locations showing that chaos is spread out at all length scales in the same manner.

## 1.4 Overview of thesis

The main objective of the thesis is studying a variety of spin-glass systems and achieve a new perspective on understanding spin-glass theory. Thus, new types of spin glass systems are introduced resulting in a rich information on these complex structures and novel orderings. In the upcoming chapter we will be dealing with controlling the frustration level on spin-glass systems by adding locally correlated quenched randomness, and accordingly we show how frustration level affects these systems on the destruction of orderings, chaotic rescaling behaviors, and thermodynamic properties. In chapter 3, q-state clock spin-glass models with symmetry in ordering (even q-state clock models) are investigated up to reaching high q-values and thus XY model limit. In chapter 4, we study spin-glass systems without symmetry in ordering of F and AF (odd q-state clock models) which belongs to a class of systems having ground-state entropy even without bond frustration. Finally, the diffusive dynamics on non-equilibrium systems are discussed in chapter 5. In general, the effects of microlevel motions are observed indirectly in the macroworld, hence observables that are less sensitive to microlevel randomness can be obtained with fewer parameters. The main aim in the first section is to simplify the transition scheme from microlevel and continuous time analysis which will be sufficient to define the motional effects on such systems. In the second section, we examine a system starting from a constrained free energy configuration, evolving to the equilibrium state under the effect of thermodynamics competing with diffusion energy barriers.

---

## REFERENCES

- [1] H. E. Stanley, *Introduction to phase transitions and critical phenomena* (Oxford University Press, 1971).
- [2] J. M. Yeomans, *Statistical Mechanics of Phase Transitions* (Oxford University Press, 1992).
- [3] N. Goldenfeld, *Lectures on Phase Transitions and Renormalization Group* (Perseus Books, 1992).
- [4] H. Nishimori, *Statistical Physics of Spin Glasses and Information Processing* (Oxford University Press, 2001).
- [5] K. Binder and A. P. Young, *Rev. Mod. Phys.* **58**, 801 (1986).
- [6] D. C. Mattis and R. H. Swendsen, *Statistical Mechanics Made Simple* (World Scientific Publishing, 2008).
- [7] M. E. Fisher, in *Lecture Notes in Physics*, Vol. 186, *Critical Phenomena*, edited by F. J. W. Hahne (Springer, Berlin, Germany 1983).
- [8] A. N. Berker and S. Ostlund, *J. Phys. C* **12**, 4961 (1979).
- [9] K. Huang, *Statistical Mechanics* (John Wiley & Sons, 1987).
- [10] S. R. McKay, A. N. Berker, and S. Kirkpatrick, *Phys. Rev. Lett.* **48**, 767 (1982).
- [11] S. R. McKay, A. N. Berker, and S. Kirkpatrick, *J. Appl. Phys.* **53**, 7974 (1982).



Chapter 2

**CONTROLLING FRUSTRATION AND  
CHAOS IN SPIN GLASSES**

## 2.1 Introduction

The occurrence of spin-glass long-range order [1], ground-state entropy [2, 3], and chaotic rescaling behavior [4, 5] has long been discussed in spin-glass systems, with reference to spatial dimensionality  $d$ , interaction randomness and frustration [6], accepted as inherent to spin-glass systems and spin-glass order. In Ising models with randomly distributed nearest-neighbor ferromagnetic and antiferromagnetic interactions on hypercubic lattices, it has been shown that a spin-glass phase does not occur in  $d = 2$  and does occur in  $d = 3$ . [7] In these hypercubic systems, frustration occurs in elementary squares with an odd number of antiferromagnetic interactions. Thus, with interactions randomly distributed with no correlation, maximally 50 % of the elementary squares can be frustrated. This fraction increases from zero as the concentration of frozen antiferromagnetic bonds  $p$  is increased from zero and reaches its maximal value of 50 % at  $p = 0.5$ .

The basis of the current study is the realization that, for any value of the antiferromagnetic bond concentration  $0 < p < 1$ , the fraction of frustrated squares can be varied considerably. For example, for the square lattice, for  $0.25 \leq p \leq 0.75$ , the fraction of frustrated squares can be made to vary to any value between 0 and 1 inclusive, by the locally correlated occurrence quenched random bonds. For  $p \leq 0.25$ , the fraction of frustrated squares can similarly be made to vary between 0 and  $4p$ . For  $0.75 \leq p$ , the fraction of frustrated squares can be made to vary between 0 and  $4(1 - p)$ . (Thus, frustration reaches 0 with no variation as  $p$  approaches 0 or 1.) Examples are shown in Fig. 2.1 for  $p = 0.5$ . Thus, when the fraction of frustrated squares is zero, we have a so-called Mattis spin glass [8]. At the other extreme, we have a fully frustrated system [9, 10, 11, 12, 13]. All frustration values in between can be obtained, by randomly removing or adding local frustration without changing the antiferromagnetic bond concentration  $p$  (Fig. 2.1).

In this study, we have implemented an exact renormalization-group study for Ising spin-glass models on the hierarchical lattices, with  $d = 3$  and  $d = 2$ , respectively shown in Figs. 2.2(b) and 2.3(b), for arbitrary overfrustration or underfrustration implemented by locally correlated quenched randomness. We have

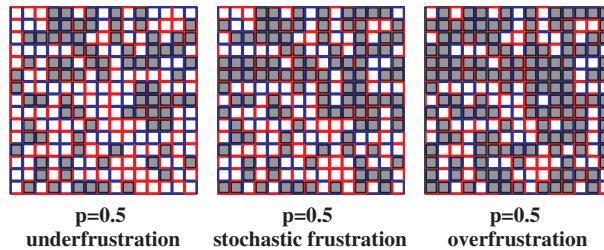


Figure 2.1: (Color online) Randomly distributed ferromagnetic (blue) and antiferromagnetic (red) interactions on a square plane. In all three cases, the antiferromagnetic bond concentration is  $p = 0.5$ . The frustrated squares are shaded. In the case at the center, the bonds were distributed in an uncorrelated fashion, leading to the frustration of half of the squares (stochastic frustration). In the case at the left, 25% of the frustration was randomly removed without changing  $p = 0.5$  (underfrustration). In the case at the right, 25% frustration was randomly added without changing  $p = 0.5$  (overfrustration). Frustration can thus be set between zero and complete frustration. It is clear that frustration can thus be adjusted in all hypercubic lattices.

calculated 18 complete phase diagrams, each for a different frustration level, in temperature and antiferromagnetic bond probability  $p$ . We find that the increase of frustration disfavors the spin-glass phase (while at low temperatures favoring the spin-glass phase at the expense of the ferromagnetic phase and, symmetrically, antiferromagnetic phase.) Both in  $d = 3$  and  $d = 2$ , the spin-glass phase disappears at zero temperature when a certain level of frustration is reached. However, this disappearance of the spin-glass phase happens in different regimes in  $d = 3$  and  $d = 2$ : For  $d = 3$ , it occurs in overfrustration, so that at stochastic frustration (no correlation in randomness) a spin-glass phase occurs. For  $d = 2$ , it already occurs in underfrustration, so that at stochastic frustration a spin-glass phase does not occur. However, with frustration only partially removed, we find that a spin-glass phase certainly does occur in  $d = 2$ .

The chaotic rescaling [4, 5, 14, 15, 16, 17, 18, 19, 20, 21, 22, 23, 24, 25, 26, 27, 28, 29, 30, 31, 32, 33, 34, 35] of the interactions within the spin-glass phase occurs as soon as frustration is increased from zero, both in  $d = 3$  and  $d = 2$ . We have calculated the Lyapunov exponent  $\lambda$  [36, 37] of the renormalization-group trajectory of the interaction at a given location, when the system is in the spin-glass phase. When frustration is increased from zero, the Lyapunov exponent  $\lambda$

increases from zero, both in  $d = 3$  and  $d = 2$ . This behavior is of course consistent with the chaotic renormalization-group trajectories. Different values of the positive Lyapunov exponents characterize different spin-glass phases. It is found here that the value of the Lyapunov exponent continuously varies with the level of frustration and is different for each dimensionality  $d$ . The Lyapunov exponent does not depend on antiferromagnetic bond concentration  $p$  or temperature.

Our calculations with varying frustration also yield information on long- and short-range ordering, and entropy. The increase in frustration lowers both the onset temperature of long-range order and the characteristic temperature of short-range order, but affects long-range order much more drastically, thus interchanging the two temperatures and eventually eliminating long-range spin-glass order. For  $d = 3$ , for low frustration, the specific heat peak occurs inside the spin-glass phase, indicating that considerable short-range disorder persists into the higher temperatures of the spin-glass phase. In these cases, as temperature is lowered, spin-glass long-range order onsets before the system is predominantly short-range ordered. As frustration is increased, both ordering temperatures are lowered, but differently, so that they interchange before stochastic frustration is reached. Thus, for overfrustration, stochastic frustration, and higher frustration values of underfrustration, the specific heat peak occurs outside the spin-glass phase, indicating that as temperature is lowered, short-range order sets before long-range order (which reaches zero temperature in overfrustration). Zero-temperature or low-temperature entropy is a distinctive character of systems with frustration. Frustration is introduced into the system, by increasing from zero the antiferromagnetic bond concentration  $p$ . It is seen that frustration favors the spin-glass phase over the ferromagnetic phase. However, it is also seen that, in all cases that frustration is introduced, the major portion of the entropy is created with the ferromagnetic phase as opposed to the spin-glass phase.

## 2.2 Overfrustrated and underfrustrated spin-glass systems on hypercubic lattices and hierarchical lattices

### 2.2.1 Stochastic Frustration, Overfrustration, and Underfrustration on Hypercubic Lattices

The Ising spin-glass model is defined by the Hamiltonian

$$-\beta\mathcal{H} = \sum_{\langle ij \rangle} J_{ij} s_i s_j \quad (2.1)$$

where  $\beta = 1/kT$ , at each site  $i$  of a lattice the spin  $s_i = \pm 1$ , and  $\langle ij \rangle$  denotes that the sum runs over all nearest-neighbor pairs of sites. The bond strengths  $J_{ij}$  are  $+J > 0$  (ferromagnetic) with probability  $1 - p$  and  $-J$  (antiferromagnetic) with probability  $p$ . On hypercubic lattices, in any elementary square with an odd number number of antiferromagnetic bonds, all bonds cannot be simultaneously satisfied, meaning that there is frustration.[6] When the antiferromagnetic bonds are randomly distributed with probability  $p$  across the lattice, a fraction

$$4p(1 - p)^3 + 4p^3(1 - p) = 4(p - 3p^2 + 4p^3 - 2p^4) \quad (2.2)$$

of the elementary squares is frustrated. This system with uncorrelated quenched randomness is the usually studied spin-glass system and we shall refer to it as a **stochastically frustrated** system. On the other hand, by changing the signs of individual bonds  $J_{ij} \rightarrow -J_{ij}$  at randomly chosen localities, with the rule that, for every ferromagnetic-to-antiferromagnetic local change, an antiferromagnetic-to-ferromagnetic local change is done, frustration can be continuously increased or decreased from the value in Eq.(2.2), without changing the antiferromagnetic bond concentration  $p$ . We call the systems in which frustration is thus increased or decreased from stochastic frustration, respectively, **overfrustrated** or **underfrustrated** systems. Examples of overfrustration, stochastic frustration, and underfrustration are given in Fig. 2.1.

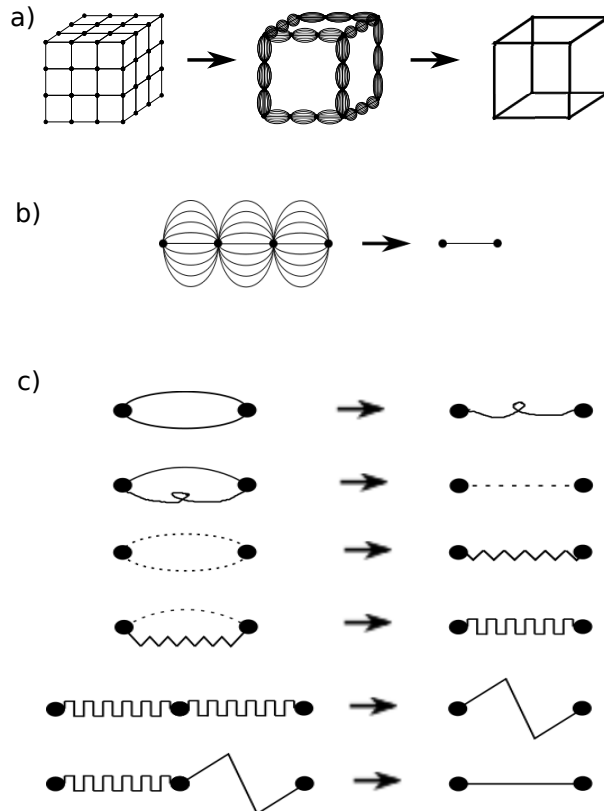


Figure 2.2: (a) Migdal-Kadanoff approximate renormalization-group transformation for the  $d = 3$  cubic lattice with the length-rescaling factor of  $b = 3$ . Bond-moving is followed by decimation. (b) Exact renormalization-group transformation for the equivalent  $d = 3$  hierarchical lattice with the length-rescaling factor of  $b = 3$ . (c) Pairwise applications of the quenched probability convolution of Eq.(2.5), leading to the exact transformation in (b) and, numerically equivalently, to the approximate transformation in (a).

### 2.2.2 Renormalization-Group Transformation, Quenched Probability Convolutions by Histograms and Cohorts

The usual, stochastically frustrated spin-glass systems on hypercubic lattices are readily solved by a renormalization-group method that is approximate on the hypercubic lattice [38, 39] and simultaneously exact on the hierarchical lattice [40, 41, 42, 43, 44]. Under rescaling, the form of the interaction as given in Eq.(2.1) is conserved. The renormalization-group transformation, for spatial dimension  $d$  and length-rescaling factor  $b = 3$  (necessary for treating the ferromagnetic and antiferromagnetic correlations on equal footing), is achieved (Figs. 2.2(a) and

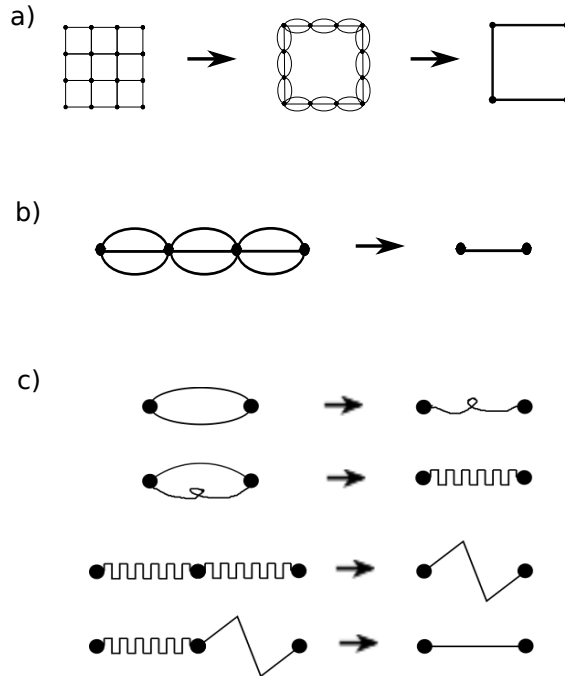


Figure 2.3: (a) Migdal-Kadanoff approximate renormalization-group transformation for the  $d = 2$  square lattice with the length-rescaling factor of  $b = 3$ . Bond-moving is followed by decimation. (b) Exact renormalization-group transformation for the equivalent  $d = 2$  hierarchical lattice with the length-rescaling factor of  $b = 3$ . (c) Pairwise applications of the quenched probability convolution of Eq.(2.5), leading to the exact transformation in (b) and, numerically equivalently, to the approximate transformation in (a).

2.3(a)) by a sequence of bond moving

$$J_{ij}^{(bm)} = \sum_{\langle kl \rangle}^{b^{d-1}} J_{kl} \quad (2.3)$$

and decimation

$$e^{J_{im}^{(dec)} s_i s_m + G_{im}} = \sum_{s_j, s_k} e^{J_{ij} s_i s_j + J_{jk} s_j s_k + J_{km} s_k s_m}, \quad (2.4)$$

where the additive constants  $G_{ij}$  are unavoidably generated.

The starting bimodal quenched probability distribution of the interactions, characterized by  $p$  and described above, is not conserved under rescaling. The renormalized quenched probability distribution of the interactions is obtained by

the convolution [45]

$$P'(J'_{i'j'}) = \int \left[ \prod_{ij}^{i'j'} dJ_{ij} P(J_{ij}) \right] \delta(J'_{i'j'} - R(\{J_{ij}\})), \quad (2.5)$$

where the primes denote the renormalized system and  $R(\{J_{ij}\})$  represents the bond moving and decimation given in Eqs.(2.3) and (2.4). For numerical practicality, the bond moving and decimation of Eqs.(2.3) and (2.4) are achieved by a sequence of pairwise combination of interactions, as shown for  $d = 3$  and  $d = 2$  respectively in Figs. 2.2(c) and 2.3(c), each pairwise combination leading to an intermediate probability distribution resulting from a pairwise convolution as in Eq.(2.5).

We implement this procedure numerically in two computationally equivalent ways: (1) The quenched probability distribution is represented by histograms.[47, 49, 50, 51] A total number of between 500 to 2,500 histograms, depending on the needed accuracy, is used here. This total number is distributed between ferromagnetic  $J > 0$  and antiferromagnetic  $J < 0$  interactions according to the total probabilities for each case. (2) By generating a cohort of 20,000 interactions [31] that embodies the quenched probability distribution. At each pairwise convolution as in Eq.(2.5), 20,000 randomly chosen pairs are matched by Eq.(2.3) or (2.4), and a new set of 20,000 is produced. The numerical convergence of the histogram and cohort implementations are determined, respectively, by the numbers of histograms and cohort members. At numerical convergence, the results of the two implementations match. The histogram method is faster and is used to calculate phase diagrams, thermodynamic properties, and asymptotic fixed distributions. The cohort method is needed for studying the repeated rescaling behavior of the interaction at a specific location on the lattice and is used to calculate chaotic trajectories, chaotic bands, and Lyapunov exponents.[31]

### 2.2.3 Stochastic Frustration, Overfrustration, and Underfrustration on Hierarchical Lattices

Hierarchical models are models which are exactly soluble by renormalization-group theory.[40, 41, 42, 43, 44] Hierarchical lattices have therefore been used to study



a variety of spin-glass and other statistical mechanics problems.[46, 47, 48, 49, 50, 51, 52, 53, 54, 55, 56, 57, 58] Hierarchical models can be constructed [40] that have identical renormalization-group recursion relations with the approximate treatment of models on hypercubic and other Euclidian lattices. Thus, Figs. 2.2(b) and 2.3(b) respectively give the hierarchical models, used in our study, that have the same recursion relations as the Migdal-Kadanoff approximation [38, 39] for the hypercubic lattice in  $d = 3$  (cubic lattice) and  $d = 2$  (square lattice).

Overfrustration or underfrustration is readily introduced into hierarchical lattices by randomly changing local interactions or groups of local interactions, while conserving  $p$ . This overfrustration or underfrustration affects the pairwise bond-moving step of the renormalization-group solution. In the case of overfrustration, when two bonds are matched for bond-moving, bonds of the same sign are accepted with a probability  $g$ ,  $0 \leq g < 1$ . Clearly, when  $g = 1$ , we have not altered the occurrence of frustration. But, for a value of  $g$  in the range  $0 \leq g < 1$ , we have removed a fraction  $1 - g$  of the unfrustrated occurrences.

Similarly, in the case of underfrustration, when two bonds are matched for bond-moving, bonds of the opposite sign are accepted with a probability  $f$ ,  $0 \leq f < 1$ . Again, when  $f = 1$ , we have not altered the occurrence of frustration. But, for a value of  $f$  in the range  $0 \leq f < 1$ , we have removed a fraction  $1 - f$  of the frustrated occurrences.

We have thus defined the degree of frustration on the hierarchical models. Accordingly, full frustration, stochastic frustration, and zero frustration respectively correspond to  $g = 0$ ,  $g = 1 = f$ ,  $f = 0$ . Our implementation of underfrustration and overfrustration via the factors  $f$  and  $g$  does affect, on the hierarchical lattice, the effective value of the antiferromagnetic bond probability  $p$  as

$$\begin{aligned}
 p_{effective} &= \frac{p - (1 - f)p(1 - p)}{1 - (1 - f)2p(1 - p)}, \\
 p_{effective} &= \frac{p - (1 - g)p^2}{1 - (1 - g)(p^2 + (1 - p)^2)}.
 \end{aligned}
 \tag{2.6}$$

$p_{effective}$  includes the combined effect of  $p$  together with the local quenched correlation rule controlled by  $f$  or  $g$ . (The actual microscopic renormalization-group

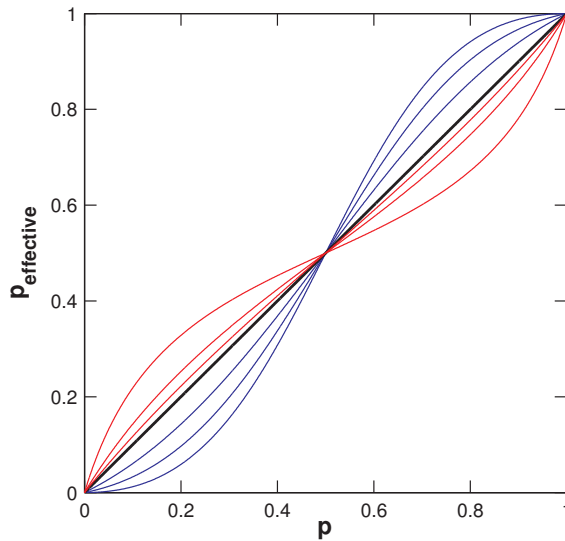


Figure 2.4: (Color online)  $p_{effective}$  versus  $p$  for the range of underfrustration and overfrustration used in our study (Eq.(2.6)). The curves are, consecutively from the lower right, for  $f = 0, 0.2, 0.5$ ;  $f = 1 = g$  (thicker line);  $g = 0.8, 0.6, 0.3$ .

calculation is of course done using  $p$  with the quenched correlation rule, which completely defines the model.) Eqs.(2.6) directly follow from the acceptance rules given in the previous two paragraphs: The second terms in the numerators subtract the probability due to rejection because of a bond-moving match that is suppressed; the denominator is a normalization taking into account this rejection probability. Thus,  $p = 0.5$ , the center of a would-be spin-glass phase, is not affected. For other values,  $p_{effective}$  stays close to  $p$ , as seen in Fig. 2.4. Just as in the case of underfrustrated and overfrustrated hypercubic lattices (Fig. 2.1), underfrustrated and overfrustrated hierarchical lattices as defined and studied here can be physically realized. However, our procedure of underfrustrating or overfrustrating hierarchical lattices is not a direct representation of underfrustrating or overfrustrating hypercubic lattices. One important difference is that, in hierarchical lattices, underfrustrating or overfrustrating is done at every length scale. This leaves the underfrustrated or overfrustrated hypercubic lattices, which can be achieved as we demonstrated, as an interesting open problem, with our current results only being suggestive.

### 2.2.4 Determination of the Phase Diagrams and Thermodynamic Properties

The different thermodynamic phases of the model are identified by the different asymptotic renormalization-group flows of the quenched probability distributions. For all renormalization-group flows, inside the phases and on the phase boundaries, Eq.(2.5) is iterated until asymptotic behavior is reached, meaning that we are studying an effectively infinite hierarchical lattice. The thermodynamic properties, such as free energy, energy, entropy, and specific heat, are calculated by summing along entire renormalization-group trajectories.[40, 43, 44, 59] Thus, we are able to calculate phase diagrams and thermodynamic properties for any case of overfrustration or underfrustration.

## 2.3 Calculated phase diagrams for overfrustration and underfrustration in $d = 3$ and $d = 2$

Figure 5 shows 18 different calculated phases diagrams, in temperature  $1/J$  and antiferromagnetic bond concentration  $p$ , for overfrustrated, stochastically frustrated, underfrustrated Ising spin-glass models in  $d = 3$  and  $d = 2$ . Each phase diagram has a different amount of overfrustration or underfrustration, or is stochastically frustrated. In general, increased frustration drives the spin-glass phase to lower temperatures. Thus, the spin-glass phase disappears at a threshold amount of frustration. This threshold frustration is dramatically different in  $d = 3$  and  $d = 2$ , as explained below. On the other hand, increased frustration favors the spin-glass phase (before it disappears) over the ferromagnetic phase and symmetrically the antiferromagnetic phase, at low temperatures.

The left panels are for  $d = 3$  dimensions. The outermost phase diagram, consisting of one horizontal and two vertical lines, is for no frustration,  $f = 0$ . Starting from this outermost phase diagram, the consecutive phase diagrams have increasing frustration: They are for the underfrustrated cases (where frustration has been removed) of  $f = 0.1, 0.2, 0.5, 0.8$ ; the stochastic case (where frustration has been neither removed, nor added) of  $f = 1 = g$ , drawn with the thicker lines; and the

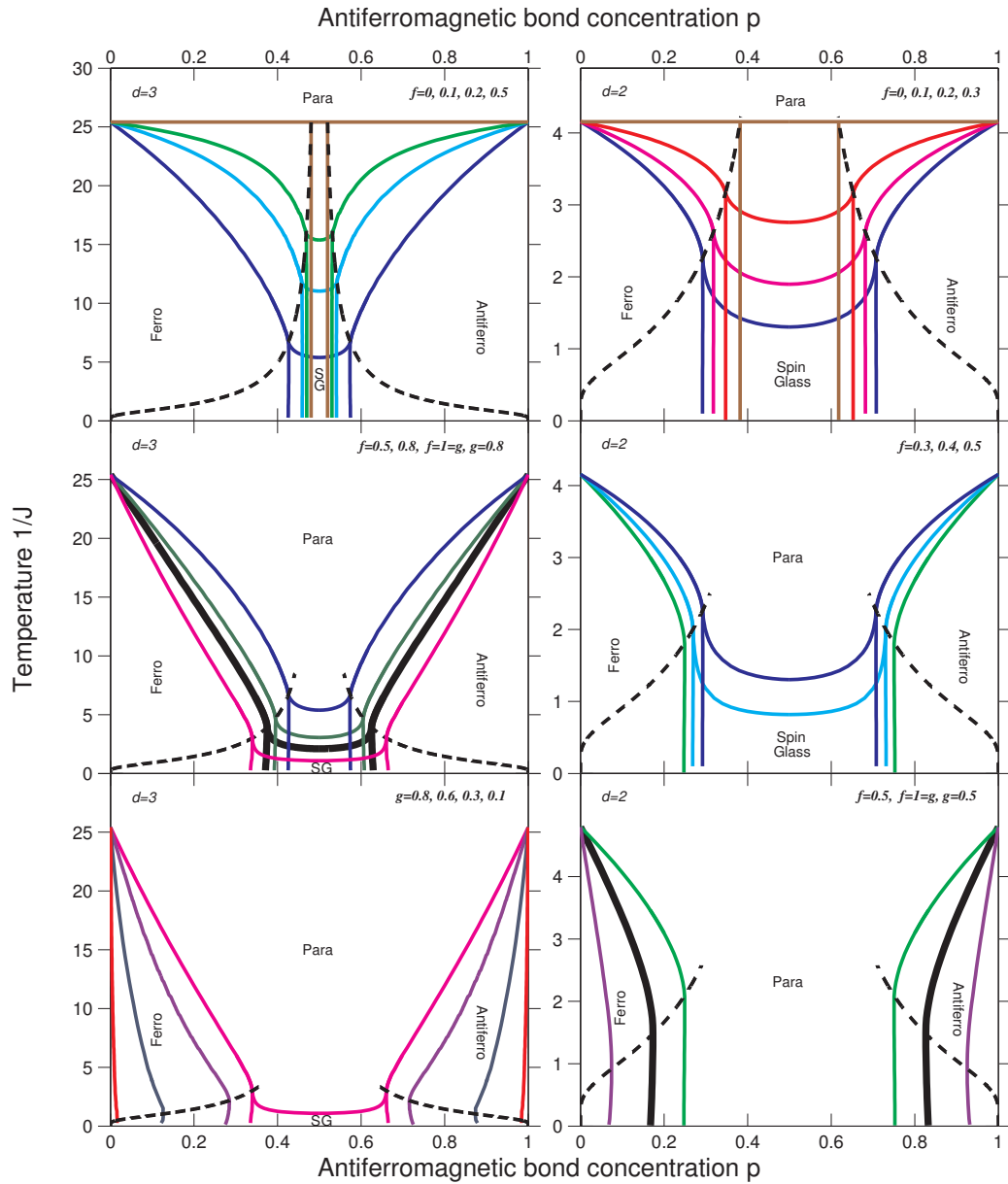


Figure 2.5: (Caption next page.)

overfrustrated case (where frustration has been added) of  $g = 0.8, 0.6, 0.3, 0.1$ . In the latter three cases,  $g = 0.6, 0.3, 0.1$ , no spin-glass phase occurs. Thus, in  $d = 3$ , excessive overfrustration destroys the spin-glass phase.

The right panels are for  $d = 2$  dimensions. Again, the outermost phase diagram, consisting of one horizontal and two vertical lines, is for no frustration,  $f = 0$ . Starting from this outermost phase diagram, the consecutive phase diagrams again have increasing frustration: They are for the underfrustrated cases of  $f = 0.1, 0.2, 0.3, 0.4, 0.5$ ; the stochastic case of  $f = 1 = g$ , drawn with the

Figure 2.5: (Previous page) Calculated phase diagrams (color online) of the overfrustrated, underfrustrated, and stochastically frustrated Ising spin-glass models on hierarchical lattices. The panels on the left side are for  $d = 3$  dimensions. Left top panel: The outermost phase diagram, consisting of one horizontal and two vertical lines, is for no frustration,  $f = 0$ . Starting from this outermost phase diagram, the three consecutive phase diagrams are for the underfrustrated cases (where frustration has been removed) of  $f = 0.1, 0.2, 0.5$ . Left middle panel: Starting from the outermost phase diagram, the four consecutive phase diagrams are for the underfrustrated cases of  $f = 0.5, 0.8$ ; the stochastic case (where frustration has been neither removed, nor added) of  $f = 1 = g$ , drawn with the thicker lines; and the overfrustrated case (where frustration has been added) of  $g = 0.8$ . Left bottom panel: Starting from the outermost phase diagram, the four consecutive phase diagrams are for the overfrustrated cases of  $g = 0.8, 0.6, 0.3, 0.1$ . In the latter three cases,  $g = 0.6, 0.3, 0.1$ , no spin-glass phase occurs. Excessive overfrustration destroys the spin-glass phase. The panels on the right side are for  $d = 2$  dimensions. Right top panel: The outermost phase diagram, consisting of one horizontal and two vertical lines, is for no frustration,  $f = 0$ . Starting from this outermost phase diagram, the three consecutive phase diagrams are for the underfrustrated cases of  $f = 0.1, 0.2, 0.3$ . Right middle panel: Starting from the outermost phase diagram, the three consecutive phase diagrams are for the underfrustrated cases of  $f = 0.3, 0.4, 0.5$ . Right bottom panel: Starting from the outermost phase diagram, the three consecutive phase diagrams are the underfrustrated case of  $f = 0.5$ ; for the stochastic case of  $f = 1 = g$ , drawn with the thicker lines; and the overfrustrated case of  $g = 0.5$ . In the latter three cases,  $f = 0.5, f = 1 = g, g = 0.5$ , no spin-glass phase occurs. However, in the underfrustrated cases of  $f = 0.1, 0.2, 0.3, 0.4$ , a spin-glass phase occurs in these  $d = 2$  dimensional systems with locally correlated randomness. All phase transitions in this figure are second order and, to the resolution of the figure, all multicritical points appear on the Nishimori symmetry line, shown with the dashed curves.

thicker lines; and the overfrustrated case of  $g = 0.5$ . In the latter three cases,  $f = 0.5, f = 1 = g, g = 0.5$ , no spin-glass phase occurs. However, in the underfrustrated cases of  $f = 0.1, 0.2, 0.3, 0.4$ , a spin-glass phase does occur in these  $d = 2$  dimensional systems with locally correlated randomness. Thus, when frustration is increased from zero, the spin-glass phase disappears while still in the underfrustrated regime. Accordingly, in ordinarily studied spin-glass systems, which are stochastically frustrated systems, the spin-glass phase is seen in  $d = 3$ , but not seen in  $d = 2$ .

The paramagnetic-ferromagnetic-spin-glass reentrance for the phase diagrams with the spin-glass phase and the paramagnetic-ferromagnetic-paramagnetic (true) reentrance for the phase diagrams without the spin-glass phase, as temperature is lowered, is seen here. Both types of phase diagrams were first noted with hierarchical models for Ising spin glasses [47] and Potts spin glasses [48]. Phase diagram reentrance is also seen in experimental spin-glass systems [60] and, most prominently, in liquid crystal systems where annealed (as opposed to quenched as in the current study) frustration plays a role.[61, 62, 63, 64] All phase transitions in Fig. 2.5 are second order and, to the resolution of the figure, the multicritical points appear on the Nishimori symmetry line, shown with the dashed curves.[65, 66, 67, 68, 69]

## 2.4 Chaos in the Spin-Glass Phase Triggered by Infinitesimal Frustration

The local interaction at a given position in the lattice at successive renormalization-group transformations, in systems with different frustrations, is given for  $d = 3$  and 2 respectively in Figs. 2.6 and 2.7. These consecutively renormalized interactions at a given position of the system are shown here as scaled with the average interaction  $\langle |J| \rangle$  across the system, which diverges as  $b^{ny_R}$  where  $n$  is the number of renormalization-group iterations and  $y_R > 0$  is **the runaway exponent** shown in Fig. 2.10. This divergence indicates **strong-coupling chaotic behavior**. [31] In Figs. 2.6 and 2.7, it is seen that, for any amount of frustration, the local interaction at a given position in the lattice exhibits, under

renormalization-group transformations, a chaotic trajectory.[15]

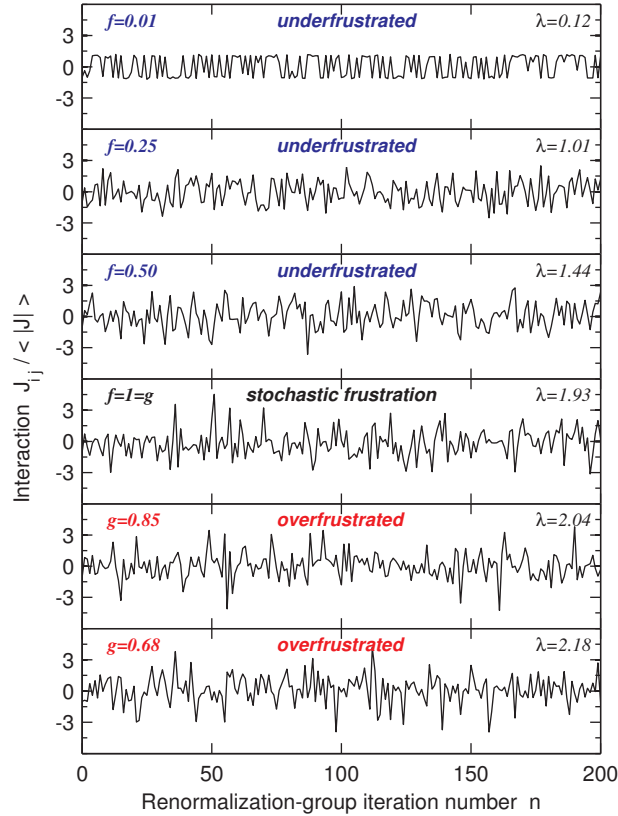


Figure 2.6: (Color online) Interaction at a given position in the lattice at successive renormalization-group iterations, for  $d = 3$  systems with different frustrations. In all cases, the antiferromagnetic bond concentration is  $p = 0.5$  and the initial temperature is  $1/J = 0.2$ , inside the spin-glass phase. For each frustration amount, a chaotic trajectory of the interaction at a given position is seen from this figure. The calculated Lyapunov exponent for each case is given in the upper right corner of each panel.

The cumulative pictures of the chaotic visits of the consecutively renormalized interactions  $J_{ij}$  at a given position of the system, for a large number of renormalization-group iterations, in the spin-glass phases for different frustrations, is given for  $d = 3$  and 2 respectively in Figs. 2.8 and 2.9. It has been recently shown [31] that these distributions over renormalization-group iterations for a given position in the lattice are completely equivalent to the distributions of interactions across the lattice at a given renormalization-group iteration. As seen in Figs. 2.8 and 9, in the system where frustration is completely removed ( $f = 0$ , uppermost leftside diagrams), the interaction at a given position randomly visits

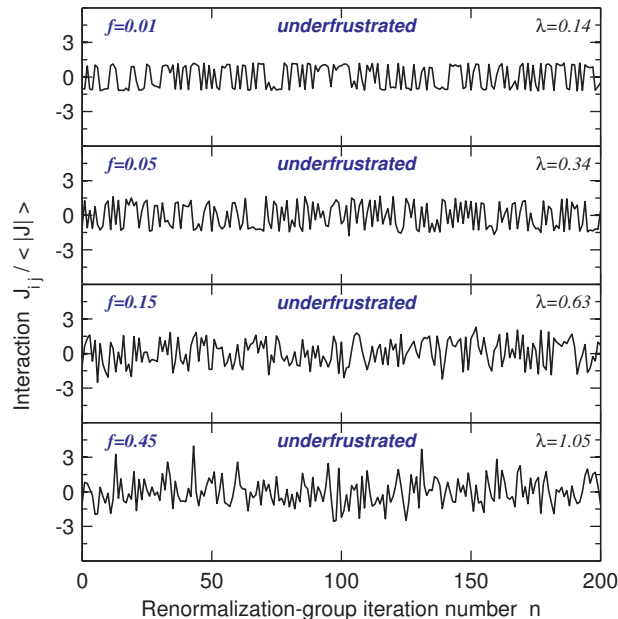


Figure 2.7: (Color online) Interaction at a given position in the lattice at successive renormalization-group iterations, for  $d = 2$  systems with different frustrations. In all cases, the antiferromagnetic bond concentration is  $p = 0.5$  and the initial temperature is  $1/J = 0.2$ , inside the spin-glass phase. For each frustration amount, a chaotic trajectory of the interaction at a given position is seen from this figure. The calculated Lyapunov exponent for each case is given in the upper right corner of each panel.

positive and negative values, giving the two delta functions seen in the figures. When frustration is introduced ( $f$  is increased from 0), these two delta functions broaden into two chaotic bands (seen in the figures for  $f = 0.01$ ), which merge into a double-peaked single band (seen for  $f = 0.10$ ), which transforms into a single peak (seen for  $f = 0.25$ ). In  $d = 3$ , the single-peaked chaotic band continues through the stochastic frustration ( $f = 1 = g$ ) into a range of overfrustrated systems ( $g > 0.67$ ), albeit with varying Lyapunov exponents  $\lambda$ , as seen in the insets and in Fig. 2.10. In  $d = 2$ , the single-peaked chaotic band continues when frustration is increased to  $f = 0.45$  (uppermost rightside diagram), but no spin-glass phase occurs for  $f > 0.49$ , that is to say in overfrustration, stochastic frustration, and the higher range of underfrustration.

The spin-glass phases, being chaotic, can be characterized [31] by **the Lyapunov exponent** of general chaotic behavior [36, 37]. The positivity of the Lyapunov exponent measures the strength of the chaos [36, 37] and was also used



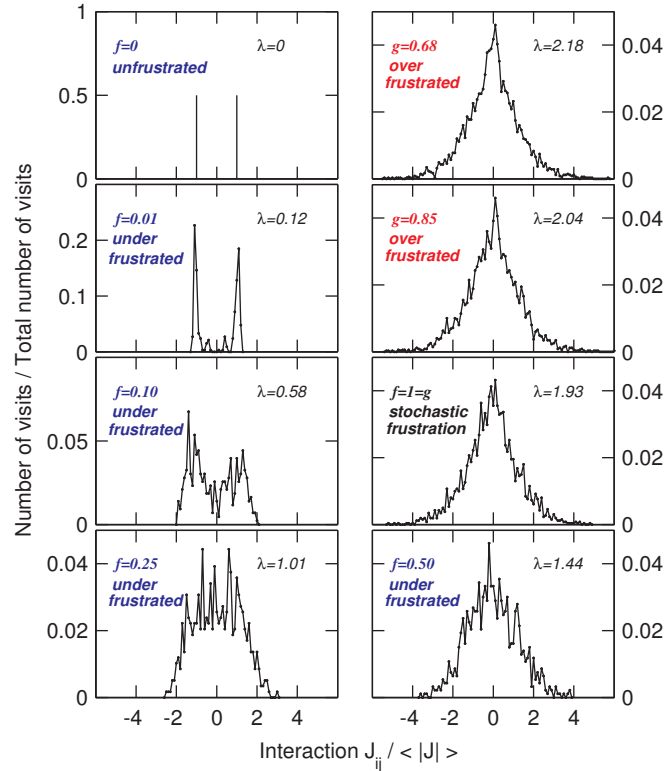


Figure 2.8: (Color online) The chaotic visits of the consecutively renormalized interactions  $J_{ij}$  at a given position of the system, in the spin-glass phase of overfrustrated, underfrustrated, and stochastically frustrated Ising models in  $d = 3$ . These consecutively renormalized interactions at a given position of the system are shown here as scaled with the average interaction  $\langle |J| \rangle$  across the system, which diverges as  $b^{ny_R}$  where  $n$  is the number of renormalization-group iterations and  $y_R > 0$  is the runaway exponent shown in Fig. 2.10. The number of visits into each interval of 0.1 on the horizontal axis have been scaled with the total number of renormalization-group iterations. Between 300 and 3,500 renormalization-group iterations have been used for the different panels. The distributions of chaotic visits shown in the panels stabilize as the number of iterations is increased. The calculated Lyapunov exponent for each case is given in the upper right corner of each panel.

in the previous spin-glass study of Ref.[27]. The calculation of the Lyapunov exponent is applied here to the chaotic renormalization-group trajectory at any specific position in the lattice,

$$\lambda = \lim_{n \rightarrow \infty} \frac{1}{n} \sum_{k=0}^{n-1} \ln \left| \frac{dx_{k+1}}{dx_k} \right| \quad (2.7)$$

where  $x_k = J_{ij} / \langle |J| \rangle$  at step  $k$  of the renormalization-group trajectory. The sum in Eq.(2.6) is to be taken within the asymptotic chaotic band. Thus, we throw

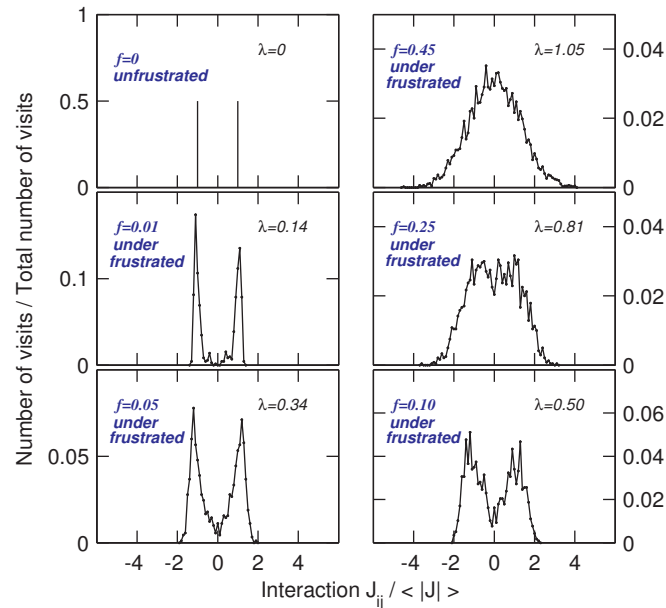


Figure 2.9: (Color online) The chaotic visits of the consecutively renormalized interactions  $J_{ij}$  at a given position of the system, in the spin-glass phase of underfrustrated Ising models in  $d = 2$ . These consecutively renormalized interactions at a given position of the system are shown here as scaled with the average interaction  $\langle |J| \rangle$  across the system, which diverges as  $b^{ny_R}$  where  $n$  is the number of renormalization-group iterations and  $y_R > 0$  is the runaway exponent shown in Fig. 2.10. The number of visits into each interval of 0.1 on the horizontal axis have been scaled with the total number of renormalization-group iterations. Between 700 and 5,000 renormalization-group iterations have been used for the different panels. The distributions of chaotic visits shown in the panels stabilize as the number of iterations is increased. The calculated Lyapunov exponent for each case is given in the upper right corner of each panel. No spin-glass phase occurs for  $f > 0.49$ , as seen in Figs. 2.5 and 2.10.

out the first 100 renormalization-group iterations to eliminate the points outside of, but leading to the chaotic band. Subsequently, typically using up to 2,000 renormalization-group iterations in the sum in Eq.(2.6) assures the convergence of the Lyapunov exponent value. The calculated Lyapunov exponents  $\lambda$  and runaway exponents  $y_R$  of the spin-glass phases of overfrustrated, underfrustrated, and stochastically frustrated Ising models in  $d = 3$  (upper curves) and  $d = 2$  (lower curves) are given in Fig. 2.10. As seen in this figure and in Figs. 2.6-9, as soon as frustration is introduced ( $f > 0$ ), the Lyapunov exponent becomes positive and chaotic behavior occurs inside the spin-glass phase. Upon further increasing frustration, on the other hand, the spin-glass phase disappears when  $y_R$  reaches

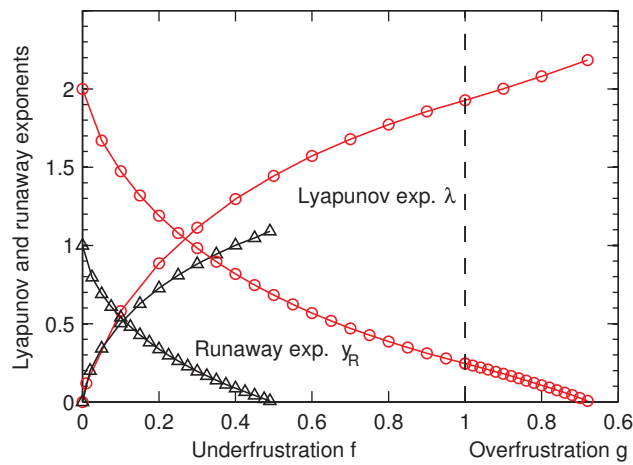


Figure 2.10: (Color online) Lyapunov exponent  $\lambda$  and runaway exponent  $y_R$  of the spin-glass phases of overfrustrated, underfrustrated, and stochastically frustrated Ising models in  $d = 3$  (upper curves) and  $d = 2$  (lower curves). The horizontal scale shows, to the left of the dashed line, the  $f$  values of the underfrustrated cases and, to the right of the dashed line, the  $g$  values of the overfrustrated cases. The dashed line marks the stochastic frustration ( $f = 1 = g$ ). As seen in this figure and in Figs. 2.8 and 2.9, as soon as frustration is introduced, ( $f > 0$ ), the Lyapunov exponent becomes positive and chaotic behavior occurs inside the spin-glass phase. The average interaction  $\langle |J| \rangle$  across the system diverges as  $b^{ny_R}$  where  $n$  is the number of renormalization-group iterations and  $y_R > 0$  is the runaway exponent. The Lyapunov exponent  $\lambda$  monotonically increases with frustration from  $\lambda = 0$  at zero frustration and the runaway exponent  $y_R$  monotonically decreases with frustration from  $y_R = d - 1$  at zero frustration. The spin-glass phase disappears when  $y_R$  reaches zero, for  $g = 0.67$  in  $d = 3$  and  $f = 0.49$  in  $d = 2$ .

zero as seen in Fig. 2.10, for  $g = 0.67$  in  $d = 3$  and  $f = 0.49$  in  $d = 2$ .

## 2.5 Entropy, Short- and Long-Range Order in Overfrustrated and Underfrustrated Spin Glasses

Information about the relative shift and interchange in short- and long-range order can be deduced from entropy and specific heat curves. Short-range order is deduced from a specific heat peak (loss of entropy) that is away from the phase transition. Long-range order is deduced from the phase transition given by the renormalization-group flows. Thus, the characteristic temperature of short-range order is the temperature of the specific heat peak. The characteristic temperature of long-range order is the phase transition temperature. The calculated entropy per site  $S/kN$  and specific heat per site  $C/kN$  are shown in Fig. 2.11 as a function of temperature  $1/J$  at fixed antiferromagnetic bond concentration  $p = 0.5$ , for  $d = 3$  systems with underfrustration ( $f = 0.02, 0.2, 0.5$ ), stochastic frustration ( $f = 1 = g$ ), and overfrustration ( $g = 0.7$ ). The tick mark shows the phase transition point between the spin-glass phase and the paramagnetic phase for each frustration case. As also seen in Fig. 2.5, frustration lowers this transition temperature. For stochastic frustration ( $f = 1 = g$ ), the specific heat peak occurs outside the spin-glass phase, indicating that considerable short-range ordering occurs at higher temperatures before the onset of spin-glass long-range order. By contrast, for low frustration ( $f = 0.02, 0.2$ ), the specific heat peak occurs inside the spin-glass phase, indicating that considerable short-range disorder persists into the higher temperatures of the spin-glass phase. This conclusion is also reached from the entropy curves in the upper panel. The changeover between these two regimes occurs for the underfrustrated system of  $f = 0.5$ . Overfrustrated systems show understandably specific heat behavior similar to  $f = 1$ , with frustration lowering the long-range order temperature and short-range order setting above this temperature with a specific heat peak.

The calculated entropy per site  $S/kN$  as a function of the antiferromagnetic bond concentration  $p$  at fixed temperature  $1/J = 0.5$  is shown in the upper panel of Fig. 2.12 for  $d = 3$  systems with no frustration ( $f = 0$ ), underfrustration

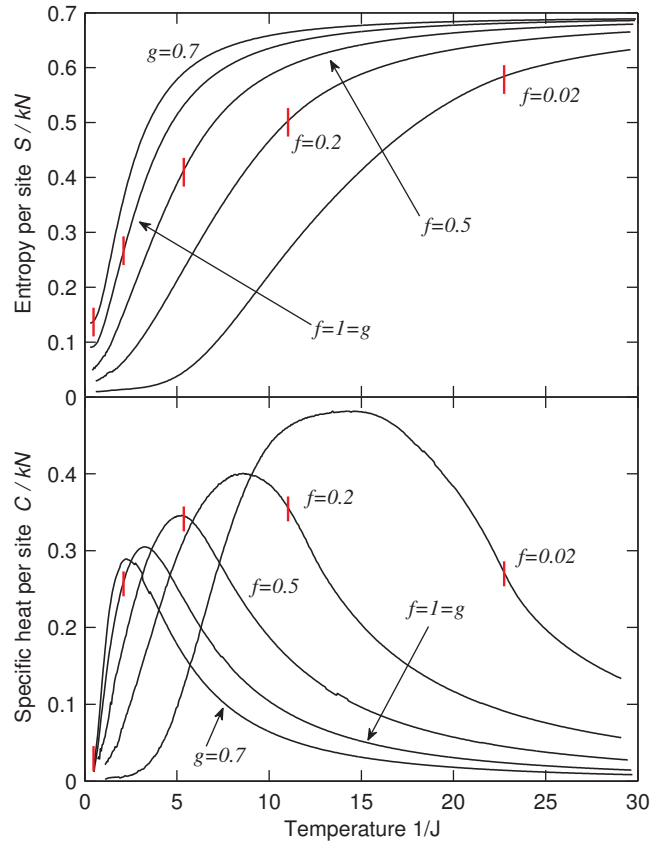


Figure 2.11: (Color online) The calculated entropy per site  $S/kN$  (upper panel) and specific heat per site  $C/kN$  (lower panel) as a function of temperature  $1/J$  at fixed antiferromagnetic bond concentration  $p = 0.5$ , for  $d = 3$  systems with underfrustration ( $f = 0.02, 0.2, 0.5$ ), the stochastic frustration ( $f = 1 = g$ ), and overfrustration ( $g = 0.7$ ). The tick mark shows the phase transition point between the spin-glass phase and the paramagnetic phase for each frustration case. It is seen that frustration lowers this transition temperature. Thus, for stochastic frustration ( $f = 1 = g$ ), the specific heat peak occurs outside the spin-glass phase, indicating that considerable short-range ordering occurs at higher temperatures before the onset of spin-glass long-range order. By contrast, for the more underfrustrated cases ( $f = 0.02, 0.2$ ), the specific heat peak occurs inside the spin-glass phase, indicating that considerable short-range disorder persists into the higher temperatures of the spin-glass phase. This conclusion is also reached from the entropy curves in the upper panel. The changeover between these two regimes occurs at the underfrustrated system of  $f = 0.5$ . Overfrustrated systems show understandably specific heat behavior similar to  $f = 1$ , with frustration lowering the long-range order temperature and short-range order setting at higher temperatures with a specific heat peak.

( $f = 0.5, 0.8$ ), stochastic frustration ( $f = 1 = g$ ), and overfrustration ( $g = 0.8$ ). Frustration is thus introduced at different rates in the different curves in Fig. 2.12. Here the tick mark shows the phase transition point between the ferromagnetic

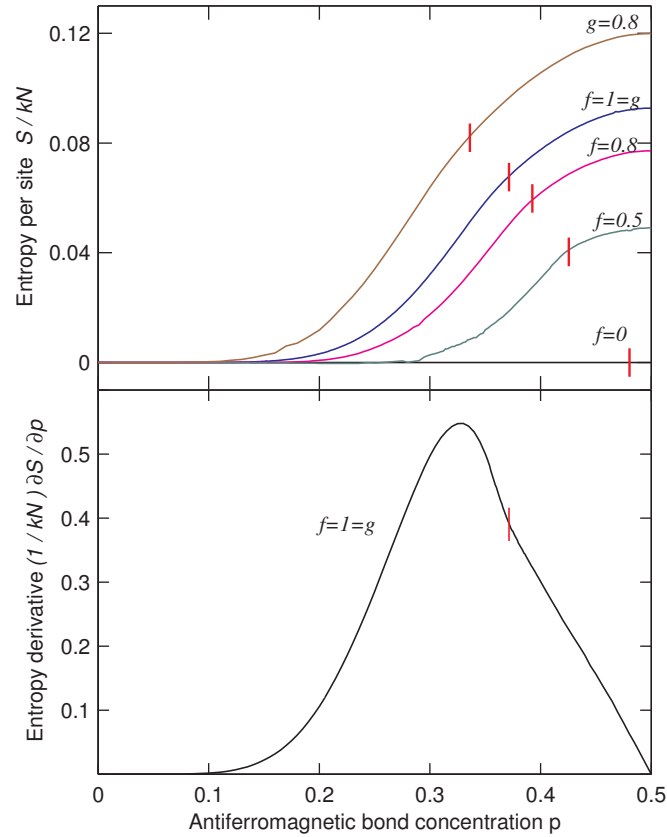


Figure 2.12: (Color online) Top panel: The calculated entropy per site  $S/kN$  as a function of the antiferromagnetic bond concentration  $p$  at fixed temperature  $1/J = 0.5$ , for systems with no frustration ( $f = 0$ ), underfrustration ( $f = 0.5, 0.8$ ), the stochastic frustration ( $f = 1 = g$ ), and overfrustration ( $g = 0.8$ ). The tick mark shows the phase transition point between the ferromagnetic phase and the spin-glass phase for each frustration case. It is seen that frustration favors the spin-glass phase over the ferromagnetic phase. It is also seen that, as soon as frustration is introduced, the major portion of the entropy is created with the ferromagnetic phase as opposed to the spin-glass phase. Lower panel: The calculated derivative of the entropy per site  $(1/kN)(\partial S/\partial p)$  as a function of the antiferromagnetic bond concentration  $p$  at temperature  $1/J = 0.5$ , for the stochastic frustration system ( $f = 1$ ) in  $d = 3$ . The tick mark shows the phase transition point between the ferromagnetic phase and the spin-glass phase. The peak being inside the ferromagnetic phase shows that short-range disorder sets inside the ferromagnetic phase.

phase and the spin-glass phase for each frustration case. It is seen that frustration favors the spin-glass phase over the ferromagnetic phase. It is also seen that, as soon as frustration is introduced, the major portion of the entropy is created with the ferromagnetic phase as opposed to the spin-glass phase. Fig. 2.12 also shows the calculated derivative of the entropy per site  $(1/kN)(\partial S/k\partial p)$  as a function of

the antiferromagnetic bond concentration  $p$  at fixed temperature  $1/J = 0.5$ , for the stochastic frustration system ( $f = 1$ ) in  $d = 3$ . The tick mark again marks the phase transition point between the ferromagnetic phase and the spin-glass phase. The peak being inside the ferromagnetic phase also indicates that short-range disorder sets inside the ferromagnetic phase.

## 2.6 Conclusion

This study has started upon the realization that in Ising spin glasses, frustration can be adjusted continuously and, if needed, considerably, without changing the antiferromagnetic bond probability  $p$ , by using locally correlated quenched randomness, as we demonstrated here on hypercubic lattices and hierarchical lattices. Thus, a rich variety of new spin-glass models and spin-glass phases was created. Such overfrustrated and underfrustrated systems on hierarchical lattices in  $d = 3$  and 2 were studied in detail, yielding new information and insights. With the removal of just 51% of frustration ( $f = 0.49$ ), a spin-glass phase appears in  $d = 2$ . With the addition of just 33% frustration ( $g = 0.67$ ), the spin-glass phase disappears in  $d = 3$ . Sequences of phase diagrams for different levels of frustration have been calculated in both dimensions. In general, frustration lowers the spin-glass ordering temperature. At low temperatures, frustration favors the spin-glass phase (before it disappears) over the ferromagnetic phase and symmetrically the antiferromagnetic phase.

When any amount, including infinitesimal, frustration is introduced, the chaotic rescaling of local interactions occurs in the spin-glass phase. Chaos increases with increasing frustration, as seen from the increased positive value of the calculated Lyapunov exponent, starting from zero when frustration is absent. The calculated runaway exponent of the renormalization-group flows decreases, from  $y_R = d - 1$  with increasing frustration to  $y_R = 0$  when the spin-glass phase disappears.

From our calculations of entropy and specific heat curves in  $d = 3$ , it is seen that frustration lowers in temperature the onset of both long- and short-range order in spin-glass phases, but is more effective on the former. Thus, for highly

overfrustrated cases, considerable short-range order occurs in the lower temperature range of the paramagnetic phase, whereas for moderately overfrustrated, stochastically frustrated, and underfrustrated cases, considerable short-range disorder occurs in the higher temperature of the spin-glass phase. From calculations of the entropy and its derivative as a function of antiferromagnetic bond concentration  $p$ , it is seen that the ground-state and low-temperature entropy already mostly sets in within the ferromagnetic and antiferromagnetic phases, before the spin-glass phase is reached.

It is hoped that these calculational results, strictly valid for hierarchical lattices but suggestive for hypercubic lattices, would be repeated by Monte Carlo simulation, or other methods, for hypercubic lattices, as we have demonstrated the preparation of overfrustrated and underfrustrated hypercubic lattices.



---

## REFERENCES

- [1] H. Nishimori, *Statistical Physics of Spin Glasses and Information Processing* (Oxford University Press, 2001).
- [2] A. N. Berker and L. P. Kadanoff, *J. Phys. A* **13**, L259 (1980).
- [3] A. N. Berker and L. P. Kadanoff, *J. Phys. A* **13**, 3786 (1980).
- [4] S. R. McKay, A. N. Berker, and S. Kirkpatrick, *Phys. Rev. Lett.* **48**, 767 (1982).
- [5] S. R. McKay, A. N. Berker, and S. Kirkpatrick, *J. Appl. Phys.* **53**, 7974 (1982).
- [6] G. Toulouse, *Commun. Phys.* **2**, 115 (1977).
- [7] I. Morgenstern and K. Binder, *Phys. Rev. Lett.* **43**, 1615 (1979).
- [8] D.C. Mattis, *Phys. Lett. A* **56**, 421 (1976)
- [9] D. Blankschtein, M. Ma, and A.N. Berker, *Phys. Rev. B* **30**, 1362 (1984).
- [10] L. W. Bernardi, K. Hukushima, H. Takayama, *J. Phys. A* **32**, 1787 (1999).
- [11] A. K. Murtazaev, I. K. Kamilov, M. K. Ramazanov, *Phys. Solid State* **47**, 1163 (2005).
- [12] H. T. Diep and H. Giacomini in *Frustrated Spin Systems* (World Scientific, 2005), pp.1-58.
- [13] V. Thanh Ngo, D. Tien Hoang, H. T. Diep, *J. Phys. Condensed Matter* **23**, 226002 (2011).
- [14] A. N. Berker and S. R. McKay, *J. Stat. Phys.* **36**, 787 (1984).
- [15] E. J. Hartford and S. R. McKay, *J. Appl. Phys.* **70**, 6068 (1991).
- [16] F. Krzakala, *Europhys. Lett.* **66**, 847 (2004).
- [17] F. Krzakala and J. P. Bouchaud, *Europhys. Lett.* **72**, 472 (2005).
- [18] M. Sasaki, K. Hukushima, H. Yoshino, and H. Takayama, *Phys. Rev. Lett.* **95**, 267203 (2005).

- 
- [19] J. Lukic, E. Marinari, O. C. Martin, and S. Sabatini, *J. Stat. Mech.: Theory Exp.* L10001 (2006).
- [20] P. Le Doussal, *Phys. Rev. Lett.* **96**, 235702 (2006).
- [21] T. Rizzo and H. Yoshino, *Phys. Rev. B* **73**, 064416 (2006).
- [22] H. G. Katzgraber and F. Krzakala, *Phys. Rev. Lett.* **98**, 017201 (2007).
- [23] H. Yoshino and T. Rizzo, *Phys. Rev. B* **77**, 104429 (2008).
- [24] T. Aspelmeier, *Phys. Rev. Lett.* **100**, 117205 (2008).
- [25] T. Aspelmeier, *J. Phys. A* **41**, 205005 (2008).
- [26] T. Mora and L. Zdeborova, *J. Stat. Phys.* **131**, 1121 (2008).
- [27] N. Aral and A. N. Berker, *Phys. Rev. B* **79**, 014434 (2009).
- [28] T. E. Stone and S. R. McKay, *Physics A* **389**, 2911 (2010).
- [29] T. Jörg and F. Krzakala, *J. Stat. Mech.: Theory Exp.* L01001 (2012).
- [30] T. Obuchi and K. Takahashi, *J. Phys. A* **45**, 125003 (2012).
- [31] E. Ilker and A. N. Berker, *Phys. Rev. E* **87**, 032124 (2013).
- [32] F. Roma and S. Risau-Gusman, *Phys. Rev. E* **88**, 042105 (2013).
- [33] W.-K. Chen, *Ann. Prob.* **41**, 3345 (2013).
- [34] L. A. Fernandez, V. Martin-Mayor, G. Parisi, and B. Seoane, *Europhys. Lett.* **103**, 67003 (2013).
- [35] W. de Lima, G. Camelo-Neto, and S. Coutinho, *Phys. Lett. A* **377**, 2851 (2013).
- [36] P. Collet and J.-P. Eckmann, *Iterated Maps on the Interval as Dynamical Systems* (Birkhäuser, Boston, 1980).
- [37] R. C. Hilborn, *Chaos and Nonlinear Dynamics*, 2nd ed. (Oxford University Press, New York, 2003).
- [38] A. A. Migdal, *Zh. Eksp. Teor. Fiz.* **69**, 1457 (1975) [*Sov. Phys. JETP* **42**, 743 (1976)].
- [39] L. P. Kadanoff, *Ann. Phys. (N.Y.)* **100**, 359 (1976).

- 
- [40] A. N. Berker and S. Ostlund, *J. Phys. C* **12**, 4961 (1979).
- [41] R. B. Griffiths and M. Kaufman, *Phys. Rev. B* **26**, 5022R (1982).
- [42] M. Kaufman and R. B. Griffiths, *Phys. Rev. B* **30**, 244 (1984).
- [43] S. R. McKay and A. N. Berker, *Phys. Rev. B* **29**, 1315 (1984).
- [44] M. Hinczewski and A. N. Berker, *Phys. Rev. E* **73**, 066126 (2006).
- [45] D. Andelman and A. N. Berker, *Phys. Rev. B* **29**, 2630 (1984).
- [46] M. J. P. Gingras and E. S. Sørensen, *Phys. Rev. B* **46**, 3441 (1992).
- [47] G. Migliorini and A. N. Berker, *Phys. Rev. B* **57**, 426 (1998).
- [48] M. J. P. Gingras and E. S. Sørensen, *Phys. Rev. B* **57**, 10264 (1998).
- [49] M. Hinczewski and A.N. Berker, *Phys. Rev. B* **72**, 144402 (2005).
- [50] C. Güven, A. N. Berker, M. Hinczewski, and H. Nishimori, *Phys. Rev. E* **77**, 061110 (2008).
- [51] G. Gülpınar and A. N. Berker, *Phys. Rev. E* **79**, 021110 (2009).
- [52] S.-C. Chang and R. Shrock, *Phys. Lett. A* **377**, 671 (2013).
- [53] R. F. S. Andrade and H. J. Herrmann, *Phys. Rev. E* **87**, 042113 (2013).
- [54] R. F. S. Andrade and H. J. Herrmann, *Phys. Rev. E* **88**, 042122 (2013).
- [55] C. Monthus and T. Garel, *J. Stat. Phys.-Theory and Experiment*, P06007 (2013).
- [56] O. Melchert and A. K. Hartmann, *Eur. Phys. J. B* **86**, 323 (2013).
- [57] J.-Y. Fortin, *J. Phys.-Condensed Matter* **25**, 296004 (2013).
- [58] Y. H. Wu, X. Li, Z. Z. Zhang, and Z. H. Rong, *Chaos Solitons Fractals* **56**, 91 (2013).
- [59] M. E. Fisher and A. N. Berker, *Phys. Rev. B* **26**, 2507 (1982).
- [60] S. B. Roy and M. K. Chattopadhyay, *Phys. Rev. B* **79**, 052407 (2009).
- [61] J. O. Indekeu and A. N. Berker, *Physica A (Utrecht)* **140**, 368 (1986).
- [62] R. R. Netz and A. N. Berker, *Phys. Rev. Lett.* **68**, 333 (1992).

- 
- [63] M. G. Mazza and M. Schoen, *Int. J. Mol. Sci.* **12**, 5352 (2011).
- [64] S. Chen, H.-B. Luo, H.-L. Xie, and H. L. Zhang, *J. Polymer Sci. A* **51**, 924 (2013).
- [65] H. Nishimori, *Prog. Theor. Phys.* **66**, 1169 (1981).
- [66] H. Nishimori and K. Nemoto, *J. Phys. Soc. Jpn.* **71**, 1198 (2002).
- [67] J.-M. Maillard, K. Nemoto, and H. Nishimori, *J. Phys. A* **36**, 9799 (2003).
- [68] K. Takeda and H. Nishimori, *Nucl. Phys. B* **686**, 377 (2004).
- [69] K. Takeda, T. Sasamoto, and H. Nishimori, *J. Phys. A* **38**, 3751 (2005).

Chapter 3

**HIGH Q-STATE CLOCK SPIN GLASSES**

### 3.1 Introduction

Spin-glass phases, with randomly frozen local order [1] and chaotic behavior under scale change [2, 3, 4], reflecting the effects of frozen interaction disorder, competition, and frustration, remain a uniquely fascinating and broadly relevant subject of statistical mechanics and condensed matter physics. However, the large and richly complex amount of theoretical knowledge produced on spin glasses has been overwhelmingly derived from Ising, i.e.,  $s_i = \pm 1$ , spin models.[5]

By contrast, we present here a detailed renormalization-group study of spin-glass phases and phase transitions, for  $q$ -state clock models and their  $q \rightarrow \infty$  limit the XY model, in spatial dimension  $d = 3$ . We note that, in addition to the now well-established chaotic behavior of the spin-glass phase [2, 3, 4, 6, 7, 8, 9, 10, 11, 12, 13, 14, 15, 16, 17, 18, 19, 20, 21, 22, 23, 24, 25], each of the two types of spin-glass phase boundaries displays, under renormalization-group trajectories, their own distinctive chaotic behavior. We see that these chaotic renormalization-group trajectories subdivide into two categories, namely as strong-coupling chaos (in the spin-glass phase and, distinctly, on the spinglass-ferromagnetic phase boundary) and as intermediate-coupling chaos (on the spinglass-paramagnetic phase boundary). We thus quantitatively characterize each different phase and phase boundary exhibiting chaos by its distinct Lyapunov exponent as used in the general chaotic studies literature [26, 27], which we calculate. We show that, under renormalization-group, chaotic trajectories and fixed distributions are mechanistically and quantitatively equivalent.

We calculate and display the phase diagrams of arbitrary even  $q$ -state clock spin-glass models in  $d = 3$ . These models, for any non-infinite  $q$ , have a finite-temperature spin-glass phase. Furthermore, we find that the spin-glass phases exhibit a universal ordering behavior, independent of  $q$ . The spin-glass phases and the spinglass-paramagnetic phase boundary exhibit universal fixed distributions, chaotic trajectories and Lyapunov exponents. In the  $d = 3$  XY model limit, our calculations indicate a zero-temperature spin-glass phase.

### 3.2 The $q$ -state clock spin-glass model and the renormalization-group method

The  $q$ -state clock models are composed of unit spins that are confined to a plane and that can only point along  $q$  angularly equidistant directions. Accordingly, the  $q$ -state clock spin-glass model is defined by the Hamiltonian

$$-\beta\mathcal{H} = \sum_{\langle ij \rangle} J_{ij} \vec{s}_i \cdot \vec{s}_j = \sum_{\langle ij \rangle} J_{ij} \cos(\theta_i - \theta_j), \quad (3.1)$$

where  $\beta = 1/k_B T$ , at site  $i$  the spin angle  $\theta_i$  takes on the values  $(2\pi/q)\sigma_i$  with  $\sigma_i = 0, 1, 2, \dots, q-1$ , and  $\langle ij \rangle$  denotes that the sum runs over all nearest-neighbor pairs of sites. The bond strengths  $J_{ij}$  are  $+J > 0$  (ferromagnetic) with probability  $1-p$  and  $-J$  (antiferromagnetic) with probability  $p$ . This model becomes the Ising model for  $q=2$  and the XY model for  $q \rightarrow \infty$ .

The  $q$ -state clock spin-glass model, in  $d = 3$  dimensions, is readily solved by a renormalization-group method that is approximate on the cubic lattice [28, 29] and simultaneously exact on the hierarchical lattice [30, 31, 32, 33, 34]. Under rescaling, for  $q > 4$ , the form of the interaction as given in the rightmost side of Eq.(3.1) is not conserved and one must therefore express the Hamiltonian more generally, as

$$-\beta\mathcal{H} = \sum_{\langle ij \rangle} V(\theta_i - \theta_j). \quad (3.2)$$

Thus, the renormalization-group flows, for even  $q$ , are the flows of  $1 + q/2$  interaction constants. With no loss of generality, the maximum value of  $V(\theta_i - \theta_j)$  is set to zero.

The renormalization-group transformation, for spatial dimensions  $d = 3$  and length rescaling factor  $b = 3$  (necessary for treating the ferromagnetic and anti-ferromagnetic correlations on equal footing), is achieved by a sequence of bond moving

$$V_{bm}(\theta_1 - \theta_2) + G_{12} = \sum_{n=1}^{b^{d-1}} V_n(\theta_1 - \theta_2) \quad (3.3)$$

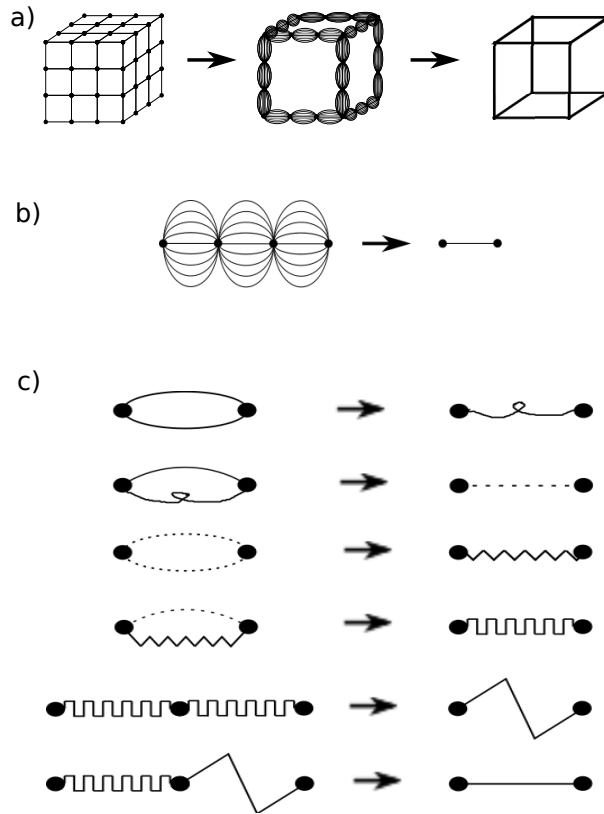


Figure 3.1: (a) Migdal-Kadanoff approximate renormalization-group transformation for the  $d = 3$  cubic lattice with the length-rescaling factor of  $b = 3$ . Bond-moving is followed by decimation. (b) Exact renormalization-group transformation for the equivalent  $d = 3$  hierarchical lattice with the length-rescaling factor of  $b = 3$ . (c) Pairwise applications of the quenched probability convolution of Eq.(3.5), leading to the exact transformation in (b).

and decimation

$$e^{V_{dec}(\theta_1 - \theta_4) + G_{14}} = \sum_{\theta_2, \theta_3} e^{V_1(\theta_1 - \theta_2) + V_2(\theta_2 - \theta_3) + V_3(\theta_3 - \theta_4)}, \quad (3.4)$$

where the constants  $G_{ij}$  are fixed by the requirement that the maximum value of  $V(\theta_i - \theta_j)$  is zero.

The starting bimodal quenched probability distribution of the interactions, characterized by  $p$  and described above, is also not conserved under rescaling. The renormalized quenched probability distribution of the interactions is obtained



by the convolution [35]

$$P'(V'(\theta_{i'j'})) = \int \left[ \prod_{ij}^{i'j'} dV(\theta_{ij}) P(V(\theta_{ij})) \right] \delta(V'(\theta_{i'j'}) - R(\{V(\theta_{ij})\})), \quad (3.5)$$

where  $R(\{V(\theta_{ij})\})$  represents the bond moving and decimation given in Eqs.(3.3) and (3.4). For numerical practicality, the bond moving and decimation of Eqs.(3.3) and (3.4) are achieved by a sequence of pairwise combination of interactions, as shown in Fig. 3.1(c), each pairwise combination leading to an intermediate probability distribution resulting from a pairwise convolution as in Eq.(3.5). We effect this procedure numerically, by generating 5,000 interactions that embody the quenched probability distribution resulting from each pairwise combination. Each of the generated 5,000 interactions is determined by  $1 + q/2$  interaction constants. At each pairwise convolution as in Eq.(3.5), 5,000 randomly chosen pairs are matched by Eq.(3.3) or (3.4), and a new set of 5,000 is produced. We have checked that our results are insensitive to further increasing the number 5,000. Furthermore, our calculated phase diagrams exactly match, for  $q = 2$ , the results in Refs.[36, 37, 38, 39] which are numerically exact by the use of the histogram representation of the quenched probability distribution.

The different thermodynamic phases of the model are identified by the different asymptotic renormalization-group flows of the quenched probability distributions. For all renormalization-group flows, inside the phases and on the phase boundaries, Eq.(3.5) is iterated until asymptotic behavior is reached, meaning that we are studying an effectively infinite hierarchical lattice. Thus, we are able to calculate phase diagrams for any number of clock states  $q$ . Our results are obtained by averaging over 30 to 50 different realizations of the initial  $\pm J \cos(\theta_i - \theta_j)$  distribution into the 5,000 initial interactions. In this study, we consider even values of  $q$  and the calculated phase diagrams are symmetric around  $p = 0.5$  with the antiferromagnetic phase replacing the ferromagnetic phase, so that only the  $p = 0$  to 0.5 halves are shown below. If  $q$  is odd, the system does not have sublattice spin-reversal symmetry, which leads to asymmetric phase diagrams.

### 3.3 Calculated phase diagrams for $d = 3$ $q$ -state clock and XY spin glasses

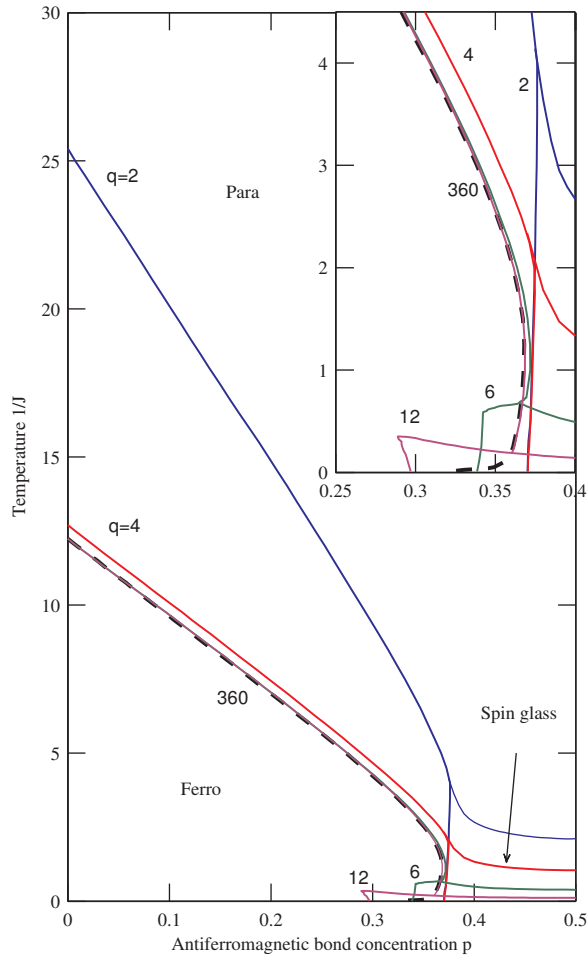


Figure 3.2: (Color online) Calculated phase diagrams of the  $q = 2, 4, 6, 12$  clock spin-glass models in  $d = 3$  dimensions. The phase diagram for the XY limit, namely  $q \rightarrow \infty$ , is also shown, by the dashed curve, calculated here with  $q = 360$  clock states. As  $q$  is increased, it is found that the spin-glass phase retreats to lower temperatures while further protruding into the ferromagnetic phase. In the XY limit, the spin-glass phase disappears at zero temperature (see Fig. 3.4 below), as the phase boundary between the remaining ferromagnetic and paramagnetic phases numerically stabilizes, on the scale of the figure, for  $q \gtrsim 6$ .

Our calculated phase diagrams for the  $q = 2, 4, 6, 12$  clock spin-glass models are shown together in Fig. 3.2. The phase diagram for the XY limit, namely  $q \rightarrow \infty$ , is also shown in Fig. 3.2, calculated here with  $q = 360$  clock states.

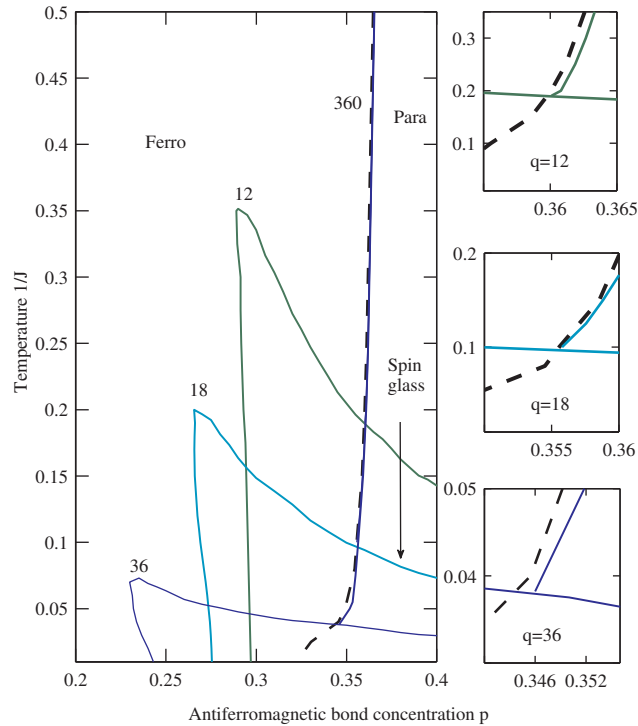


Figure 3.3: (Color online) Phase diagrams of the  $q = 12, 18, 36$  clock spin-glass models in  $d = 3$  dimensions. Two new phenomena are simultaneously detected here: (1) double reentrance: paramagnetic-ferromagnetic-spin-glass-ferromagnetic as temperature is lowered, (2) lateral reentrance: ferromagnetic-spin-glass-ferromagnetic-paramagnetic as  $p$  is increased. The XY limit is given, calculated here with  $q = 360$  clock states, by the dashed curve. The panels on the right show the region of the multicritical point, where the three phase boundary lines meet, for each  $q$  case along with the ferromagnetic-paramagnetic phase boundary of the XY limit.

In this limit, the spin-glass phase disappears at zero temperature, whereas the phase boundary between the ferromagnetic and paramagnetic phases numerically stabilizes, on the scale of the figure, for  $q \gtrsim 6$ . The paramagnetic-ferromagnetic-spin-glass reentrance as temperature is lowered, previously seen [36, 40] for  $q = 2$ , namely the Ising case, is also seen here for the other  $q$ . As  $q$  is increased, it is found that the spin-glass phase retreats to lower temperatures while further protruding into the ferromagnetic phase.

The calculated phase diagrams for the high- $q$  models,  $q = 12, 18, 36, 360$ , are shown in Fig. 3.3. As  $q$  is increased, the trend mentioned above, of the spin-glass phase retreating to lower temperatures while further protruding into

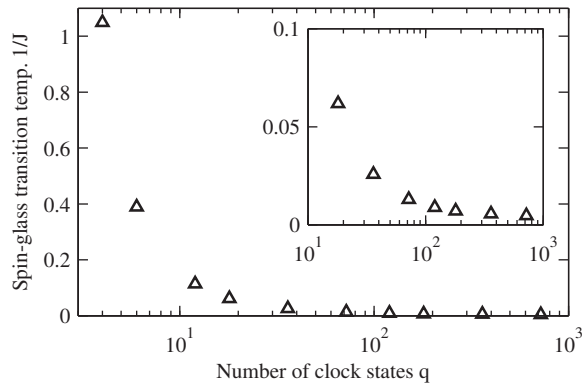


Figure 3.4: The calculated transition temperatures between the spin-glass phase and the paramagnetic phase, at  $p = 0.5$ , as a function of  $q$ , up to very large values of  $q = 720$ . Note the logarithmic scale of the horizontal axes. The slow decay of the transition temperature suggests that a zero-temperature spin-glass phase exists in the ( $q \rightarrow \infty$ ) XY model limit.

the ferromagnetic phase, is also seen here. Furthermore, two new phenomena are simultaneously detected here: (1) double reentrance, namely paramagnetic-ferromagnetic-spin-glass-ferromagnetic phases as temperature is lowered; (2) lateral reentrance, namely ferromagnetic-spin-glass-ferromagnetic-paramagnetic phases as  $p$  is increased. Multiple reentrances have previously been seen in liquid crystal systems.[41, 42, 43]

The (slow) disappearance of the  $q$ -state clock spin-glass phase is shown in Fig. 3.4, where the calculated spin-glass transition temperatures at  $p = 0.5$  are shown as a function of  $q$ , up to very large values of  $q = 720$ . The slow decay of the transition temperature suggests that a zero-temperature spin-glass phase [44] exists in the  $q \rightarrow \infty$ , namely XY model limit, in agreement with the previous Monte Carlo study of Ref.[19].

### 3.4 Stable fixed distribution and chaotic renormalization-group trajectory of clock spin-glass phases

#### 3.4.1 Stable fixed distribution

For the spin-glass phase of the Ising model ( $q = 2$ ), under repeated renormalization-group transformations, the quenched probability distribution of

the interactions across the system becomes symmetric in ferromagnetic ( $J_{ij} > 0$ ) and antiferromagnetic ( $J_{ij} < 0$ ) couplings, with the average magnitude of either type of interaction equal and diverging to infinity.[36]

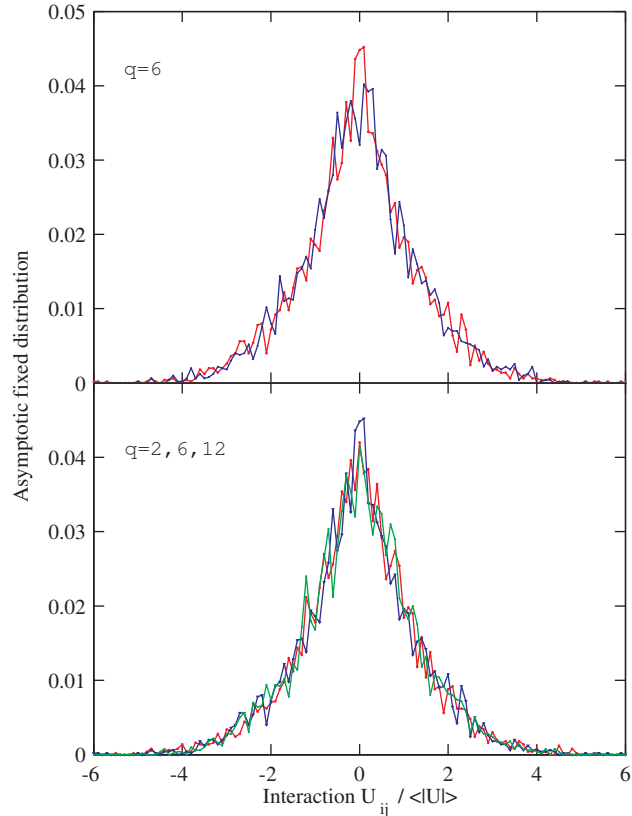


Figure 3.5: (Color online) Asymptotic fixed distribution, under renormalization-group transformations, of the interactions in the spin-glass phase, namely the renormalization-group sink of the spin-glass phase. Note that these are strong-coupling distributions, as the average interaction strength  $\langle |U| \rangle$  diverges to infinity under the renormalization-group transformations. The divergence of  $\langle |U| \rangle$  is as  $b^{0.24n}$ , where  $n$  is the number of iterations. Top: For the  $q = 6$ -state clock model in  $d = 3$ , for a trajectory starting in the spin-glass phase at  $p = 0.5$  and temperature  $1/J = 0.05$ , the distributions after 20 and 21 renormalization-group steps are shown. It is seen that these two distributions coincide, signifying a fixed distribution. Bottom: Asymptotic fixed distributions of the spin-glass phases for the  $q = 2$  (Ising), 6, 12-state clock models in  $d = 3$ . These distributions are reached after 20 renormalization-group steps, starting at  $p = 0.5$  and temperature  $1/J = 0.05$ . Note that the spin-glass sink fixed distributions for different values of  $q$  coincide. The Lyapunov exponent is  $\lambda = 1.93$  for the single, universal distribution that is illustrated in this figure.

For the spin-glass phases of all  $q$ -state clock models, we find that under repeated

renormalization-group transformations, the interaction values  $V_{ij}(\theta)$  divide into two groups:  $\theta = 2\pi n/q$  and  $\theta = 2\pi m/q$ , where  $n$  is an even integer,  $n=0,2,4,\dots,q-2$ , and  $m$  is an odd integer,  $m=1,3,5,\dots,q-1$ . The asymptotic renormalized quenched distribution of the interactions is symmetric, with interactions equal within each group mentioned above, but at each location overwhelmingly favoring one or the other of the two groups. Thus, the interaction difference between the two groups,

$$\frac{1}{q/2} \sum_{n=0,2,\dots}^{q-2} V_{ij}(2\pi n/q) - \frac{1}{q/2} \sum_{m=1,3,\dots}^{q-1} V_{ij}(2\pi m/q) \equiv U_{ij}, \quad (3.6)$$

after many renormalization-group transformations, is randomly and equally distributed as positive or negative in our sampling of 5,000 interactions, which represent the distribution of interactions spatially across the system, with the average magnitude of either type of interaction equal and diverging to infinity as  $b^{0.24n}$ , where  $n$  is the number of iterations. This asymptotic fixed distribution, namely the sink of the spin-glass phase, is shown in Fig. 3.5. Note that this asymptotic behavior is also consistent with the behavior of the Ising spin-glass phase ( $U$  reduces to  $J$  for the Ising case), recalled at the beginning of this section. This behavior leaves the system asymptotically frustrated.

### 3.4.2 Chaotic renormalization-group trajectory

The fact that the Ising spin-glass phase is characterized by the chaotic rescaling behavior of the interactions [2, 3, 4], and therefore of the correlations [23], is now well established [2, 3, 4, 6, 7, 8, 9, 10, 11, 12, 13, 14, 15, 16, 17, 18, 19, 20, 21, 22, 23, 24, 25] and is also seen here for the spin-glass phases of the  $q$ -state clock models in  $d = 3$ , as shown in Fig. 3.5. As with the Ising model [7], we have here a strong-coupling chaotic behavior: The values of the interaction difference  $U_{ij}$  obtained by successive renormalization-group transformations at any specific location, divided by the average magnitude  $\langle |U| \rangle$  across the system, fall into a chaotic band. Thus, the  $U_{ij}/\langle |U| \rangle$  values are sampled within the band as shown in Fig. 3.5. The average magnitude  $\langle |U| \rangle$  diverges to infinity under repeated renormalization-group transformations, as  $b^{0.24n}$ , where  $n$  is the number

of iterations.

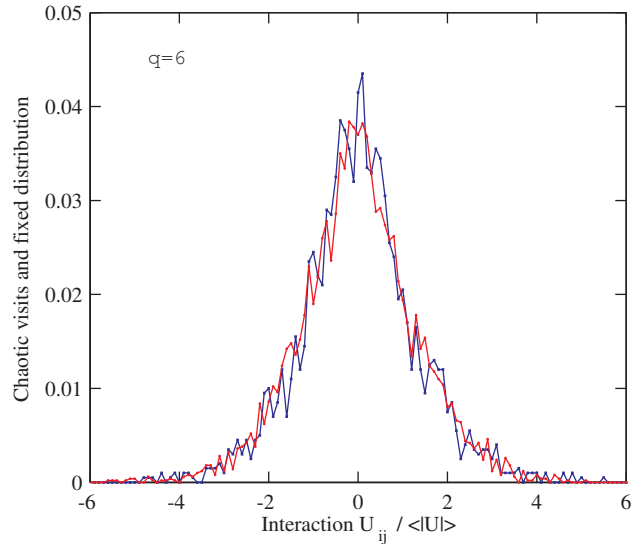


Figure 3.6: (Color online) Comparison, showing the coincidence, of the chaotic visits of the consecutively renormalized interactions at a given position of the system (for 2,000 renormalization-group iterations) and of the asymptotic distribution of the interactions across the system at a given renormalization-group step, for the spin-glass phase. The Lyapunov exponent is  $\lambda = 1.93$ . Identical asymptotic behavior occurs for all  $q$ -state clock spin-glass phases, as shown in Fig. 3.5. The divergence of  $\langle |U| \rangle$  is as  $b^{0.24n}$ , where  $n$  is the number of iterations.

We thus realize that the spin-glass phases can be characterized by the Lyapunov exponent of general chaotic behavior [26, 27]. The positivity of the Lyapunov exponent measures the strength of the chaos [26, 27] and was also used in the previous spin-glass study of Ref.[23]. The calculation of the Lyapunov exponent is applied here to the chaotic renormalization-group trajectory at any specific location in the lattice,

$$\lambda = \lim_{n \rightarrow \infty} \frac{1}{n} \sum_{k=0}^{n-1} \ln \left| \frac{dx_{k+1}}{dx_k} \right| \quad (3.7)$$

where  $x_k = U_{ij} / \langle |U| \rangle$  at step  $k$  of the renormalization-group trajectory. The sum in Eq.(3.7) is to be taken within the asymptotic chaotic band. Thus, we throw out the first 100 renormalization-group iterations to eliminate the points outside of, but leading to the chaotic band. Subsequently, typically using 2,000 renormalization-group iterations in the sum in Eq.(3.7) assures the convergence of the Lyapunov exponent value. We have calculated the Lyapunov exponent

$\lambda = 1.93$  for the clock spin-glass phases of  $q = 2, 6, 12$  and presumably for the clock spin-glass phases of all  $q$ , which is to be expected since all  $q$  spin-glass phases renormalize to the same chaotic band, as seen in Fig. 3.5.

### 3.4.3 Equivalence of the chaotic renormalization-group trajectory and the quenched probability fixed distribution

The distributions of the interaction difference  $U_{ij}$  values shown in Figs. 3.5 and 3.6, respectively obtained as the spatial distribution across the system after many renormalization-group transformations and the values obtained by successive renormalization-group transformations at a specific location in the system, are in fact identical, as seen in Fig. 3.6. Thus, it is understood that the asymptotic fixed distribution is realized, after a given number of renormalization-group transformations, by the interactions at different locations being at different points of the same chaotic trajectory.

## 3.5 Unstable fixed distributions and chaotic renormalization-group trajectories of the clock spinglass-paramagnetic and spinglass-ferromagnetic boundaries

We find that the points on the various spin-glass phase boundaries also renormalize to a fixed distribution of the quenched interactions across the system and, equivalently, to a chaotic renormalization-group trajectory of the interaction at any single location in the lattice. The difference between the asymptotic rescaling behaviors inside the spin-glass phase and on the spin-glass phase boundaries is that, under rescaling transformations, the fixed distribution and the chaotic trajectory are reached in a stable manner, with respect to initial conditions, for the spin-glass phase and are conversely unstable for the spin-glass phase boundaries. The ferromagnetic-paramagnetic phase boundary renormalizes to the pure ferromagnetic system, where an unstable fixed point determines the critical exponent, differently for each  $q$ .



### 3.5.1 The spinglass-paramagnetic phase boundary

The phase boundary between the spin-glass and paramagnetic phases renormalizes to the fixed distribution and chaotic renormalization-group trajectory shown in Fig. 3.7. The interaction grouping, under rescaling, described before Eq.(3.6) also happens. However, this behavior here occurs at finite coupling  $\langle |U| \rangle = 0.686$  for all  $q$ , in contrast to the asymptotic behaviors of the spin-glass phase (given above) and of the spinglass-ferromagnetic phase boundary (given below), which occur at strong coupling  $\langle |U| \rangle \rightarrow \infty$ .

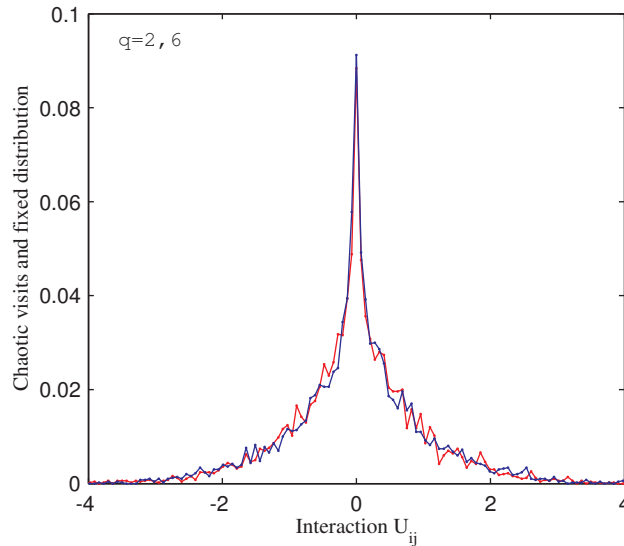


Figure 3.7: (Color online) The fixed distribution and, equivalently, chaotic renormalization-group trajectory onto which the phase boundary between the spin-glass and paramagnetic phases renormalizes, for the  $q = 2$  and  $q = 6$ -state clock models in  $d = 3$ . The Lyapunov exponent is  $\lambda = 1.35$ . Identical asymptotic behavior occurs for all  $q$ . Note that the chaotic behavior and fixed distribution are at intermediate coupling strength, with  $\langle |U| \rangle = 0.686$  for all  $q$ .

### 3.5.2 The spinglass-ferromagnetic phase boundary

The phase boundary between the spin-glass and ferromagnetic phases renormalizes to a fixed distribution and chaotic renormalization-group trajectory at strong coupling  $\langle |U| \rangle \rightarrow \infty$ . The interaction grouping, under rescaling, described before Eq.(3.6) does not happen. Thus, the interaction  $V(\theta)$  as a function of  $\theta$  has

$1 + q/2$  different values. The asymptotic fixed distribution for  $q = 2$  is shown in Fig. 3.8 and is characterized by the Lyapunov exponent  $\lambda = 1.69$ . The divergence of  $\langle |U| \rangle$  is as  $b^{0.46n}$ , where  $n$  is the number of iterations.

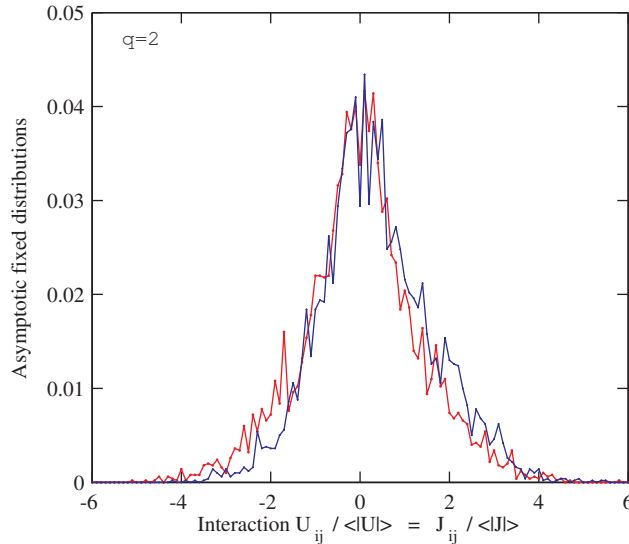


Figure 3.8: (Color online) Two different, non-coinciding strong-coupling fixed distributions: The fixed distribution and, equivalently, chaotic renormalization-group trajectory onto which the spinglass-ferromagnetic phase boundary of the  $q = 2$ -state model in  $d = 3$  renormalizes. For comparison and distinction, the asymptotic fixed distribution and chaotic renormalization-group trajectory of the corresponding spin-glass phase is also shown. The latter curve is symmetric around  $U_{ij} / \langle |U| \rangle = 0$ , whereas the former curve is noticeably displaced towards positive (ferromagnetic) interaction values. Note that these are strong-coupling distributions and are therefore shown as a fraction of the diverging  $\langle |U| \rangle$ . The divergence of  $\langle |U| \rangle$  is as  $b^{0.46n}$  and  $b^{0.24n}$ , where  $n$  is the number of iterations, respectively for the phase boundary and phase sink cases. Thus, even small shifts in the shown curves signify large differences in the interaction values. The Lyapunov exponents are  $\lambda = 1.69$  and  $1.93$ , respectively for the phase boundary and phase sink cases. For  $q = 2$ , the form of the interaction in Eq.(3.1) is conserved under renormalization, which is reflected in the horizontal axis label here.

The asymptotic fixed distribution for  $q = 6$  is shown in Fig. 3.9. The full fixed distribution has the form  $P(\{V(0), V(60), V(120), V(180)\})$ , as a coupled function of its arguments. The dominant configurations of this fixed distribution are shown in Table 3.1. The system remains frustrated at all length scales.

Weight in fixed dist.	$e^{V(0)}$	$e^{V(60)}$	$e^{V(120)}$	$e^{V(180)}$
0.4802	1	0	0	0
0.3951	0	1	0	0
0.1139	1	0	1/2	0
0.0108	0	1	0	2/3

Table 3.1: Dominant potentials in the asymptotic fixed distribution of the phase boundary between the spin-glass and ferromagnetic phases of the  $q = 6$  clock model in  $d = 3$ . Thus, the system remains frustrated at all length scales.

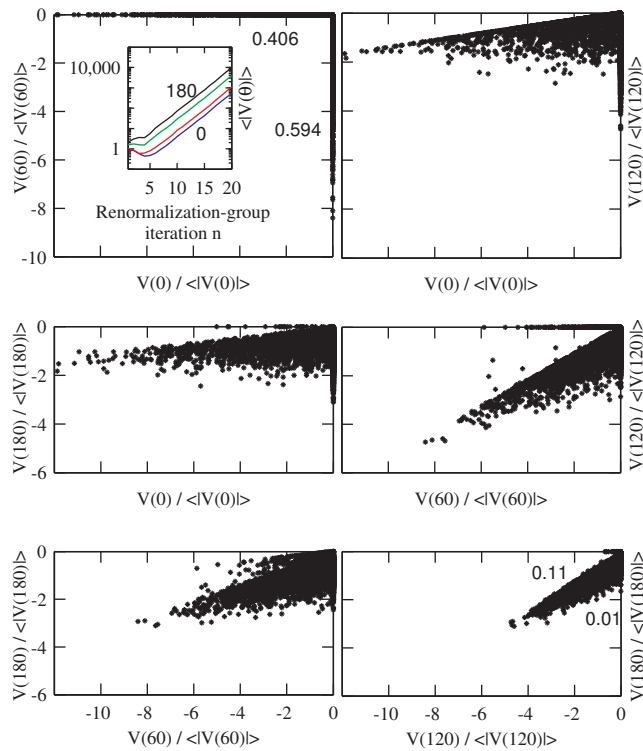


Figure 3.9: The fixed distribution and, equivalently, chaotic renormalization-group trajectory onto which the spinglass-ferromagnetic phase boundary of the  $q = 6$ -state clock model in  $d = 3$  renormalizes. The coupled distributions of the interactions  $V(\theta)/\langle |V(\theta)| \rangle$  are shown, while next to each axis, the fraction of points on the axis are given. The full fixed distribution has the form  $P(\{V(0), V(60), V(120), V(180)\})$ , as a coupled function of its arguments. This is a strong-coupling behavior: The inset in the upper left panel shows, with the logarithmic vertical scale, the diverging  $\langle |V(\theta)| \rangle$  as a function of renormalization-group iteration  $n$ , the consecutive curves being for  $\theta = 180, 120, 60, 0$ . It is seen that, for all  $\theta$ ,  $\langle |V(\theta)| \rangle$  diverges as  $b^{0.46n}$ , where  $n$  is the number of iterations.

### 3.6 Conclusion

We have calculated, from renormalization-group theory, the phase diagrams of arbitrary even  $q$ -state clock spin-glass models in  $d = 3$ . These models, for all non-infinite  $q$ , have a finite-temperature spin-glass phase, exhibiting a universal ordering behavior, independent of  $q$ . In addition to the chaotic rescaling behavior of the spin-glass phase, each of the two types of spin-glass phase boundaries displays, under renormalization-group trajectories, their own distinctive chaotic behavior, subdividing into two categories: strong-coupling chaos, in the spin-glass phase and distinctly on the spinglass-ferromagnetic phase boundary, and intermediate-coupling chaos, on the spinglass-paramagnetic phase boundary. We uniquely characterize each different phase and phase boundary exhibiting chaos by its distinct Lyapunov exponent from general chaos studies, which we calculate. We demonstrate that, under renormalization-group, chaotic trajectories and fixed distributions are mechanistically and quantitatively equivalent. The spin-glass phases and the spinglass-paramagnetic phase boundaries exhibit universal fixed distributions, chaotic trajectories and Lyapunov exponents. In the XY model limit, our calculations indicate a zero-temperature spin-glass phase.

## REFERENCES

- [1] H. Nishimori, *Statistical Physics of Spin Glasses and Information Processing* (Oxford University Press, 2001).
- [2] S. R. McKay, A. N. Berker, and S. Kirkpatrick, *Phys. Rev. Lett.* **48**, 767 (1982).
- [3] S. R. McKay, A. N. Berker, and S. Kirkpatrick, *J. Appl. Phys.* **53**, 7974 (1982).
- [4] A. N. Berker and S. R. McKay, *J. Stat. Phys.* **36**, 787 (1984).
- [5] For two applications to quantum Heisenberg spin glasses, see C. N. Kaplan and A. N. Berker, *Phys. Rev. Lett.* **100**, 027204 (2008); P. C. Menezes and A. Theumann, *Phys. Rev. B* **78**, 054444 (2008)
- [6] A. J. Bray and M. A. Moore, *Phys. Rev. Lett.* **58**, 57 (1987).
- [7] E. J. Hartford and S. R. McKay, *J. Appl. Phys.* **70**, 6068 (1991).
- [8] M. Nifle and H. J. Hilhorst, *Phys. Rev. Lett.* **68**, 2992 (1992).
- [9] M. Nifle and H. J. Hilhorst, *Physica A* **194**, 462 (1993).
- [10] M. Cieplak, M. S. Li, and J. R. Banavar, *Phys. Rev. B* **47**, 5022 (1993).
- [11] F. Krzakala, *Europhys. Lett.* **66**, 847 (2004).
- [12] F. Krzakala and J. P. Bouchaud, *Europhys. Lett.* **72**, 472 (2005).
- [13] M. Sasaki, K. Hukushima, H. Yoshino, and H. Takayama, *Phys. Rev. Lett.* **95**, 267203 (2005).
- [14] J. Lukic, E. Marinari, O. C. Martin, and S. Sabatini, *J. Stat. Mech.: Theory Exp.* L10001 (2006).
- [15] P. Le Doussal, *Phys. Rev. Lett.* **96**, 235702 (2006).
- [16] T. Rizzo and H. Yoshino, *Phys. Rev. B* **73**, 064416 (2006).
- [17] H. G. Katzgraber and F. Krzakala, *Phys. Rev. Lett.* **98**, 017201 (2007).
- [18] H. Yoshino and T. Rizzo, *Phys. Rev. B* **77**, 104429 (2008).

- 
- [19] J. H. Pixley and A. P. Young, Phys Rev B **78**, 014419 (2008).
- [20] T. Aspelmeier, Phys. Rev. Lett. **100**, 117205 (2008).
- [21] T. Aspelmeier, J. Phys. A **41**, 205005 (2008).
- [22] T. Mora and L. Zdeborova, J. Stat. Phys. **131**, 1121 (2008).
- [23] N. Aral and A. N. Berker, Phys. Rev. B **79**, 014434 (2009).
- [24] Q. H. Chen, Phys. Rev. B **80**, 144420 (2009).
- [25] T. Jörg and F. Krzakala, J. Stat. Mech.: Theory Exp. L01001 (2012).
- [26] P. Collet and J.-P. Eckmann, *Iterated Maps on the Interval as Dynamical Systems* (Birkhäuser, Boston, 1980).
- [27] R. C. Hilborn, *Chaos and Nonlinear Dynamics*, 2nd ed. (Oxford University Press, New York, 2003).
- [28] A. A. Migdal, Zh. Eksp. Teor. Fiz. **69**, 1457 (1975) [Sov. Phys. JETP **42**, 743 (1976)].
- [29] L. P. Kadanoff, Ann. Phys. (N.Y.) **100**, 359 (1976).
- [30] A. N. Berker and S. Ostlund, J. Phys. C **12**, 4961 (1979).
- [31] R. B. Griffiths and M. Kaufman, Phys. Rev. B **26**, 5022R (1982).
- [32] M. Kaufman and R. B. Griffiths, Phys. Rev. B **30**, 244 (1984).
- [33] S. R. McKay and A. N. Berker, Phys. Rev. B **29**, 1315 (1984).
- [34] M. Hinczewski and A. N. Berker, Phys. Rev. E **73**, 066126 (2006).
- [35] D. Andelman and A. N. Berker, Phys. Rev. B **29**, 2630 (1984).
- [36] G. Migliorini and A. N. Berker, Phys. Rev. B. **57**, 426 (1998).
- [37] M. Hinczewski and A.N. Berker, Phys. Rev. B **72**, 144402 (2005).
- [38] C. Güven, A. N. Berker, M. Hinczewski, and H. Nishimori, Phys. Rev. E **77**, 061110 (2008).
- [39] G. Gülpınar and A. N. Berker, Phys. Rev. E **79**, 021110 (2009).
- [40] S. B. Roy and M. K. Chattopadhyay, Phys. Rev. B **79**, 052407 (2009).

- 
- [41] J. O. Indekeu and A. N. Berker, *Physica A (Utrecht)* **140**, 368 (1986).
  - [42] R. R. Netz and A. N. Berker, *Phys. Rev. Lett.* **68**, 333 (1992).
  - [43] M. G. Mazza and M. Schoen, *Int. J. Mol. Sci.* **12**, 5352 (2011).
  - [44] G. Grinstein, A. N. Berker, J. Chalupa, and M. Wortis, *Phys. Rev. Lett.* **36**, 1508 (1976).

Chapter 4

**ODD Q-STATE CLOCK SPIN GLASSES**



## 4.1 Introduction

Spin-glass problems [1] continue to fascinate with new orderings and phase diagrams under frustration [2] and ground-state entropy [3, 4]. The extension of these models from the extensively studied Ising spin models to less simple spins offer the possibility of completely new orderings and phase diagrams. We find that odd  $q$ -state clock models are such cases. Spins in odd  $q$ -state clock models cannot be exactly anti-aligned with each other. Furthermore, for a given spin, its interacting neighbor has two states that give the maximally misaligned pair configuration. This fact immediately injects ground-state entropy in the presence of antiferromagnetic interactions, even without the frozen randomness of interactions of the spin-glass system.

We have calculated, from renormalization-group theory, the phase diagrams of arbitrary odd  $q$ -state clock spin-glass models in  $d = 3$  dimensions. We find that these models have asymmetric phase diagrams, as is also the case for quantum Heisenberg spin-glass models [5]. They exhibit no finite-temperature spin-glass phase. For all odd  $q \geq 5$ , algebraically ordered antiferromagnetic phases occur. One such phase is dominant and occurs for all  $q \geq 5$ . Other such phases occupy a small low-temperature portion of the phase diagram and occur for  $5 \leq q \leq 15$ . All algebraically ordered phases have the same structure, determined by an attractive finite-temperature sink fixed point where a dominant and a subdominant pair states have the only non-zero Boltzmann weights. The phase transition critical exponents come from distinct critical fixed points, but quickly saturate to the high  $q$  value. Thus, a rich phase transition structure is seen for odd  $q$ -state spin-glass models on a  $d = 3$  hierarchical lattice.

## 4.2 The odd $q$ -state clock spin-glass model and the renormalization-group method

The  $q$ -state clock models are composed of unit spins that are confined to a plane and that can only point along  $q$  angularly equidistant directions. Accordingly, the

$q$ -state clock spin-glass model is defined by the Hamiltonian

$$-\beta\mathcal{H} = \sum_{\langle ij \rangle} J_{ij} \vec{s}_i \cdot \vec{s}_j = \sum_{\langle ij \rangle} J_{ij} \cos(\theta_i - \theta_j), \quad (4.1)$$

where  $\beta = 1/k_B T$ , at site  $i$  the spin angle  $\theta_i$  takes on the values  $(2\pi/q)\sigma_i$  with  $\sigma_i = 0, 1, 2, \dots, q-1$ , and  $\langle ij \rangle$  denotes that the sum runs over all nearest-neighbor pairs of sites. The bond strengths  $J_{ij}$  are  $+J > 0$  (ferromagnetic) with probability  $1-p$  and  $-J$  (antiferromagnetic) with probability  $p$ . This model becomes the Ising model for  $q=2$  and the XY model for  $q \rightarrow \infty$ .

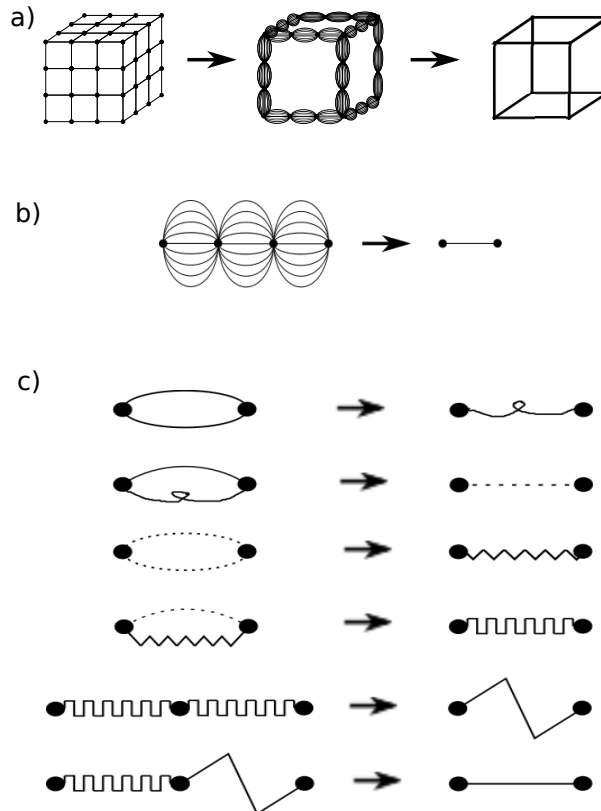


Figure 4.1: (a) Migdal-Kadanoff approximate renormalization-group transformation for the  $d = 3$  cubic lattice with the length-rescaling factor of  $b = 3$ . Bond-moving is followed by decimation. (b) Exact renormalization-group transformation for the equivalent  $d = 3$  hierarchical lattice with the length-rescaling factor of  $b = 3$ . (c) Pairwise applications of the quenched probability convolution of Eq.(4.5), leading to the exact transformation in (b).

The  $q$ -state clock spin-glass model, in  $d = 3$  dimensions, is readily solved by a renormalization-group method that is approximate on the cubic lattice [6, 7]

and simultaneously exact on the hierarchical lattice [8, 9, 10, 11, 12]. Hierarchical lattices have been used to study a variety of spin-glass and other statistical mechanics problems.[15, 14, 13, 16, 17, 18, 19, 20, 21, 22, 23, 24, 25, 26, 27, 28, 29, 30, 31, 32, 33, 34, 35, 36, 37, 39, 38, 40, 41, 42] Under rescaling, for  $q > 4$ , the form of the interaction as given in the rightmost side of Eq.(4.1) is not conserved and one must therefore express the Hamiltonian more generally, as

$$-\beta\mathcal{H} = \sum_{\langle ij \rangle} V(\theta_i - \theta_j). \quad (4.2)$$

The energy  $V(\theta_i - \theta_j)$  depends on the absolute value of the angle difference,  $|(\theta_i - \theta_j)|$ . Thus, the renormalization-group flows are the flows of  $q/2$  interaction constants for even  $q$  and the flows of  $(q - 1)/2$  interaction constants for odd  $q$ . With no loss of generality, the maximum value of  $V(\theta_i - \theta_j)$  is set to zero.

The renormalization-group transformation, for spatial dimensions  $d = 3$  and length rescaling factor  $b = 3$  (necessary for treating the ferromagnetic and anti-ferromagnetic correlations on equal footing), is achieved by a sequence of bond moving

$$V_{bm}(\theta_1 - \theta_2) + G_{12} = \sum_{n=1}^{b^{d-1}} V_n(\theta_1 - \theta_2) \quad (4.3)$$

and decimation

$$e^{V_{dec}(\theta_1 - \theta_4) + G_{14}} = \sum_{\theta_2, \theta_3} e^{V_1(\theta_1 - \theta_2) + V_2(\theta_2 - \theta_3) + V_3(\theta_3 - \theta_4)}, \quad (4.4)$$

where the constants  $G_{ij}$  are fixed by the requirement that the maximum value of  $V(\theta_i - \theta_j)$  is zero.

The starting bimodal quenched probability distribution of the interactions, characterized by  $p$  and described above, is also not conserved under rescaling. The renormalized quenched probability distribution of the interactions is obtained

by the convolution [43]

$$P'(V'(\theta_{i'j'})) = \int \left[ \prod_{ij}^{i'j'} dV(\theta_{ij}) P(V(\theta_{ij})) \right] \delta(V'(\theta_{i'j'}) - R(\{V(\theta_{ij})\})), \quad (4.5)$$

where  $R(\{V(\theta_{ij})\})$  represents the bond moving and decimation given in Eqs.(4.3) and (4.4). For numerical practicality, the bond moving and decimation of Eqs.(4.3) and (4.4) are achieved by a sequence of pairwise combination of interactions, as shown in Fig. 4.1(c), each pairwise combination leading to an intermediate probability distribution resulting from a pairwise convolution as in Eq.(4.5). We effect this procedure numerically, by generating 5,000 interactions that embody the quenched probability distribution resulting from each pairwise combination. Due to the large number of phase diagrams (Figs. 4.2 and 4.3), a single realization of quenched randomness is used. Each of the generated 5,000 interactions is determined by  $(q - 1)/2$  interaction constants. At each pairwise convolution as in Eq.(4.5), 5,000 randomly chosen pairs are matched by Eq.(4.3) or (4.4), and a new set of 5,000 is produced.

The different thermodynamic phases of the model are identified by the different asymptotic renormalization-group flows of the quenched probability distributions. For all renormalization-group flows, inside the phases and on the phase boundaries, Eq.(4.5) is iterated until asymptotic behavior is reached. Thus, we are able to calculate phase diagrams for any number of clock states  $q$ . Similar previous studies, on other spin-glass systems, are in Refs. [13, 14, 15, 16, 17, 18, 19, 20, 21, 22].

In a previous study [21], using the above method, we have considered even values of  $q$ . In this study, we consider odd values of  $q$  and calculate the phase diagrams, which are not symmetric around  $p = 0.5$ . For  $q$  odd, the system does not have sublattice spin-reversal ( $\theta_i \rightarrow \theta_i + \pi$ ) symmetry, which leads to the asymmetric phase diagrams. We obtain qualitatively new features in the phase diagrams for odd  $q$ . These features do not occur for even  $q$ .

### 4.3 Calculated phase diagrams for odd $q$ -state clock spin glasses in $d=3$

Our calculated phase diagrams for the odd  $q = 3, 5, 7, 9, 11, 13, 15, 17, 21, 361$ -state clock spin-glass models are shown in Fig. 4.2. The lower temperature details of the phase diagrams are given in Fig. 4.3. All phase boundaries are second order.

The phase diagrams of the odd  $q$ -state clock spin-glass models are quite different from the even  $q$  phase diagrams [21]: The odd  $q$  phase diagrams do not have ferromagnetic-antiferromagnetic symmetry, *i.e.*, they are not left-right symmetric with respect to the  $p = 0.5$  line. The odd  $q$  phase diagrams do not have a spin-glass phase, which is consistent with previous results [13, 21] that the XY model, corresponding to the  $q \rightarrow \infty$  limit of the  $q$ -state clock models, does not have a spin-glass phase on  $d = 3$  hierarchical lattices. The odd  $q$  phase diagrams show a multiplicity of algebraically ordered phases (and one conventionally ordered phase) on the antiferromagnetic side. All points in an algebraically ordered phase flow, under renormalization group, to a single stable fixed point (sink) that occurs at non-zero, non-infinite temperature. Convergence to this stable critical fixed occurs, to 6 significant figures, within 5 renormalization-group transformations. Further convergence is obtained for more renormalization-group transformations. As seen in Fig. 4.4, at each renormalization-group transformation, the quenched probability distribution of interactions changes from the initial  $(1-p)$  and  $p$  double-delta function, to eventually reach the critical sink described below. Because of this flow structure, the correlation length is infinite and the correlation function decays as an inverse power of distance (as opposed to exponentially) at all points in such an algebraically ordered phase. Such algebraically ordered phases were previously seen by Berker and Kadanoff [3, 4] for antiferromagnetic Potts models and have since been extensively studied [44, 45, 46, 47, 48, 49, 50, 51, 52]. The correlation function decay critical exponent has the same value for all points in such a phase, since the renormalization-group flows are to single fixed point, in contrast to the continuously varying critical exponents in the algebraically ordered phase of the  $d = 2$  XY model, where the flows are to a fixed line.[53, 54, 55]

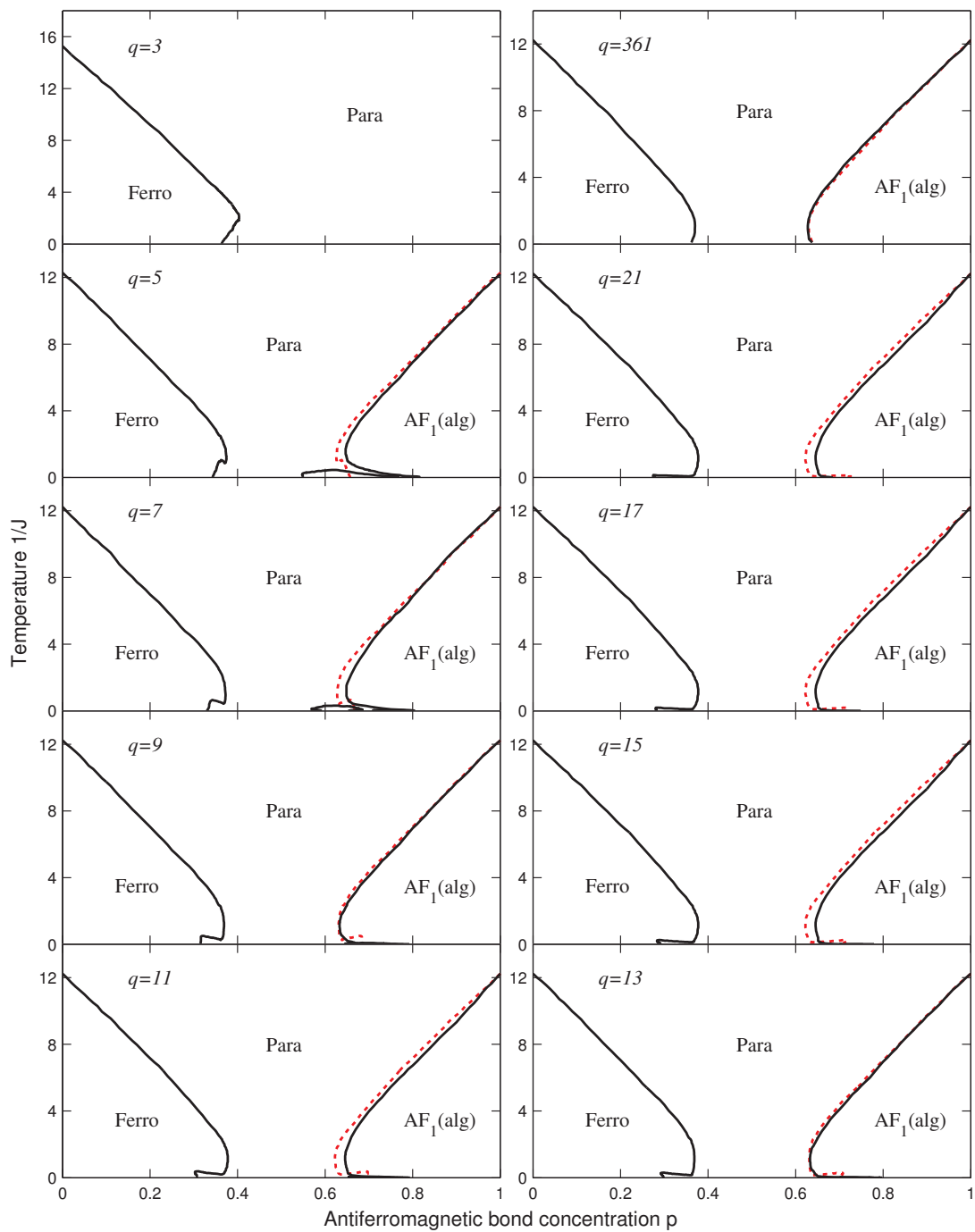


Figure 4.2: (Caption next page.)

Figure 4.2: (Previous page) Calculated phase diagrams (color online) of the odd  $q$ -state clock spin-glass models on the hierarchical lattice with  $d = 3$  dimensions. These phase diagrams do not have ferromagnetic-antiferromagnetic symmetry, *i.e.*, they are not left-right symmetric with respect to the  $p = 0.5$  line. The phase diagrams do not have a spin-glass phase, but show a multiplicity of algebraically ordered phases on the antiferromagnetic side. The phase diagrams show true reentrance (disordered-ordered-disordered) as temperature is lowered at fixed antiferromagnetic bond concentration  $p$ , on both the ferromagnetic and antiferromagnetic sides of the phase diagram. The phase diagrams also show lateral, true double reentrance (ferromagnetic-disordered-ferromagnetic-disordered) as the antiferromagnetic bond concentration  $p$  is increased at fixed temperature, only on the ferromagnetic side. No antiferromagnetic ordering occurs for the lowest model,  $q = 3$ . Algebraically ordered antiferromagnetic phases occur for all higher  $q \geq 5$  models. In these cases, the phase boundary between the dominant antiferromagnetic algebraically ordered phase and the disordered phase is slightly asymmetric with the phase boundary between the ferromagnetic and disordered phases. To make this slight asymmetry evident, the latter boundary is also shown (dashed) reflected about the  $p = 0.5$  line. The lower temperature details of these phase diagrams are shown in Fig. 4.3

The phase diagrams show true reentrance [13] (disordered-ordered-disordered) as temperature is lowered at fixed antiferromagnetic bond concentration  $p$ , on both the ferromagnetic and antiferromagnetic sides of the phase diagram. The phase diagrams also show lateral, true double reentrance (ferromagnetic-disordered-ferromagnetic-disordered) as the antiferromagnetic bond concentration  $p$  is increased at fixed temperature, only on the ferromagnetic side. Multiple reentrances have previously been seen in liquid crystal systems.[56, 57, 58]

No antiferromagnetic ordering occurs for the lowest model,  $q = 3$ . Algebraically ordered antiferromagnetic phases occur for all higher  $q \geq 5$  models. In these cases, the phase boundary between the dominant antiferromagnetic algebraically ordered phase and the disordered phase is slightly asymmetric with the phase boundary between the ferromagnetic phase and the disordered phase. To make this slight asymmetry evident, the latter boundary is also shown (dashed) in Fig. 4.2 reflected about the  $p = 0.5$  line. The phase diagram for the XY model limit, namely odd  $q \rightarrow \infty$ , is also shown in Fig. 4.2, calculated here with  $q = 361$  clock states. In this limit, the distinction between odd and even  $q$  disappears. This suggests that the zero-temperature spin-glass phase [60] found for even  $q \rightarrow \infty$  [21] also occurs

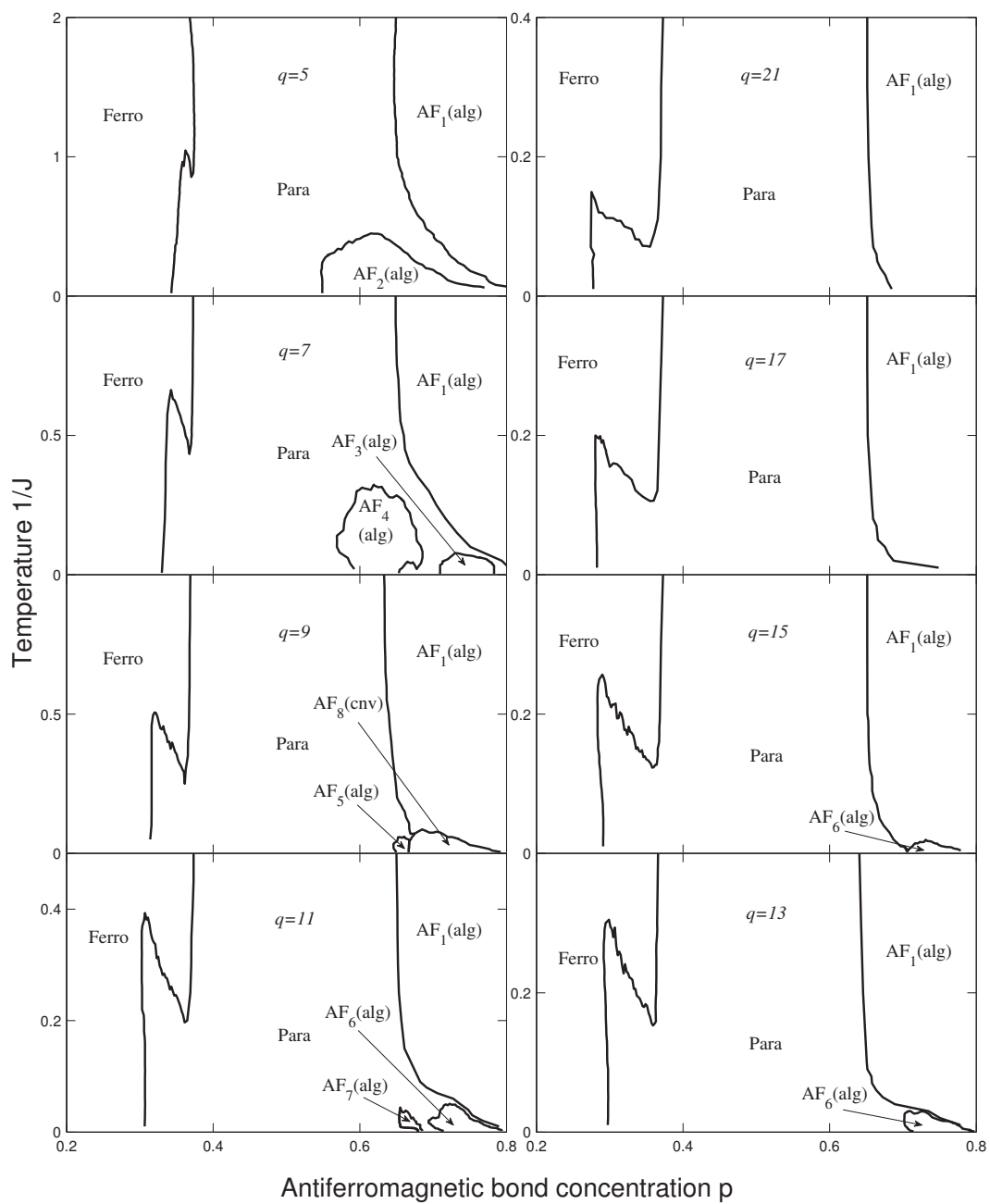


Figure 4.3: Lower temperature details of the phase diagrams shown in Fig. 4.2.



for odd  $q \rightarrow \infty$ .

#### 4.4 Algebraically ordered phases, finite-temperature renormalization-group sinks, and ground-state entropy

Spins in odd  $q$ -state clock models cannot be exactly anti-aligned with each other, *i.e.*,  $\theta_i - \theta_j = 2\pi q_{ij}/q < \pi$ , where  $q_{ij}$  is an integer between 0 and  $(q-1)/2$  inclusive. Furthermore, for a given spin, its interacting neighbor has two states that give the maximally misaligned pair configuration with  $\theta_i - \theta_j = \pi(q-1)/q < \pi$ . Thus, for antiferromagnetic interaction, this local degeneracy is of crucial distinctive importance, injecting ground-state entropy into the system, driving the sink of a would-be ordered phase to non-zero temperature, and thereby causing algebraic order, as generally explained in Ref. [3, 4].

All points in the antiferromagnetic phases in the phase diagrams in Figs. 4.2 and 4.3 flow under renormalization-group to  $p = 1$  (just as all points in the one ferromagnetic phase flow to  $p = 0$ ). The most extant antiferromagnetic phase in Fig. 4.2, labeled  $AF_1(alg)$ , occurring for all odd  $q \geq 5$  values, is an algebraically ordered phase. All points in this phase flow to a completely stable fixed point ("a phase sink" [61]) that is also a critical point since it occurs at finite temperature [3, 4]. Of the pair-interaction Boltzmann weights  $e^{V(\theta_i - \theta_j)}$ , with  $\theta_i - \theta_j = \pi(q - 1 - 2n)/q$ , where  $n = 0$  is the most misaligned pair state,  $n = 1$  is the next-most misaligned state, *etc.*, until  $n = (q - 1)/2$  is the completely aligned pair state, only two are non-zero at this sink: The most misaligned pair state,  $n = 0$ , is dominant with  $e^{V(\pi(q-1)/q)} = 1$  and the next-most misaligned pair state,  $n = 1$ , is also present but less dominant with  $e^{V(\pi(q-3)/q)} = 1/3$ . The other, less misaligned pair states, with  $n \geq 2$ , and the aligned pair state have zero Boltzmann weight at this sink. That these sink fixed-point Boltzmann weights are applicable for all odd  $q$  is consistent with the fact that the  $q - 5$  less-misaligned pair states and one aligned pair state have negligible Boltzmann weights at the sink fixed point, so that the numerosity of  $q$  does not matter. The finite difference between the energies

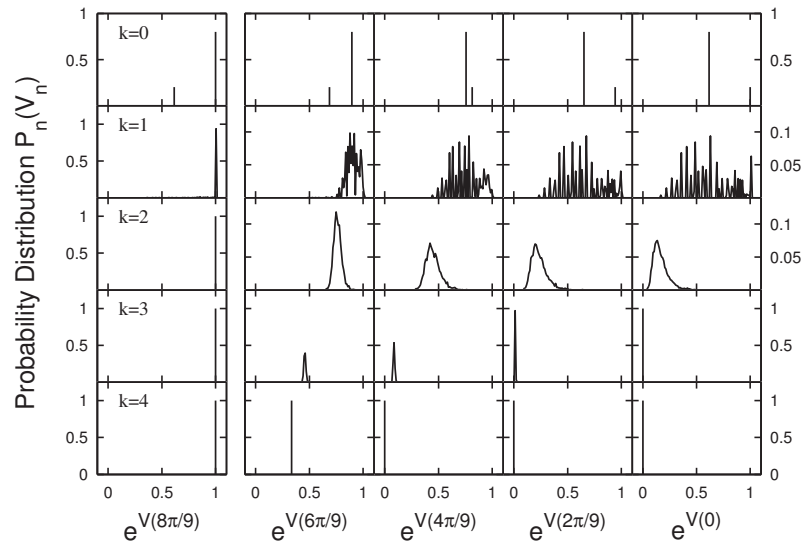


Figure 4.4: Evolution of the quenched probability distribution under successive renormalization-group transformations. The case of  $q = 9$ , starting with the initial condition temperature  $1/J = 4$  and antiferromagnetic bond concentration  $p = 0.8$  is shown here. For  $q = 9$ , the generalized interaction potential unavoidably generated by the renormalization-group transformation is determined by 5 interaction constants (see Table 4.1). The renormalization-group transformation gives the evolution, under scale change, of the correlated quenched probability distribution  $P(V_0, V_1, V_2, V_3, V_4)$ . Shown in this figure are the projections  $P_0(V_0) = \int dV_1 dV_2 dV_3 dV_4 P(V_0, V_1, V_2, V_3, V_4)$  and similarly for  $P_1(V_1)$ ,  $P_2(V_2)$ ,  $P_3(V_3)$ , and  $P_4(V_4)$ . Each row corresponds to another renormalization-group step  $k$ , as marked on the figure. It is seen here that in four renormalization-group transformations, the renormalized system essentially reaches the critical phase sink described in Sec. IV: The most misaligned pair state is dominant with Boltzmann weight  $e^{V(8\pi/9)} = 1$  and the next-most misaligned pair state is also present but less dominant with  $e^{V(6\pi/9)} = 1/3$ . The other two less misaligned pair states and the aligned pair state have zero Boltzmann weight at the sink.

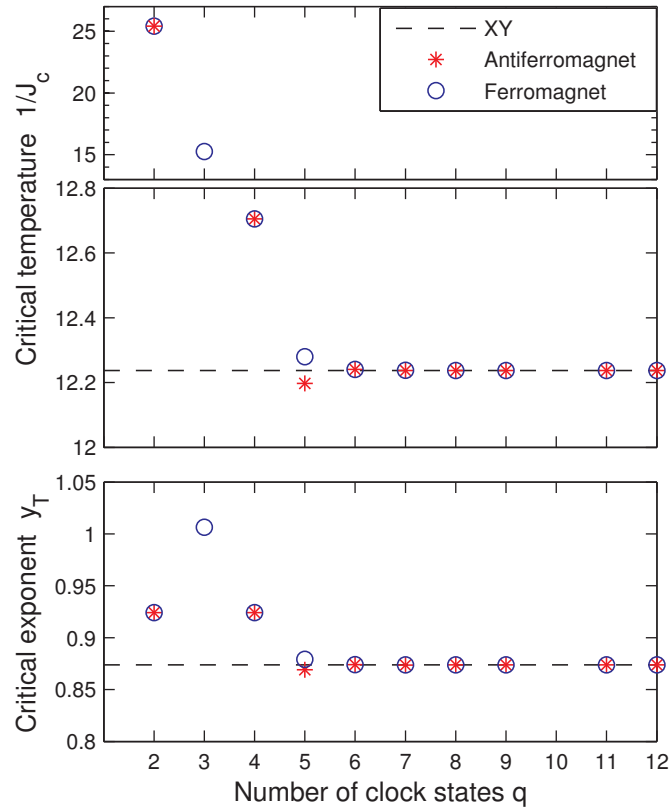


Figure 4.5: (Color online) Top panel: Critical temperatures  $1/J_C$  of the ferromagnetic (circles) and antiferromagnetic (asterisks)  $q$ -state clock models in  $d = 3$ . Lower panel: Critical exponents  $y_T$  of the ferromagnetic (circles) and antiferromagnetic (asterisks)  $q$ -state clock models in  $d = 3$ . In both panels, the values exactly coincide for even  $q$ , due to the ferromagnetic-antiferromagnetic symmetry that is present for even  $q$  but absent for odd  $q$ .

for  $\theta_i - \theta_j = \pi(q-1)/q$  and  $\theta_i - \theta_j = \pi(q-3)/q$  establishes this sink as a finite-temperature attractive critical fixed point. It can be shown that, in the basin of attraction of a finite-temperature fixed point, the order parameter is strictly zero, the correlation length is infinite, and the correlations vanish algebraically with distance.[3, 4, 62, 11]

The evolution of the quenched probability distribution, under successive renormalization-group transformations, towards such a critical sink is shown in Fig. 4.4. The case of  $q = 9$ , starting with the initial condition temperature  $1/J = 4$  and antiferromagnetic bond concentration  $p = 0.8$  is shown in the figure. For  $q = 9$ , the generalized interaction potential unavoidably generated by the renormalization-group transformation is determined by 5 interaction constants (see Table 4.1). The renormalization-group transformation gives the evolution, under scale change, of the correlated quenched probability distribution  $P(V_0, V_1, V_2, V_3, V_4)$ . Shown in Fig. 4.4 are the projections  $P_0(V_0) = \int dV_1 dV_2 dV_3 dV_4 P(V_0, V_1, V_2, V_3, V_4)$  and similarly for  $P_1(V_1), P_2(V_2), P_3(V_3)$ , and  $P_4(V_4)$ . Each row corresponds to another renormalization-group step  $k$ , as marked on the figure. It is seen that in four renormalization-group transformations, the renormalized system essentially reaches the critical phase sink described above: The most misaligned pair state is dominant with Boltzmann weight  $e^{V(8\pi/9)} = 1$  and the next-most misaligned pair state is also present but less dominant with  $e^{V(6\pi/9)} = 1/3$ . The other two less misaligned pair states and the aligned pair state have zero Boltzmann weight at the sink.

The less extant antiferromagnetic phases occur for specific  $q$  values, at lower temperatures, and are disconnected from the most extant antiferromagnetic phase  $AF_1(alg)$ . In  $AF_2(alg)$ , the two sink Boltzmann weights have exchanged roles: the next-most misaligned pair state,  $n = 1$ , is dominant with  $e^{V(\pi(q-3)/q)} = 1$  and the most misaligned pair state,  $n = 0$ , is also present but less dominant with  $e^{V(\pi(q-1)/q)} = 1/3$ . In  $AF_3(alg), AF_4(alg), AF_5(alg), AF_6(alg), AF_7(alg)$ , these roles are played respectively by  $n = 2, 0, n = 1, 2, n = 2, 1, n = 1, 4, n = 4, 2$ . On the other hand,  $AF_8(cnv)$  is a conventionally ordered phase, with a strong-coupling sink fixed point where  $n = 1$  and  $n = 4$  are equally dominant.

It is thus seen that the stable sink fixed points that attract, under renormaliza-

$V(\theta_{ij})$	n=0	n=1	n=2	n=3	n=4	n=5	n=6	$y_T$	relevant eigenvectors
q=5	0	-0.0905	-0.1502					0.869030	( 1, 0.588 )
q=7	0	-0.0538	-0.1242	-0.1569				0.873691	( 1, 0.782, 0.330 )
q=9	0	-0.0345	-0.0893	-0.1395	-0.1599			0.873709	( 1, 0.866, 0.544, 0.206 )
q=11	0	-0.0238	-0.0649	-0.1111	-0.1475	-0.1614		0.873709	( 1, 0.909, 0.675, 0.387, 0.140 )
q=13	0	-0.0173	-0.0486	-0.0873	-0.1249	-0.1523	-0.1623	0.873709	( 1, 0.935, 0.759, 0.523, 0.287, 0.101 )

Table 4.1: Antiferromagnetic critical fixed-point potentials  $V(\pi(q-1-2n)/q)$ , critical exponents  $y_T$ , and corresponding relevant eigenvectors of different odd  $q$ -state clock models. Thus, each column progresses, from left to right, from the most misaligned pair state  $n=0$  to the aligned pair state  $n=(q-1)/2$ . For each  $q$ , the relevant eigenvector is the (only) relevant eigenvector of the  $[(q-1)/2] \times [(q-1)/2]$  recursion matrix between the independent  $V(\theta_{ij})$ . Although the fixed points and relevant eigenvectors are distinct for different  $q$ , the critical exponents quickly converge  $y_T = 0.8737$ .

tion-group flows, and characterize the algebraically ordered phases have identical structure for all odd  $q \geq 5$ . A similar, but not identical, phenomenon occurs for the unstable critical fixed points that control the antiferromagnetic phase transitions. This is seen in Fig. 4.5 and Table 4.1, where the ferromagnetic ( $p=0$ ) and antiferromagnetic ( $p=1$ ) critical temperatures  $1/J_C$  are given as a function of  $q$ . The fixed-point Boltzmann weight values  $e^{V(\pi(q-1-2n)/q)}$  underpinning the antiferromagnetic phase transitions, as well as the critical exponents  $y_T$  and corresponding relevant eigenvectors are given for different  $q$  in Table 4.1. For each  $q$ , the relevant eigenvector is the (only) relevant eigenvector of the  $[(q-1)/2] \times [(q-1)/2]$  recursion matrix between the independent  $V(\theta_{ij})$ . Although the fixed points and relevant eigenvectors are distinct for different  $q$ , the critical temperatures and critical exponents quickly converge, for high  $q$ , to  $1/J_C = 12.2373$  and  $y_T = 0.8737$ . The critical temperatures and exponents thus show differences for low  $q$ . The convergence for high  $q$  of the critical temperatures at  $p=0$  and  $p=1$  is expected, since the  $q$ -state clock models approach the XY model for large  $q$ , with identical antiferromagnetic and ferromagnetic behavior.

## 4.5 Conclusion

We have calculated, from renormalization-group theory, the phase diagrams of arbitrary odd  $q$ -state clock spin-glass models in  $d=3$ . These models have asymmetric phase diagrams, as is also the case for quantum Heisenberg spin-glass models

[5]. For all odd  $q \geq 5$ , algebraically ordered antiferromagnetic phases occur. One such phase is dominant and occurs for all  $q \geq 5$ . Other such phases occupy small low-temperature portions of the phase diagrams and occur for  $5 \leq q \leq 15$ . All algebraically ordered phases have the same structure, determined by an attractive finite-temperature sink fixed point where a dominant and a subdominant pair states are the non-zero Boltzmann weights. The phase transition critical exponents, on the other hand, vary with  $q$  only at low  $q$ .

A rich and distinctive phase transition structure is thus seen for odd  $q$ -state spin-glass models on a  $d = 3$  dimensional hierarchical lattice.

## REFERENCES

- [1] H. Nishimori, *Statistical Physics of Spin Glasses and Information Processing* (Oxford University Press, 2001).
- [2] G. Toulouse, *Commun. Phys.* **2**, 115 (1977).
- [3] A. N. Berker and L. P. Kadanoff, *J. Phys. A* **13**, L259 (1980).
- [4] A. N. Berker and L. P. Kadanoff, *J. Phys. A* **13**, 3786 (1980).
- [5] C. N. Kaplan and A. N. Berker, *Phys. Rev. Lett.* **100**, 027204 (2008). See also P. C. Menezes and A. Theumann, *Phys. Rev. B* **78**, 054444 (2008).
- [6] A. A. Migdal, *Zh. Eksp. Teor. Fiz.* **69**, 1457 (1975) [*Sov. Phys. JETP* **42**, 743 (1976)].
- [7] L. P. Kadanoff, *Ann. Phys. (N.Y.)* **100**, 359 (1976).
- [8] A. N. Berker and S. Ostlund, *J. Phys. C* **12**, 4961 (1979).
- [9] R. B. Griffiths and M. Kaufman, *Phys. Rev. B* **26**, 5022R (1982).
- [10] M. Kaufman and R. B. Griffiths, *Phys. Rev. B* **30**, 244 (1984).
- [11] S. R. McKay and A. N. Berker, *Phys. Rev. B* **29**, 1315 (1984).
- [12] M. Hinczewski and A. N. Berker, *Phys. Rev. E* **73**, 066126 (2006).
- [13] M. J. P. Gingras and E. S. Sørensen, *Phys. Rev. B.* **46**, 3441 (1992).
- [14] G. Migliorini and A. N. Berker, *Phys. Rev. B.* **57**, 426 (1998).
- [15] M. J. P. Gingras and E. S. Sørensen, *Phys. Rev. B.* **57**, 10264 (1998).
- [16] M. Hinczewski and A.N. Berker, *Phys. Rev. B* **72**, 144402 (2005).
- [17] C. Güven, A. N. Berker, M. Hinczewski, and H. Nishimori, *Phys. Rev. E* **77**, 061110 (2008).
- [18] M. Ohzeki, H. Nishimori, and A. N. Berker, *Phys. Rev. E* **77**, 061116 (2008).
- [19] V. O. Özçelik and A. N. Berker, *Phys. Rev. E* **78**, 031104 (2008).

- 
- [20] G. Gülpınar and A. N. Berker, *Phys. Rev. E* **79**, 021110 (2009).
- [21] E. Ilker and A. N. Berker, *Phys. Rev. E* **87**, 032124 (2013).
- [22] E. Ilker and A. N. Berker, *Phys. Rev. E* **89**, 042139 (2014).
- [23] M. Kaufman and H. T. Diep, *Phys. Rev. E* **84**, 051106 (2011).
- [24] J. Barre, *J. Stat. Phys.* **146**, 359 (2012).
- [25] C. Monthus and T. Garel, *J. Stat. Mech. - Theory and Experiment*, P05002 (2012).
- [26] Z. Zhang, Y. Sheng, Z. Hu, et al., *Chaos* **22**, 043129 (2012).
- [27] S.-C. Chang and R. Shrock, *Phys. Lett. A* **377**, 671 (2013).
- [28] Y.-L. Xu, L.-S. Wang, and X.-M. Kong, *Phys. Rev. A* **87**, 012312 (2013).
- [29] R. F. S. Andrade and H. J. Herrmann, *Phys. Rev. E* **87**, 042113 (2013).
- [30] R. F. S. Andrade and H. J. Herrmann, *Phys. Rev. E* **88**, 042122 (2013).
- [31] C. Monthus and T. Garel, *J. Stat. Phys.-Theory and Experiment*, P06007 (2013).
- [32] O. Melchert and A. K. Hartmann, *Eur. Phys. J. B* **86**, 323 (2013).
- [33] J.-Y. Fortin, *J. Phys.-Condensed Matter* **25**, 296004 (2013).
- [34] Y. H. Wu, X. Li, Z. Z. Zhang, and Z. H. Rong, *Chaos Solitons Fractals* **56**, 91 (2013).
- [35] P. N. Timonin, *Low Temp. Phys.* **40**, 36 (2014).
- [36] B. Derrida and G. Giacomin, *J. Stat. Phys.* **154**, 286 (2014).
- [37] M. F. Thorpe and R. B. Stinchcombe, *Philos. Trans. Royal Soc. A - Math. Phys. Eng. Sciences* **372**, 20120038 (2014).
- [38] C. Monthus and T. Garel, *Phys. Rev. B* **89**, 184408 (2014).
- [39] T. Nogawa and T. Hasegawa, *Phys. Rev. E* **89**, 042803 (2014).
- [40] M. L. Lyra, F. A. B. F. de Moura, I. N. de Oliveira, and M. Serva, *Phys. Rev. E* **89**, 052133 (2014).
- [41] Y.-L. Xu, X. Zhang, Z.-Q. Liu, K. Xiang-Mu, and R. Ting-Qi, *Eur. Phys. J. B* **87**, 132 (2014).



- 
- [42] Y. Hirose, A. Oguchi, and Y. Fukumoto, *J. Phys. Soc. Japan* **83**, 074716 (2014).
- [43] D. Andelman and A. N. Berker, *Phys. Rev. B* **29**, 2630 (1984).
- [44] Y. Qin and Z. R. Yang, *Phys. Rev. B* **43**, 8576 (1991).
- [45] H. Saleur, *Nuclear Phys. B* **360**, 219 (1991).
- [46] J. A. Redinz, A. C. N. deMagalhaes, and E. M. F. Curado, *Phys. Rev. B* **49**, 6689 (1994).
- [47] J. A. Redinz and A. C. N. Demagalhaes, *Physica A* **246**, 27 (1997).
- [48] J. L. Jacobsen, J. Salas, and A. D. Sokal, *J. Stat. Phys.* **119**, 1153 (2005).
- [49] J. L. Jacobsen and H. Saleur, *Nuclear Phys. B* **743**, 207 (2006).
- [50] Y. Ikhlef, *Mod. Phys. Lett. B* **25**, 291 (2011).
- [51] J. L. Jacobsen and C. R. Scullard, *J. Phys. A* **45**, 494003 (2012).
- [52] J. L. Jacobsen and J. Salas, *Nuclear Phys. B* **875**, 678 (2013).
- [53] J. M. Kosterlitz and D. J. Thouless, *J. Phys. C* **6**, 1181 (1973).
- [54] J.V. José, L.P. Kadanoff, S. Kirkpatrick, and D.R. Nelson, *Phys. Rev. B* **16**, 1217 (1977).
- [55] A. N. Berker and D. R. Nelson, *Phys. Rev. B* **19**, 2488 (1979).
- [56] J. O. Indekeu and A. N. Berker, *Physica A* **140**, 368 (1986).
- [57] R. R. Netz and A. N. Berker, *Phys. Rev. Lett.* **68**, 333 (1992).
- [58] M. G. Mazza and M. Schoen, *Int. J. Mol. Sci.* **12**, 5352 (2011).
- [59] S. Chen, H.-B. Luo, H.-L. Xie, and H. L. Zhang, *J. Polymer Sci. A* **51**, 924 (2013).
- [60] G. Grinstein, A. N. Berker, J. Chalupa, and M. Wortis, *Phys. Rev. Lett.* **36**, 1508 (1976).
- [61] A. N. Berker and M. Wortis, *Phys. Rev. B* **14**, 4946 (1976).
- [62] M. E. Fisher and A. N. Berker, *Phys. Rev. B* **26**, 2507 (1982).

Chapter 5

**DIFFUSIVE DYNAMICS IN  
NON-EQUILIBRIUM SYSTEMS**

Dynamical systems with many degrees of freedom follow in general an observable diffusive motion imposed by vibrational modes due to thermal energy. The transitions between different configurational states continuously occur in non-equilibrium systems until relaxing to the global equilibrium state. Atomic scale events in such diffusive motions can be observed indirectly in experimental studies. On the other hand, computer simulations including interatomic interactions and partitioning thermal energy randomly on degrees of freedom maintain motional information on individuals. Hence, MD simulations are extensively used on the investigation of many body systems or specific molecules interacting with many body environment under the effect of thermodynamics. With a sincere interest on these studies, we work on two different problems. In the first study, we demonstrate a scheme projecting continuous dynamical modes on to a discrete Markov State Model (MSM) and analyze cw-ESR spectrum of a spin label attached to a macromolecule undergoing an arbitrary (but Markovian) rotational diffusion. In the second study, we generate the statistics and calculate the energetics of the dominant surface diffusion mechanisms and observe growth modes on bimetallic nanoparticles.

## 5.1 Simulating cw-ESR Spectrum Using Discrete Markov Model of Single Brownian Trajectory

Dynamic trajectories can be modeled with a Markov State Model (MSM). The reduction of continuous space coordinates to discretized coordinates can be done by statistical binning process. In addition to that, the transition probabilities can be determined by recording each event in the dynamic trajectory. This framework is put to a test by the electron spin resonance (ESR) spectroscopy of nitroxide spin label in X- and Q-bands. Calculated derivative spectra from the MSM model with transition matrix obtained from a single Brownian trajectory by a statistical binning process with the derivative spectra generated from the average of a large number of Brownian trajectories, are compared and yield a very good agreement. It is suggested that this method can be implemented to calculate absorption spectra from molecular dynamics (MD) simulation data.

### 5.1.1 Introduction

Spin labeling theory [1, 2, 3] has many applications in understanding the dynamics of complex molecules in a liquid environment. The line shapes from the continuous wave electron spin resonance (cw-ESR) spectroscopy due to rotational diffusive motion in liquid environment had already been investigated by stochastic Kubo-Anderson approach [4, 5, 6], approximation of relaxation times [7, 8], and spherical Stochastic Liouville Equation (SLE) [9] formalism.

The work by Robinson and co-workers [10] changed the perspective on looking to the problem by taking the rotational molecular trajectory as given. This has opened a new era, when the community started to infer possible interactions in the liquid environment that are effective on the cw-ESR spectrum by using molecular dynamics (MD) simulations following Steinhoff and Hubbell [11, 12]. This framework is based on calculating cw-ESR spectra of a spin label on a rotationally diffusing molecule from the motion of the three Euler angles  $(\phi, \theta, \psi)$  that represent the orientational dynamics, and can be modeled with isotropic and anisotropic rotational diffusion processes.

On the other hand, the diffusion of three Euler angles may depend on the internal dynamics and structural properties of the molecule and the spin label [13, 14, 15]. Thus, ESR spectroscopy is a very helpful method in understanding the physics of such complex structures [16, 17, 18, 19]. With the inclusion of the internal dynamics, this problem becomes more complex so that it requires an additional set of variables. As a result modeling spin dynamics with the sampling of different types of potentials [20, 21, 22] has become necessary. In the end, one can combine internal dynamics obtained from MD data and the global diffusion of the molecule to account for the entire dynamics of a spin-labeled molecule [23].

In the recent years, Markov State Models (MSM) of conformational dynamics have been suggested, in order to interpret the slowly varying potential changes applied on the molecule or the spin label itself due to the effects of internal degrees of freedom [24, 25]. This framework has been established on determining transition probabilities from relaxation timescales of each dynamical mode. MSM technique shows a promising scheme in understanding the features of intra- and inter-molecular phenomena [26, 27] in non-equilibrium dynamics.

Another difficulty for the determination of the effects resulting from spatial dynamics of a molecule from a MD trajectory, is that MD trajectories are often too short and would require to complete the rest of trajectory artificially, e.g., adding the paths together back and forth. To overcome this issue, Oganessian suggested a novel technique to get an overall scheme for simulation from a truncated trajectory [28, 29, 30]. Another approach suggests calculating ESR spectra by using spherical SLE formalism and taking rotational diffusion parameters from the MD simulations [31] which has basic similarities with the framework that we used in this study.

In this paper, we take the example of the cw-ESR spectrum of a spin-1/2 electron coupled to a magnetic field and spin-1 nucleus, e.g., nitroxide spin label, freely diffusing in a liquid, which is a problem that has been discussed many times. The s-state Kubo-Anderson process, with Markovian jumps maintains a solution that takes relatively less computational effort than working on the continuous coordinate system. We show that a Brownian trajectory can be mapped to a MSM by using a statistically binning process of exhibited jumps from one microstate to

another. Therefore, a comparison between, on the one hand, calculated derivative spectra from MSM model with transition matrix obtained from a single Brownian trajectory by statistical binning process and, on the other hand the derivative spectra generated from the average of large number of Brownian trajectories has been made and shows a very good agreement. In addition to that, extension to other coordinates, i.e., other rotation angles and hidden dynamics is noted. It is believed that this framework would fit into calculating the derivative spectra MD simulation trajectories. This methodology can be also successful for separable and reducible potentials. It also allows a faster parametrization process with less computational time by reducing the set of variables.

This section is organized as follows: The Kubo-Anderson process with s-state Markov model, generalization to s-state Kubo-Anderson process with discrete rotational diffusion, and continuous isotropic diffusion processes are overviewed in Sections 5.1.2, 5.1.3, and 5.1.4 respectively. In Section 5.1.5, a reduction scheme from continuous coordinates to discrete coordinates by using statistical binning process is introduced, and put to a test for the nitroxide example. In Section 5.1.6, we note an extension scheme to other coordinates and also exhibit the relevant comparisons. The application on short length trajectories is shown in Section 5.1.7. Finally, we discuss modeling different diffusion processes in Markov dynamics. In addition to that, we have included calculation tools for trajectory, evolution of average magnetization in trajectory method, and computational details in Appendix (Section 5.1.9).

### 5.1.2 Markov State Model for diffusion

For a Markov process, the master equation for microstate probability vector  $\langle p(t) |$  is given as

$$\frac{d \langle p(t) |}{dt} = \langle p(t) | \mathbf{K}, \quad (5.1)$$

where  $\mathbf{K}$  is the transition rate matrix per unit time whose elements  $\mathbf{K}_{ij}$  represent the transition rate from microstate  $\langle i |$  to  $\langle j |$ , so that it is basically the

diffusion operator. The time-dependent average magnetization is a function of these microstates, and it can be written as  $M_+(t) = \langle M_+(t)|p(t)\rangle$ , or equivalently  $M_+(t) = \langle p(t)M_+(t)|1\rangle$ . Thus, the time evolution of probability-weighted magnetization vector is given as a Kubo-Anderson process[4, 5, 6],

$$\frac{d\langle p(t)M_+(t)|}{dt} = \langle p(t)M_+(t)|(-i\mathbf{\Omega} + \mathbf{K}), \quad (5.2)$$

where  $\mathbf{\Omega}$  is a diagonal matrix with the eigenfrequencies of the Hamiltonian. Here,  $\mathbf{\Omega}$  is independent of time if the microstates are stationary. The decay rate of the average magnetization is given by the transition rate matrix. The cw-ESR signal is obtained from the Fourier transform of the time-dependent average magnetization. Taking the Fourier transform of both sides and multiplying by ket  $|1\rangle_s = [1, 1, 1, \dots, 1]^T$ , which is a vector with length  $s$  (number of states), and applying the initial condition  $M_+(0) = 0$  for all microstates yields to the equation

$$I(\omega) = \langle v_{eq.}|(i\mathbf{\Omega} - \mathbf{K} + i\omega\mathbf{I}_s)^{-1}|1\rangle_s. \quad (5.3)$$

where  $\langle v_{eq.}|$  represents the equilibrium probability vector and  $\mathbf{I}_s$  is the  $s \times s$  identity matrix. This is the Stochastic Liouville Equation (SLE) formalism for ESR absorption lines in which the Liouvillian operator is taken as the eigenfrequency matrix  $\mathbf{\Omega}$ . The normalization factors are ignored for practicality since we normalize the spectrum by the maximum intensity value. The spin-spin relaxation rate can be included as an operator in the parenthesis. Taking the derivative with respect to frequency  $\omega$  will give the derivative absorption spectra,

$$\frac{\partial I(\omega)}{\partial \omega} = -i \langle v_{eq.}|(i\mathbf{\Omega} - \mathbf{K} + (i\omega + \gamma_e T_2^L)\mathbf{I}_s)^{-2}|1\rangle_s, \quad (5.4)$$

where  $T_2^L = 1/\gamma_e T_2$ , with  $T_2$  as spin-spin relaxation time. Note that we should divide each term in the parenthesis by gyromagnetic ratio  $\gamma_e$  in order to see the spectrum in Gauss (G) units. This formalism can be extended to  $s$ -site jump model, i.e., the  $s$ -state Kubo-Anderson process [32] and Eq.(5.3) will be the solution for absorption spectra.

### 5.1.3 Isotropic rotational diffusion in discrete form

MSM model can be used for describing the rotational diffusion process for molecules by using a discretized form of diffusion equation [10, 33, 34]. The Hamiltonian that we consider here is the case where we have stationary eigenkets, i.e., we neglect the  $I_+$ ,  $I_-$  terms,

$$\frac{H(t)}{\gamma_e} = \omega_0 g_{zz}^{lab}(t) S_z + S_z A_{zz}^{lab}(t) I_z, \quad (5.5)$$

in which we define  $\omega_0 = B_0/g_e$ . The spin label is assumed to be rigidly fixed to a macromolecule that is freely diffusing in a solution. The components  $g_{zz}^{lab}$  and  $A_{zz}^{lab}$  are found by a transformation using Euler angles  $(\phi, \theta, \psi)$  on the diagonal matrix consisting of their xx, yy, and zz components in the molecular frame. For the cases in which their plane components x and y are equal to each other, i.e.,  $A_{xx} = A_{yy}$  and  $g_{xx} = g_{yy}$ , the only relevant diffusion coordinate is the angle  $\theta$ . Their transformation is given as

$$\begin{aligned} g_{zz}^{lab}(t) &= \cos^2(\theta(t)) g_{zz}^{mol} + \sin^2(\theta(t)) g_{xx}^{mol}, \\ A_{zz}^{lab}(t) &= \cos^2(\theta(t)) A_{zz}^{mol} + \sin^2(\theta(t)) A_{xx}^{mol}. \end{aligned} \quad (5.6)$$

Note that, we may subtract the rotation independent part, i.e.,  $tr(\mathbf{g})/3$ , in the first line of Eq.(5.6) which will result in a shift in the frequency axis as  $\omega \rightarrow \omega - \omega_0$ . In the MSM model of rotational diffusion,  $\theta$  is discretized according to the number of states  $s$  in the form  $\theta_k = (k - \frac{1}{2})\Delta\theta$ , where  $k=1,2,\dots,s$  and  $\Delta\theta = \pi/s$ . Following the arrangement of microstates, the purpose is to find the transition rate matrix  $\mathbf{K}$  for the discretized  $\theta$  coordinate. The calculation of the transition rate matrix from the discretized form of the rotational diffusion equation by using finite difference method is given in detail in Ref.[10]. Here, we apply the same procedure with reflective boundary conditions, and use transition rate matrix  $\mathbf{K}$  to solve Eq.(5.3), which takes much less time than taking average over various diffusion trajectories. The magnetization is a summation over different orientations of the nuclear spin  $m = -1, 0, 1$ , i.e.,  $M_+(t) = \Sigma_m M_+^m(t)/3$ , where the magnetization components have their distinct time evolution  $M_+^m(t) = \langle M_+^m(t) | p(t) \rangle$ , and therefore it is con-



venient to solve their contribution on the absorption spectra  $I(\omega)$  separately and add them together. As said before, the matrix  $\mathbf{\Omega}$  is the eigenfrequency matrix, whose components are in this case

$$\frac{h\nu^m}{\gamma_e} = \omega_0 g_{zz}^{lab} + mA_{zz}^{lab}. \quad (5.7)$$

Finally, for isotropic rotational diffusion, we have  $\langle v_{eq.} | = \langle \sin(\theta) |$  in Eq.(5.3).

#### 5.1.4 Isotropic rotational diffusion in continuous form

Another approach to this problem suggests generating Gaussian or uniform diffusion trajectories using the relevant diffusion constant and implying equilibrium conditions [11]. Accordingly, the rotation angle  $\theta$  is continuous, i.e., we can reach any angle between 0 and  $\pi$ , but the time-axis is discretized.

The diffusion equation using the Euler angles is solved by the Itô process [35, 36]. The equation of motion for angle  $\theta$  is given as

$$\Delta\theta_n = \sigma\Delta X_n + \frac{\sigma^2}{2\tan\theta_n}, \quad (5.8)$$

where  $n$  is the time step,  $\Delta X_n$  is the Brownian with mean zero, and  $\sigma = \sqrt{2D\Delta t}$ . The second term in Eq.(5.9) is due to the potential maintaining the path being in spherical coordinates. When this process is carried out by using a finite  $\Delta t$ , it makes strong jumps near the boundaries  $\theta = 0$  and  $\theta = \pi$ , which would cause a random noise. In order to get rid of this problem, it is convenient to take  $\Delta t$  as small as possible, but this takes more computational time. Alternatively, this problem is solved by using quaternion based Monte-Carlo approach [23, 37].

The absorption spectrum is calculated through the Fourier transform of the average magnetization, i.e.,

$$I(\omega) = \int_0^T \Sigma_m \langle M_+^m(t) | p(t) \rangle e^{-i\omega t} e^{-t/T_2} dt, \quad (5.9)$$

where again the normalization factor for intensity is ignored. The contribution of each trajectory to the magnetization is done by introducing their initial configuration from the equilibrium distribution, i.e.,  $p_{eq.}(\theta) = \sin(\theta)$ .

The comparison of the derivative spectra calculated from Brownian trajectories and MSM model is given in Fig. 5.1, to point out once more the equivalence of two methods. The magnetic tensor parameters are given as

$$(g_{xx}, g_{yy}, g_{zz})^{mol} = (2.00210, 2, 00210, 2.00775), \quad (5.10)$$

$$(A_{xx}, A_{yy}, A_{zz})^{mol} = (6.62, 6.62, 33.09) \text{ G}. \quad (5.11)$$

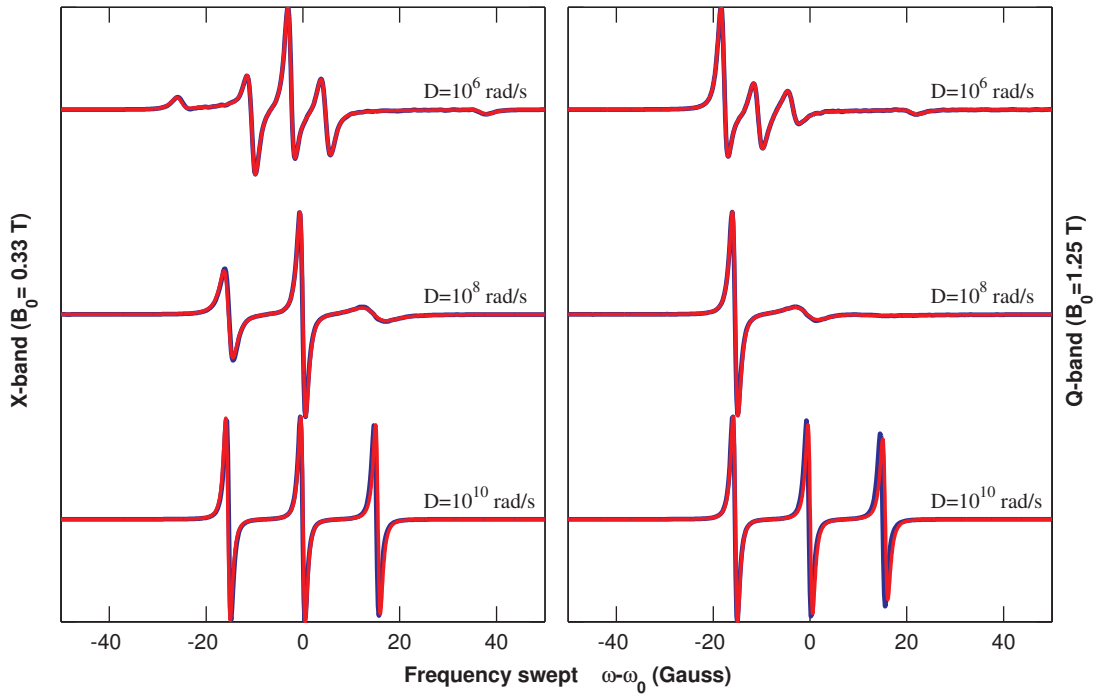


Figure 5.1: Derivative spectra generated from 100,000 Brownian trajectories (blue line) with time step  $\Delta t=0.005$  ns,  $\Delta t=0.025$  ns,  $\Delta t=0.5$  ns until magnetization significantly decays to zero, respectively  $t = 600$  ns,  $t = 1 \mu$ s,  $t = 5 \mu$ s (and for the ones with  $t < 2 \mu$  s zero-padded to  $2 \mu$  s) and calculated from MSM model (red line) with  $s=12, 18, 36$  states from bottom to top are compared. The two results are indistinguishable on the scale of this figure. Lorentzian broadening with  $T_2^L=0.8$  G is used. The magnetic tensor parameters are given in Eqs. (5.10,5.11).

For the discrete jump model, the convergence is reached with just  $s=36, 18, 12$  states for  $D = 10^6, 10^8, 10^{10}$  rad/s respectively. Thus, a lot of computational effort has been eliminated and minimized.

### 5.1.5 Reduction from continuous space to discrete coordinates

Reduction to finite number of microstates from the continuous model is done first by creating the discretized angle axis with the angle set  $\theta = \theta_1, \theta_2, \dots, \theta_s$ , and then using binning procedure for the angle such that if angle  $\theta(t)$  is between  $\theta_k - \Delta\theta/2$  and  $\theta_k + \Delta\theta/2$ , it is set as  $\theta(t) = \theta_k$  (Fig. 5.2). Accordingly, all the angles can be defined in such manner, and then we should be able to determine the transition probabilities between microstates.

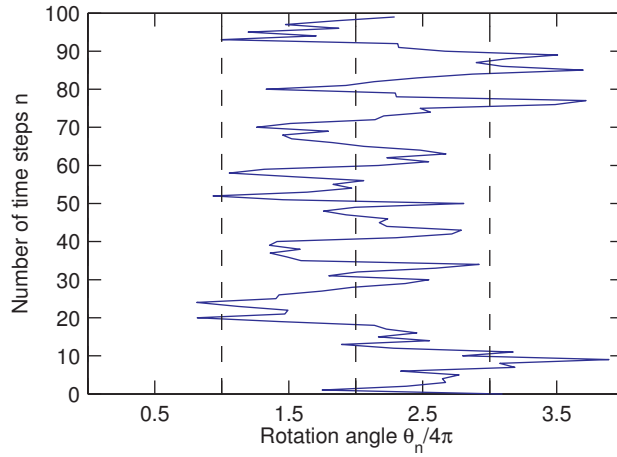


Figure 5.2: Simple reduction scheme from continuous to discrete coordinates for a Brownian trajectory for the  $s=4$  MSM model. If a point in the trajectory falls into one of these gridlines, it takes the value of that bin. Calculation of the transition matrix is done using the discretized coordinates determined by this scheme.

The solution to Eq.(5.1) is simply:

$$\langle p(t) | = \langle p(0) | \mathbf{U}(t) \quad (5.12)$$

or

$$\langle p(t + \Delta t) | = \langle p(t) | \mathbf{U}(\Delta t), \quad (5.13)$$

where  $\mathbf{U}(t) = e^{\mathbf{K}t}$  is the propagator for the microstate probability vector, or simply the transition probability matrix. In order to create the transition matrix from a Brownian diffusion trajectory, we should first be able to calculate the propagator matrix, take its matrix logarithm, divide by  $\Delta t$ . Our interest is in Eq.(5.13) and since we allow at most a single jump within a time step  $\Delta t$  and only one component

of  $\langle p(t) |$  is equal to 1 in a random trajectory, we may define  $\langle p(t) | = \langle i |$  and  $\langle p(t + \Delta t) | = \langle j |$ , where  $\langle i |$  and  $\langle j |$  are chosen among the orthonormal eigenbasis of microstates. Multiplying both sides by ket  $|j\rangle$  gives the matrix elements of  $\mathbf{U}(\Delta t)$ ,

$$1 = \langle i | \mathbf{U}(\Delta t) | j \rangle. \quad (5.14)$$

Single jump at a time means that there is a contribution to a single component (i,j) of the matrix  $\mathbf{U}(\mathbf{t})$  at each time step. Therefore, we should cover a long trajectory, and then take an average. The total probability of transitions from a state should be conserved, hence we should normalize the rows of the transition probability matrix  $\mathbf{U}(\mathbf{t})$ .

The timescale of events are governed by the rotational correlation time  $\tau_c = 1/(6D)$ . The resolution of the transition probability matrix will be determined by the number of time steps we take into account, and typically a minimum of 10,000 time steps with a time step around  $\Delta t \sim \tau_c/10$  is needed in order to have a reliable transition matrix. In this study, up to 40,000 time steps ( $\Delta t$  values are given in the figures) from a single diffusion trajectory are taken into account, which is especially needed when approaching to the rigid limit, i.e., for  $D = 10^6$  rad/s in Fig. 5.3.

Finally, the equilibrium probability density vector can be determined from both transition matrix or occupancy rates. In this study we use the latter. Now we have all entries for Eq.(5.3) and Eq.(5.4) and can solve for the absorption spectrum. Alternatively, one can always calculate the average magnetization in time domain with the given ingredients. The comparison between the derivative spectra generated from 100,000 Brownian trajectories and from MSM model with transition matrix obtained from a single Brownian trajectory with 40,000 time steps is given in Fig. 5.3.

This approach can easily be applied to the calculation of absorption spectra from a single MD trajectory, and resolution of time steps can be taken same as the relevant MD simulation. In the next subsection, the extension to another rotation angle will be demonstrated before finally discussing the use for short MD

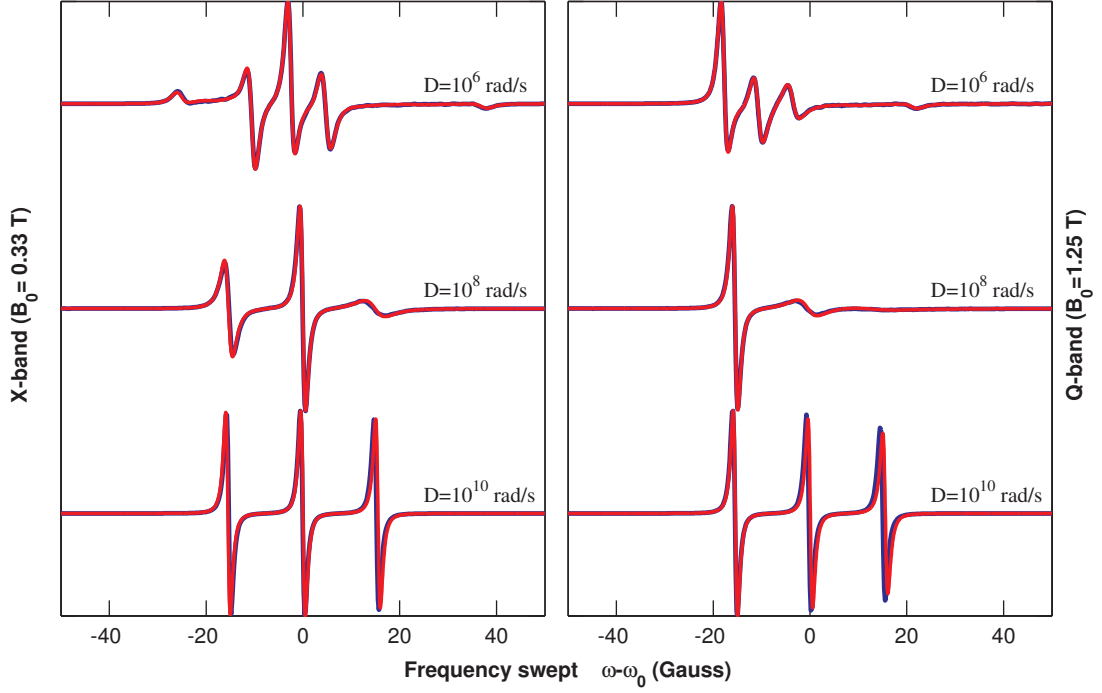


Figure 5.3: Derivative spectra generated from 100,000 Brownian trajectories (blue line) same as in Fig. 5.1 and calculated from MSM model (red line) with transition matrix obtained from a single Brownian trajectory with 40,000 time steps having  $s=12, 18, 36$  states from bottom to top are compared. The two results are indistinguishable on the scale of this figure. Lorentzian broadening with  $T_2^L=0.8$  G is used. The magnetic tensor parameters are given in Eqs. (5.10,5.11).

trajectories and the possibilities of having a continuous spatial diffusion entangled to a  $m$ -state Markov model.

### 5.1.6 Extension to other coordinates

The diffusion operator that we want to consider is in the form

$$\Gamma(\theta, \phi) = D \frac{1}{\sin\theta(t)} \frac{\partial}{\partial\theta} \sin\theta(t) \frac{\partial}{\partial\theta} + \frac{D}{\sin^2\theta(t)} \frac{\partial^2}{\partial\phi^2}. \quad (5.15)$$

Let us define the transition rates for diffusion operator for angle  $\theta$  with  $s_1 \times s_1$  matrix  $\mathbf{K}_\theta$  and for the operator  $D \frac{\partial^2}{\partial\phi^2}$  with  $s_2 \times s_2$  as  $\mathbf{K}_\phi$  matrix, where  $s_1, s_2$  are the numbers of eigenstates for angles  $\theta$  and  $\phi$  respectively. Hence, the transition rate operator in Eq.(5.3) will be a  $s_1 s_2 \times s_1 s_2$  matrix

$$\mathbf{K}_{\theta\phi} = \mathbf{K}_\theta \otimes \mathbf{I}_{s_2} + \mathbf{M} \otimes \mathbf{K}_\phi. \quad (5.16)$$

$\mathbf{M}$  is a  $s_1 \times s_1$  diagonal matrix with elements  $1/\sin^2(\theta_k)$  remembering  $k = 1, 2, \dots, s_1$ , and  $\mathbf{I}_{s_2}$  is  $s_2 \times s_2$  identity matrix. The transition matrix in this case is expanded in  $|\theta, \phi\rangle = |\theta\rangle_{s_1} |\phi\rangle_{s_2}$  space,

$$|\theta, \phi, m\rangle = |\theta\rangle_{s_1} |\phi\rangle_{s_2} |m\rangle_3, \quad (5.17)$$

where  $|\theta\rangle, |\phi\rangle$  are respectively  $s_1, s_2$  dimensional vectors, and  $|m\rangle = [1, 1, 1]^T$ . At equilibrium, the state vector becomes  $|\sin\theta\rangle |1\rangle |1\rangle$ . Thus, it is the general formalism for an electron spin that is coupled to a magnetic field and nuclear spin, on a rotating frame with Euler angles  $(\theta, \phi)$ . For simplicity, we eliminated the ket  $|m\rangle$ , in Section 5.1.3, by calculating a simple summation over  $m$  states. The equation for absorption spectra in Eq.(5.3) becomes

$$I(\omega) = \langle v_{eq}. | (i\omega + i\mathcal{L} - \mathbf{K}_{\theta\phi\mathbf{m}})^{-1} |1\rangle_{s_1 \times s_2 \times 3}, \quad (5.18)$$

which will give the derivative absorption spectra as:

$$\frac{\partial I(\omega)}{\partial \omega} = -i \langle v_{eq}. | (i\omega + i\mathcal{L} - \mathbf{K}_{\theta\phi\mathbf{m}})^{-2} |1\rangle_{s_1 \times s_2 \times 3}, \quad (5.19)$$

where  $\mathcal{L}$  is the Liouvillian operator extended to  $\theta$  and  $\phi$  basis and  $\mathbf{K}_{\theta\phi\mathbf{m}}$  is the transition matrix extended to  $|m\rangle$  basis, hence  $\mathbf{K}_{\theta\phi\mathbf{m}} = \mathbf{K}_{\theta\phi} \otimes \mathbf{I}_3$ . The spin-spin relaxation rate which will result a Lorentzian broadening of  $\gamma_e T_2^L$  in the spectrum, can be included in same manner as shown in Eq.(5.4). Note that we should divide each term in the paranthesis by gyromagnetic ratio  $\gamma_e$  in order to see the spectrum in Gauss (G) units.

Including  $I_+, I_-$  terms in Hamiltonian, we will have  $\mathcal{H} = H(t)/\gamma_e$ :

$$\mathcal{H} = \omega_0 g_{zz}^{lab} S_z + S_z (A_{zx}^{lab} I_x + A_{zy}^{lab} I_y + A_{zz}^{lab} I_z) \quad (5.20)$$

which can be represented in matrix form as:

$$\mathcal{H} = \frac{1}{2} \left( \begin{array}{c|c} \mathcal{H}^\uparrow & \\ \hline & \mathcal{H}^\downarrow \end{array} \right) \quad (5.21)$$

where  $\mathcal{H}^\uparrow = -\mathcal{H}^\downarrow$ , and given as:

$$\mathcal{H}^\uparrow = \begin{pmatrix} \omega_0 g_{zz}^{lab} + A_{zz}^{lab} & \frac{1}{\sqrt{2}}(A_{zx}^{lab} - iA_{zy}^{lab}) & 0 \\ \frac{1}{\sqrt{2}}(A_{zx}^{lab} + iA_{zy}^{lab}) & \omega_0 g_{zz}^{lab} & \frac{1}{\sqrt{2}}(A_{zx}^{lab} - iA_{zy}^{lab}) \\ 0 & \frac{1}{\sqrt{2}}(A_{zx}^{lab} + iA_{zy}^{lab}) & \omega_0 g_{zz}^{lab} - A_{zz}^{lab} \end{pmatrix}. \quad (5.22)$$

Liouvillian operator in this case is expanded in  $|\theta\rangle_{s_1} |\phi\rangle_{s_2} |m\rangle_{s_3}$  basis such as for example when  $s_1 = 3$ ,

$$\mathcal{L}(\{\theta\}, \{\phi\}) = \left( \begin{array}{c|c|c} \mathcal{L}(\theta_1, \{\phi\}) & & \\ \hline & \mathcal{L}(\theta_2, \{\phi\}) & \\ \hline & & \mathcal{L}(\theta_3, \{\phi\}) \end{array} \right) \quad (5.23)$$

and  $\mathcal{L}(\theta_k, \{\phi\})$  is extended in itself with the same hierarchy depending on the number of  $\phi$  states,  $s_2$ . We have concluded that the Hamiltonian in Eq.(5.21) is our relevant Liouvillian operator, i.e.,  $\mathcal{L}(\{\theta\}, \{\phi\}) = \mathcal{H}^\uparrow(\{\theta\}, \{\phi\})$  using the Hermiticity of both the Hamiltonian and the density matrix [38] and after tracing with  $S_+$  operator. The elements of  $\mathbf{A}^{lab}$  and  $\mathbf{g}^{lab}$  matrices are obtained as a function of three Euler angles  $(\phi, \theta, \psi)$ , defined with a transformation:

$$\mathbf{A}^{lab} = R(\phi, \theta, \psi) \mathbf{A}^{mol} R^T(\phi, \theta, \psi) \quad (5.24)$$

where  $R(\phi, \theta, \psi)$ , is the rotation matrix from molecular frame to lab frame.

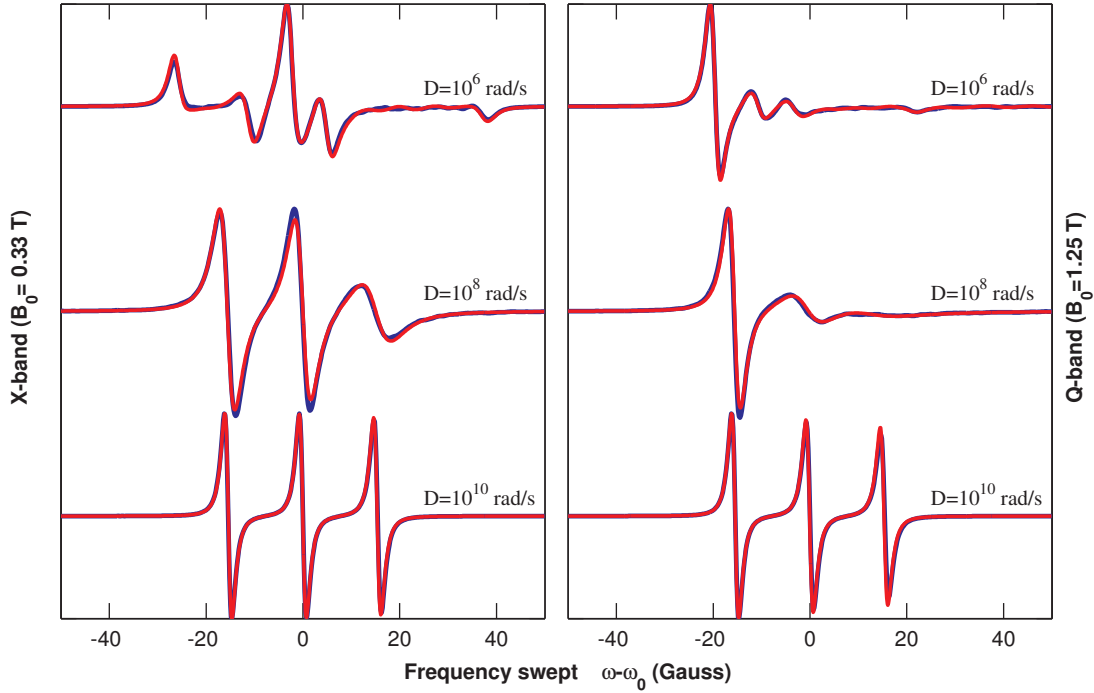


Figure 5.4: Derivative spectra generated from 20,000 Brownian trajectories (blue line) with time step  $\Delta t=0.010$  ns,  $\Delta t=0.2$  ns,  $\Delta t=0.5$  ns until magnetization significantly decays to zero, respectively  $t = 400$ ns,  $t = 700$ ns,  $t = 2.5\mu$ s (and for the ones with  $t < 2 \mu$ s zero-padded to  $2 \mu$ s) and calculated from MSM model (red line) of single Brownian trajectory with 40,000 timesteps having  $\Delta t=0.005$  ns,  $\Delta t=0.2$  ns,  $\Delta t=25$  ns with  $(s_1, s_2)=(12,5)$  (18,5) (21,5) states from bottom to top are compared. The two results are indistinguishable on the scale of this figure. Lorentzian broadening with  $T_2^L=1.25$  G is used. The magnetic tensor parameters are given in Eqs. (5.10,5.11).

For creating the transition matrix, the discrete form of the diffusion operator in Eq.(5.15) may not represent successfully the spherical rotation, and instead of that we will use the methodology introduced in Section 5.1.5 extended to  $|\theta\rangle_{s_1} |\phi\rangle_{s_2}$  space, therefore we will first create a trajectory long enough which is generated by quaternion based Monte-Carlo algorithm, and then take the statistics from that trajectory. The definition of Euler angles in terms of quaternions and their time evolution is explained in detail in Ref.[23] and Ref.[37], and also included in Appendix A. For the trajectory method, we need to keep track of evolution



of density matrix and calculate average magnetization as a function of time from various trajectories, and then take the Fourier transform to obtain spectrum as shown in Eq.(5.9). The evolution of transverse magnetization in trajectory method is explained in Appendix B. The comparison between two methods for isotropic rotation with angles  $(\theta, \phi)$ , using magnetic tensor parameters in Eqs. (5.10,5.11) is shown in Fig. 5.4 and yield a very good agreement.

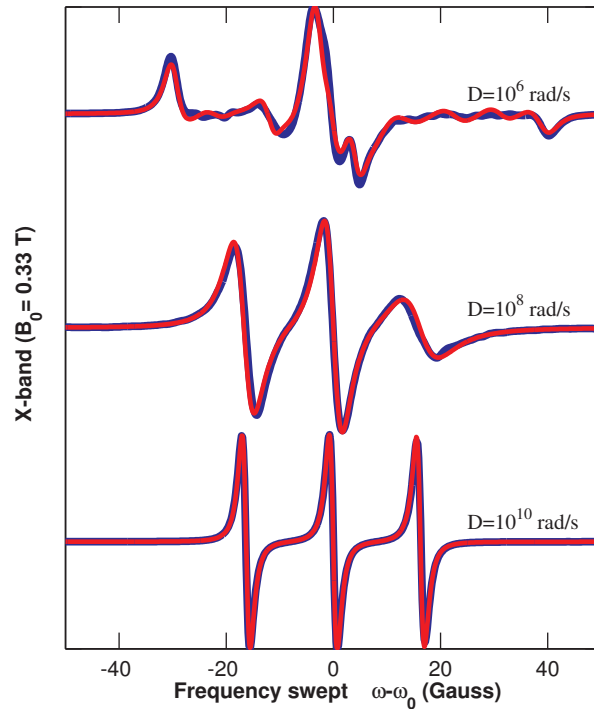


Figure 5.5: Derivative spectra generated from 20,000 Brownian trajectories (blue line) with time step  $\Delta t=0.010$  ns,  $\Delta t=0.2$  ns,  $\Delta t=0.5$  ns until magnetization significantly decays to zero, respectively  $t = 400$ ns,  $t = 700$ ns,  $t = 2.5$   $\mu$ s (and for the ones with  $t < 2$   $\mu$ s zero-padded to 2  $\mu$ s) and calculated from MSM model (red line) of single Brownian trajectory with 40,000 time steps having  $\Delta t=0.005$  ns,  $\Delta t=0.2$  ns,  $\Delta t=25$  ns with  $(s_1, s_2, s_3)=(12,3,2)$   $(18,3,2)$   $(12,3,5)$  states from bottom to top are compared. The two results are indistinguishable on the scale of this figure. Lorentzian broadening with  $T_2^L=1.25$  G is used. The magnetic tensor parameters are given as  $(g_{xx}, g_{yy}, g_{zz})^{mol} = (2.0082, 2.0060, 2.0023)$  and  $(A_{xx}, A_{yy}, A_{zz})^{mol} = (7.0, 6.0, 36.0)G$ .

Using the procedure applied in Eqs. (5.18-23), it is straightforward to extend angle space into  $|\theta, \phi, \psi\rangle = |\theta\rangle_{s_1} |\phi\rangle_{s_2} |\psi\rangle_{s_3}$  space. The comparison between two methods for isotropic rotation with angles  $(\theta, \phi, \psi)$ , using magnetic tensor parameters  $(g_{xx}, g_{yy}, g_{zz})^{mol} = (2.0082, 2.0060, 2.0023)$  and  $(A_{xx}, A_{yy}, A_{zz})^{mol} =$

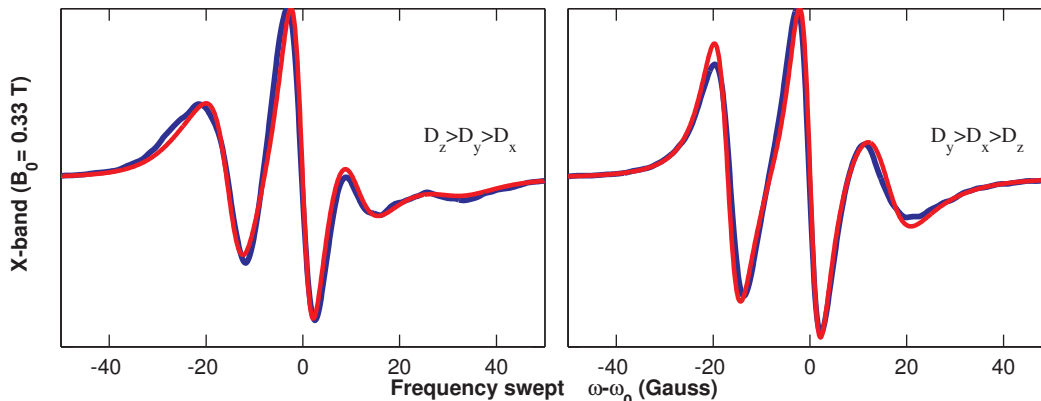


Figure 5.6: Derivative spectra generated from 25,000 Brownian trajectories (blue line) for fully anisotropic rotational motion with time step  $\Delta t=0.2$  ns until 200 ns for each trajectory (then, zero-padded to  $2 \mu\text{s}$ ), and calculated from MSM model (red line) of single Brownian trajectory with 40,000 time steps having  $\Delta t=0.2$  ns are compared. In the left figure, we have  $D_x = D/5, D_y = D/2, D_z = D$  using MSM with  $(s_1, s_2, s_3)=(30,3,2)$  while in the right figure, we have  $D_x = D/2, D_y = D, D_z = D/5$  using MSM with  $(s_1, s_2, s_3)=(36,5,2)$ . For both cases,  $D = 10^8$  rad/s and Lorentzian broadening with  $T_2^L=1.8$  G is used. The magnetic tensor parameters are same as in Fig. 5.5.

$(7.0, 6.0, 36.0)G$  is shown in Fig. 5.5 and resulted a very good agreement. We have also made the comparison for fully anisotropic diffusion of cases  $D_z > D_y > D_x$  and  $D_y > D_x > D_z$  in Fig. 5.6, where  $D_x, D_y, D_z$  are respectively diffusion constants for rotation around x, y, z axes. The results seem to deliver a good result but need improvement whether by increasing the number of events in single Brownian trajectory or increasing the number of states and/or developing the binning method. It is also observed that convergence to the spectra obtained from 25,000 Brownian trajectories is mostly and highly dependent on the accuracy of motional statistics along  $\theta$  axis.

### 5.1.7 Application to short Brownian trajectories

In this section, our purpose is to discuss the applicability of the presented approach to short MD simulations. As a specific case, we will continue with isotropic rotational diffusion up to 100 ns. In that case, we would not expect to get the correct results for the rare event case, i.e., rigid limit,  $D = 10^6$  rad/s. Therefore, for such examples, it is better to estimate rotational correlation time, and perform

simulations. On the other extreme, we expect and obtain a perfect convergence (data not shown) for fast motion limit, i.e.,  $D = 10^{10}$  rad/s for all independent single trajectories. Our interest will be on the case of slow motional regime having  $D = 10^8$  rad/s. The procedure is the same as in Section 5.1.5 and 5.1.6, except that this time we have a Brownian trajectory of 100 ns.

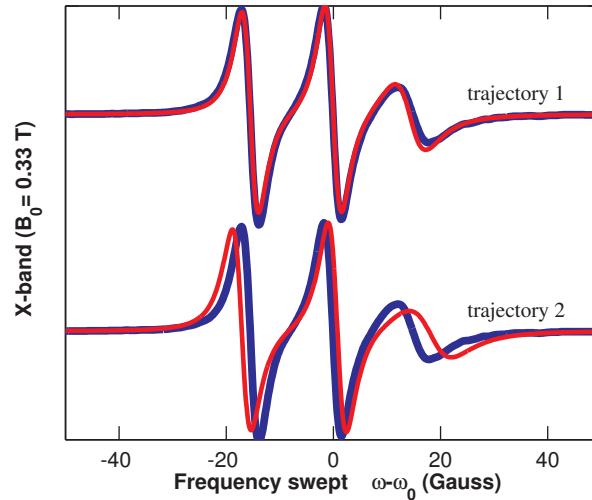


Figure 5.7: Derivative spectra for  $D = 10^8$  rad/s calculated from MSM model (red line) of single Brownian trajectory until 100 ns having  $\Delta t = 0.1$  ns, with  $(s_1, s_2) = (18, 5)$  states. Upper and lower figures are for different realizations of the single Brownian trajectory, blue lines are for comparison with the derivative spectra generated from 20,000 Brownian trajectories (blue lines) with time step  $\Delta t = 0.2$  ns until 700 ns as in Fig. 5.4. Lorentzian broadening with  $T_2^L = 1.25$  G is used. The magnetic tensor parameters are given in Eqs. (5.10, 5.11).

For the diffusion process with  $D = 10^8$  rad/s the rotational correlational time is  $\tau_c \approx 1.667$  ns. Thus, the motion will still not reach some regions in phase space. Accordingly, when creating the transition probability matrix we may observe unvisited sections. It is important to eliminate rows with zero event, not only for computational ease but also not to get a singular matrix. As a result, for example, while starting with  $s = 18$  state model, we may end up with a  $14 \times 14$  matrix instead of  $18 \times 18$ . This also shows that some statistical improvement is necessary when creating the gridlines. In our calculations, we have just followed the scheme that is creating gridlines equal in length. As seen in Fig. 5.7, the convergence of the derivative spectra calculated from MSM of single short Brownian trajectory to the one obtained from 20,000 trajectories may depend on the realization. In that

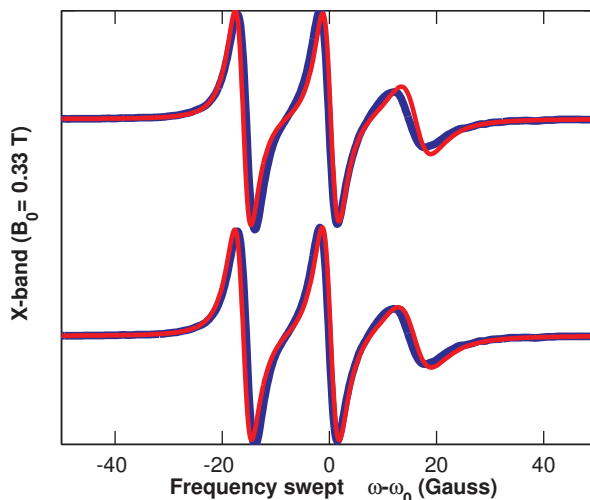


Figure 5.8: Derivative spectra for  $D = 10^8$  rad/s calculated from MSM model (red line) of statistics obtained from 5 independent Brownian trajectories until 100 ns having  $\Delta t=0.1$  ns. Upper figure is obtained from  $(s_1, s_2)=(18,5)$  state model and lower figure is obtained by increasing number of states, i.e.,  $(s_1, s_2)=(32,5)$ , and shows a better agreement, blue lines are for comparison with the derivative spectra generated from 20,000 Brownian trajectories (blue lines) with time step  $\Delta t=0.2$  ns until 700 ns as in Fig. 5.4. Lorentzian broadening with  $T_2^L=1.25$  G is used. The magnetic tensor parameters are given in Eqs. (5.10,5.11).

case, we may need more information about the type of motion. This is shown in Fig. 5.8 with the same MSM having a transition matrix obtained from 5 independent trajectories, and it shows a better agreement. The convergence to the one obtained from 20,000 trajectories increases further with higher number of  $\theta$  states.

### 5.1.8 Discussion and conclusions

As a further step, having a process such as spatial diffusion of molecule under a potential that is an element of m-state potential space in which the potential is selected by a Markov process, may be helpful in understanding the effect of conformational changes in the spin dynamics [25]. For example, a diffusive process that has a m-fold selective potential for the angle  $\theta$  can be introduced, such as with m=A state for  $\theta \in [0, \pi/2]$  and m=B state  $\theta \in [\pi/2, \pi]$ . This will help to get a quick feedback about the credibility of the model for the given MD simulation results by reducing the set of variables. If the simulations are done distinctly for two different types of potentials [20, 21], then the overall transition rate matrix

can be created by their extension to the potential subspace, i.e., taking their Kronecker product with potential change rate matrix, and summing them up. Alternatively, if these two type of potentials are completely separable, then the two simulations can be defined in one transition probability matrix, by adding their records of jumps as if they are in the same trajectory, one being in the starting section, and the other in the second section, and their own lengths in time axis will be directly related to their equilibrium distribution and transition rates among these two types of potentials. On the other hand, for slowly varying potentials due to internal dynamics, this approach will be insufficient for not recognizing non-Markovian processes and therefore one has to model rotational motion of the molecule entangled with the effects of the conformational changes on the spin label itself, as defined in the upper statement and previous examples [25, 28].

In summary, we have simulated the cw-ESR spectrum of a spin-1/2 electron coupled to a magnetic field and spin-1 nucleus for X- and Q- bands by using both discrete isotropic rotational diffusion and continuous Brownian diffusion processes. In addition to that, calculated derivative spectra from the MSM model with transition matrix obtained from a single Brownian trajectory by statistical binning process and the spectra generated from the average of large number of Brownian trajectories are compared and resulted in a very good agreement. It is suggested that this method can be implemented to calculate absorption spectra from MD simulation data. One of its advantages is that due to its reduction of computational effort, the parametrization process will be quicker. Secondly, the transition matrix defined in this manner, may indicate separable potential changes during the motion of the molecule. It is also possible to change the course of single trajectory by hand and observe its consequences. Thirdly, one can calculate the ESR spectra from a single MD trajectory directly without extending it artificially in the time axis. However, for short MD trajectories, the required statistical information can not be obtained depending on the timescale of transitions. Therefore, some statistical improvement will be needed in order to reach a better convergence. On the other hand, if there is a requirement of high precision in the extended coordinates, it will enlarge the transition matrix and therefore will take more computational time. Hence, reducibility of relevant coordinates is

undoubtedly necessary to maintain the efficiency of the present framework. It is hoped that, in the following studies, this framework will be helpful in extracting the statistics of motional information of a molecule or implementing additional motional information on the spin label under various kinds of potentials.

### 5.1.9 Appendix

#### Quaternion dynamics

For the generation of Brownian trajectories, we have used the conjecture in Ref. [23] in which the detailed calculations can be found. Only difference is that here we use Gaussian random processes, instead of random uniform displacements. Euler angles  $(\phi, \theta, \psi)$  defined in terms of quaternions as:

$$\mathbf{q}(t) = \begin{pmatrix} q_0(t) \\ q_1(t) \\ q_2(t) \\ q_3(t) \end{pmatrix} = \begin{pmatrix} \cos \frac{\theta(t)}{2} \cos \frac{(\phi(t)+\psi(t))}{2} \\ \sin \frac{\theta(t)}{2} \sin \frac{(\phi(t)-\psi(t))}{2} \\ -\sin \frac{\theta(t)}{2} \cos \frac{(\phi(t)-\psi(t))}{2} \\ -\cos \frac{\theta(t)}{2} \sin \frac{(\phi(t)+\psi(t))}{2} \end{pmatrix} \quad (5.25)$$

satisfying  $q_0^2(t) + q_1^2(t) + q_2^2(t) + q_3^2(t) = 1$ , therefore it is still a function of 3 independent variables. Using the equation relating angular velocities around  $x, y, z$  axes with the time derivative of Euler angles and converting it to quaternion formalism, one would get the equation of motion as:

$$\mathbf{q}(t + \Delta t) = e^{\mathbf{P}\Delta t/2} \mathbf{q}(t) \quad (5.26)$$

where  $\mathbf{P}$  is defined in the form of

$$\mathbf{P} = \begin{pmatrix} 0 & \omega_x & \omega_y & \omega_z \\ -\omega_x & 0 & \omega_z & -\omega_y \\ -\omega_y & -\omega_z & 0 & \omega_x \\ -\omega_z & \omega_y & -\omega_x & 0 \end{pmatrix}. \quad (5.27)$$

$\omega_x, \omega_y, \omega_z$  are respectively angular velocities around  $x, y, z$  axes. As a realization of Brownian trajectory, we can evaluate  $\mathbf{P}\Delta t$  with 3 independent random Gaussian

displacements. Thus, we introduce  $\omega_i \Delta t = \sigma_i \Delta U_i$ , where  $\Delta U_i$  is a Brownian with mean zero and  $\sigma_i = \sqrt{2D_i \Delta t}$ , with  $D_i$  as diffusion constant for rotation around  $i^{th}$  axis. Simplifications for the time evolution of quaternions is shown in the related reference.

Rotation given by three Euler angles defined with the rotation matrix  $R(\phi, \theta, \psi) = R_z(\psi)R_x(\theta)R_z(\phi)$  which can be written in terms of quaternions as

$$R(t) = \begin{pmatrix} q_0^2 + q_1^2 - q_2^2 - q_3^2 & -2(q_0q_3 - q_1q_2) & 2(q_0q_2 + q_1q_3) \\ 2(q_0q_3 + q_1q_2) & q_0^2 - q_1^2 + q_2^2 - q_3^2 & -2(q_0q_1 - q_2q_3) \\ -2(q_0q_2 - q_1q_3) & 2(q_0q_1 + q_2q_3) & q_0^2 - q_1^2 - q_2^2 + q_3^2 \end{pmatrix}. \quad (5.28)$$

Accordingly, one can use directly the rotation matrix in this form to implement Eq.(5.24) and calculate the Hamiltonian. In our conjecture for calculating the transition matrix from discretized coordinates, we take the information by converting quaternions to three Euler angles at each time step throughout the trajectory. It is also possible to consider an application of binning process over quaternions which are taking values between -1 and 1 with the condition  $q_0^2(t) + q_1^2(t) + q_2^2(t) + q_3^2(t) = 1$ , and therefore belonging to a process of 3 independent variables. In this study, we have implemented binning process only on to angle values.

### Propagation of magnetization

The time dependent transverse magnetization observable is obtained as:

$$M_+ = Tr(\rho S_+). \quad (5.29)$$

As our Hamiltonian shown in Eq.(5.5) and Eqs.(5.20-22), we will have a  $6 \times 6$  density matrix.  $S_+$  operator in that basis will act on only  $\rho_+$  section of density matrix which is shown in  $\rho$  as,

$$\rho = \left( \begin{array}{c|c} & \\ \hline & \\ \hline \rho_+ & \end{array} \right) \quad (5.30)$$

and hence  $M_+ = Tr(\rho_+)$ . As a consequence we will need only the time evolution of  $\rho_+$  to calculate time dependent magnetization. In short time dynamics, i.e., for small  $\Delta t$  its time evolution can be calculated with [37]

$$\rho_+(t + \Delta t) = e^{i(\gamma_e \mathcal{H}^\dagger) \Delta t} \rho_+(t) e^{i(\gamma_e \mathcal{H}^\dagger) \Delta t}. \quad (5.31)$$

Finally, initial condition of  $\rho_+$  being a  $3 \times 3$  identity matrix, i.e.,  $\rho_+(0) = \mathbf{I}_3$  is implemented and propagation of that matrix is followed with its trace being recorded at each time step throughout the trajectory. Average magnetization that is needed to solve Eq.(5.9) is calculated over different realizations of Brownian diffusion with their appropriate  $\sin(\theta)$  weight.

### Computational details

The calculations are performed by MATLAB R2012b using a single core Intel<sup>®</sup> Xeon<sup>®</sup> Processor E5420 with base frequency at 2.50 Ghz.

### Trajectory method

Calculations are done with a simple process consisting of loop for time steps  $n_{time}$ , inside a loop for number of trajectories  $N_{traj}$  in which the magnetization is determined as shown in the text and Appendix B. For the evaluation of exponentials in Eqs.(5.26) and (5.31), we have used the simplifications suggested in the related references. To obtain the derivative spectrum, a Fast Fourier Transform is held using `fft` function in MATLAB.

For the calculation of average magnetizations it is seen that there is a linear increase with number of steps as well as with number of trajectories. For ex., from average over 5 computations we have observed that for diffusion of  $(\theta, \phi)$  with 5,000 time steps ( $n_{time}$ ) and 10,000 Brownian trajectories ( $N_{traj}$ ) average run time is  $t_{av} = 12257.6s$  with a standard deviation  $\sigma_t = 85.48s$ , whereas with  $n_{time}=5,000$  and  $N_{traj}=5,000$ , we had  $t_{av} = 6080.5s$  and  $\sigma_t = 28.51s$ , with  $n_{time}=5,000$  and  $N_{traj}=1,000$ , we had  $t_{av} = 1223s$  and  $\sigma_t = 10.06s$ , and finally with  $n_{time}=1,000$  and  $N_{traj}=1,000$ , we had  $t_{av} = 244.6s$  and  $\sigma_t = 1.07s$ . In addition to that, we have observed computation values for the case of diffusion of  $(\theta, \phi, \psi)$  being very similar



values such as with  $n_{time}=1,000$  and  $N_{traj}=1,000$ ,  $t_{av} = 258.4s$  and  $\sigma_t = 1.97s$ . Accordingly, the computation values for each case obtained in this study can be determined from the relation  $t_{av} \propto N_{traj}n_{time}$ , and using

*( $\theta$ )diffusion*

$$\Delta t = 0.005ns \longrightarrow 500ns \longrightarrow 100,000steps$$

$$\Delta t = 0.025ns \longrightarrow 1\mu s \longrightarrow 40,000steps$$

$$\Delta t = 0.5ns \longrightarrow 5\mu s \longrightarrow 10,000steps$$

*( $\theta, \phi$ )diffusion*

$$\Delta t = 0.010ns \longrightarrow 400ns \longrightarrow 40,000steps$$

$$\Delta t = 0.2ns \longrightarrow 700ns \longrightarrow 3,500steps$$

$$\Delta t = 0.5ns \longrightarrow 2\mu s \longrightarrow 4,000steps$$

*( $\theta, \phi, \psi$ )diffusion*

$$\Delta t = 0.010ns \longrightarrow 400ns \longrightarrow 40,000steps$$

$$\Delta t = 0.2ns \longrightarrow 700ns \longrightarrow 3,500steps$$

$$\Delta t = 0.5ns \longrightarrow 2.5\mu s \longrightarrow 5,000steps.$$

It should be noted that the computation times for only ( $\theta$ ) diffusion are much lower than for the given examples, and it is completed within a few minutes or less while it takes less than 10 seconds for MSM method. Furthermore, convergence is reached with around 5,000-10,000 trajectories for ( $\theta$ ) diffusion and with more than 10,000 trajectories for two and three angles diffusions. Another point is that one can also reduce computation times by changing the total number of time steps (depending on additional broadenings) and time step value  $\Delta t$ , e.g., for fast

motional limit, i.e.  $D = 10^{10}$  rad/s, one can get the same results (data not shown) with  $\Delta t = 50ps$ .

After calculation of average magnetization, Fast Fourier Transform is performed using `fft` function in MATLAB, which is completed within seconds for up to 10,000 time steps (including zero-padding), and depending on the size of time array the computation time may extend drastically.

### MSM model of single Brownian trajectory

The computation of derivative spectra from MSM of a single trajectory consists of *i*) generation of single Brownian trajectory *ii*) creation of transition matrix as explained in Section 5.1.5, *iii*) calculation of energies for allowed states (depending on the number of states), *iv*) calculation of derivative spectra using formula in Eq.(5.19) for 796 points between frequencies  $\omega - \omega_0 = [-50, 50]$  G. Computation times for derivative spectra in the case of  $(\theta, \phi)$  and  $(\theta, \phi, \psi)$  diffusion which are exhibited in Fig. 5.4 and Fig. 5.5, are shown respectively in Table 5.1 and Table 5.2.

For much larger matrices, this method becomes problematic, and decrease the computer efficiency drastically, with taking the logarithm and then the inverse of large matrices. In such cases, better optimizations and algorithms will be needed to improve this methodology.

States (s1,s2)	$t_{av}$	$\sigma_t$
(12,5)	7.29 s	0.042 s
(18,5)	21.42 s	0.269 s
(21,5)	32.83 s	0.086 s

Table 5.1: Average computation times  $t_{av}$  and standard deviations  $\sigma_t$  over 5 runs for calculation of spectra with  $(\theta, \phi)$  diffusion.

---

States (s1,s2,s3)	$t_{av}$	$\sigma_t$
(12,3,2)	11.82 s	0.073 s
(18,3,2)	36.01 s	0.357 s
(12,3,5)	43.48 s	0.922 s

Table 5.2: Average computation times  $t_{av}$  and standard deviations  $\sigma_t$  over 5 runs for calculation of spectra with  $(\theta, \phi, \psi)$  diffusion.

## REFERENCES

- [1] J. L. Berliner, *Spin Labeling: Theory and Applications* (Academic Press: New York, 1979).
- [2] P. P. Borbat, A. J. Costa-Filho, K. A. Earle, J. K. Moscicki, J. H. Freed, *Science* **291**, 266 (2001).
- [3] J. P. Klare and H.-J. Steinhoff, M. Muller, *Photosynth. Res.* **102**, 337 (2009).
- [4] P. W. Anderson, *J. Phys. Soc. Jpn.* **9**, 316 (1954).
- [5] R. Kubo, *J. Phys. Soc. Jpn.* **9**, 935 (1954).
- [6] R. Kubo, *Adv. Chem. Phys.* **15**, 101 (1969).
- [7] A. Redfield, *IBM J. Res. Dev.* **1**, 19 (1957).
- [8] A. Abragam, *The Principles of Nuclear Magnetism* (Oxford University Press, 1961).
- [9] D. J. Schneider and J. H. Freed, *Adv. Chem. Phys.* **73**, 387 (1989).
- [10] B. H. Robinson, L. J. Slutsky, and F.P. Auteri, *J. Chem. Phys.* **96**, 2609 (1992).
- [11] H.-J. Steinhoff and W. Hubbell, *Biophys. J.* **71**, 2201 (1996).
- [12] H.-J. Steinhoff, M. Muller, C. Beier, and M. Pfeiffer, *J. Mol. Liq.* **84**, 17 (2000).
- [13] Z. Liang, Y. Lou, J. H. Freed, L. Columbus, and W. L. Hubbell, *J. Phys. Chem B.* **108**, 17,649 (2004).
- [14] K. Murzyn, T. Rog, W. Blicharski, M. Dutka, J. Pyka, S. Szytula, and W. Froncisz, *C. Proteins.* **62** 1088 (2006).
- [15] H. S. Mchaourab, P. R. Steed, and K. Kazmier, *Structure* **19**, 1549 (2011).
- [16] P. Cekan, S. T. Sigurdsson, *J. Am. Chem. Soc.* **131**, 18,054 (2009).
- [17] M. Bennatia and T. F. Prisner, *Rep. Prog. Phys.* **68** (2005).

- [18] P. Maragakis, K. Lindorff-Larsen, M. P. Eastwood, R. O. Dror, J. L. Klepeis, I. T. Arkin, M. O. Jensen, H. Xu, N. Trbovic, R. A. Friesner, A. G. Palmer, and D. E. Shaw, *J. Phys. Chem. B.* **112**, 6155 (2008).
- [19] L. Columbus, T. Kalai, J. Jeko, K. Hideg, and W. L. Hubbell, *Biochemistry* **40** 3828 (2001).
- [20] I. Stoica, *J. Phys. Chem. B.* **108**, 1771 (2004).
- [21] C. Beier and H. J. Steinhoff, *Biophys. J.* **91** (2006).
- [22] D. Hamelberg, C. A. F. de Oliveira, and J. A. McCammon, *J. Chem. Phys.* **127** 155102 (2007).
- [23] S. DeSensi, D. Rangel, A. Beth, T. Lybrand and E. Hustedt, *Biophys. J.* **94**, 3798 (2008).
- [24] D. Sezer, J. H. Freed, and B. Roux, *J. Phys. Chem.* **112**, 11014 (2008).
- [25] D. Sezer and B. Roux, in *An Introduction to Markov State Models and Their Application to Long Timescale Molecular Simulations*, edited by G. Bowman, V. Pande and F. Noe, (Springer, 2014).
- [26] C. R. Schwantes, R. T. McGibbon, and V. S. Pande, *J. Chem. Phys.* **141**, 090901 (2014).
- [27] R. T. McGibbon, C. R. Schwantes, and V. S. Pande, *J. Phys. Chem. B* **118**, 6475 (2014).
- [28] V. S. Oganessian, *J. Magn. Reson.* **188**, 196 (2007).
- [29] V. S. Oganessian, E. Kuprusevicius, H. Gopee, A. N. Camidge, and M. R. Wilson, *Phys. Rev. Lett.* **102**, 013005 (2009).
- [30] V. S. Oganessian, *Phys. Chem. Chem. Phys.* **13**, 4724 (2011).
- [31] D. E. Budil, K. L. Sale, K. A. Khairy, and P. G. Fajer, *J. Phys. Chem. A.* **110**, 3703 (2006).
- [32] M. Blume, *Phys. Rev.* **174**, 351 (1968).
- [33] R. Lenk, *Brownian Motion and Spin Relaxation* (Elsevier, 1977).
- [34] R. G. Gordon and T. Messenger, in *Electron Spin Relaxation in Liquids*, edited by L. T. Muus and P. W. Atkins (Plenum, 1972).
- [35] K. Itô and H.P. McKean *Diffusion Processes and Their Sample Paths*, (Springer, 1965).

- 
- [36] D. R. Brillinger, *J. Theor. Prob.* **10**, 429 (1997).
- [37] D. Sezer, J. H. Freed, and B. Roux, *J. Chem. Phys.* **128**, 165106 (2008).
- [38] L. D. Landau and E. M. Lifshitz, *Quantum Mechanics: Non-Relativistic Theory* (Pergamon Press, 1981).

## 5.2 Growth of Bimetallic Nanoparticles: Cu-Ni

### 5.2.1 Introduction

Controlling the morphology of nanosize metallic synthesis has become increasingly important on nanotechnology due to having diverse properties industrially acknowledged on many applications. With the adequate initial conditions implemented on the nano structure (forced configurational state), an environment in which the diffusion mechanisms (the diffusion in the solution and the surface diffusion on the nanocube) govern the formation of layers in the macrostructure can be maintained [1, 2]. Then, it becomes a much easier task for the experimenter to intervene kinetics of relaxation process in order to control the growth of bimetallic synthesis by tuning experimental parameters such as the temperature and injection rate of the additional atoms [2]. Controlled growth of bimetallic nanoparticles can be maintained by intervening kinetics of relaxation processes. Such an experimental framework [3, 4, 5, 6, 7] has recently become very common in controlling the layer formation on bimetallic nanocubes for a variety of synthesis. While the framework is established upon basic principles of thermodynamics, the atomic-scale details on non-equilibrium processes are still in ambiguity. It is therefore an appropriate task for molecular static and dynamic simulations to leak out the underlying atomistic mechanisms of the experimentally well-classified growth modes.

The present work provides an atomic scale analysis on Cu deposition on Cu nano cube (Cu-Cu), Ni deposition on Ni nano cube (Ni-Ni), Ni deposition on Cu nano cube (Cu-Ni), Cu deposition on Ni nano cube (Ni-Cu). In each case, the original nano cube is a single seed truncated cube in fcc structure having (111) facets on 8 corners and (100) facets on 6 sides. Starting from a constrained state where adatoms are projected to (111) facets, it is expected that the system evolves to the equilibrium state (minimum energy configuration) through diffusion when the constraint on the system is removed. In fact, this process is a non-equilibrium process which can be controlled by kinetics. Thus, we have carried out a detailed atomic scale analysis on relevant diffusion mechanisms and diffusion timescales

by utilizing the statistics obtained from single-atom diffusion simulations and calculated energetics of transition pathways. Among all types of synthesis, we have observed Ni-Cu synthesis to contain fastest diffusion processes. Using this analysis, we investigate the overall non-equilibrium phenomena for each type of synthesis (Cu-Cu, Ni-Ni, Cu-Ni, Ni-Cu) in two ways. In the first part, we consider an open system at a fixed temperature  $T=500$  K in which we impose inclusion of particles (adatoms) with a uniform frequency (injection rate) and an initial constraint over adsorption sites (only upon deposition), and observe growth modes of the system by varying injection rates. The entire process is highly sensitive on kinetics, i.e., competition between surface diffusion velocity  $v_{diff}$  and deposition velocity  $v_{dep}$  of the adatom, hence our statistical analysis on diffusion timescales is deemed to be a reliable guide. In the second part, we consider a closed system starting from a metastable state (octopod shape) in which the deposition process for Ni-Cu synthesis is held at  $T=300$  K. The system is then put into a thermal bath at fixed temperatures distinctly with  $T=300$  K and  $T=500$  K, in order to observe relaxation dynamics and timescales. Accordingly, we have observed a fast transition (about dozens of ns) to the equilibrium state at  $T=500$  K while having a very slow dynamics which prolongs the relaxation time to infinite simulation time (from ns to hours) at  $T=300$  K.

### 5.2.2 Computational Details

Our aim in this study is to compose a dynamic process which will simulate atomic deposition on a nano crystal with periodic ad atom injections in a solution at a fixed temperature. The experimental setup that we want to refer investigates atomic deposition on a fcc nano crystal containing (100) facets on 6 sides and (111) facets on 8 corners of which (100) facets are passivated and hence ad atoms are only deposited on (111) facets. In the experiments, growth modes are governed by the ratio of surface diffusion velocity  $v_{diff}$  to deposition velocity  $v_{dep}$  of the ad atom, as well as intrinsic characteristics of the interactions between the ad atom and the nano crystal [2, 3]



For that purpose, we first prepare a single seed nano crystal in a non-periodic computation cell. Then, we propose periodic single atom injection from 8 corners directed towards the center of (111) facets with a periodicity  $\Phi$  that is inversely proportional to the deposition velocity  $v_{dep}$ . Atomic deposition on single seed nano crystals is simulated by using LAMMPS Molecular Dynamics Simulator [8]. Initial cubic nano crystal is obtained using bulk fcc lattice coordinates of the associated seed type and has finite size with the length of 3.615 nm and 3.52 nm for Cu and Ni, respectively. The computational cells for both Cu and Ni contain the same number of atoms. Then a minimization process is applied on both nano crystals using LAMMPS through which the finite size and surface effects were directly implemented. MD simulations for the initial 4455 single type of atoms of the crystal structure are conducted after cutting the corners of the cube, thus forming the (111) facets at the corners (Fig. 5.9). In the heating process, temperature is increased by 50K at each 30 ps time interval using Nosé-Hoover thermostat [9, 10]. Deposition process is performed simultaneously from 8 corners with period of  $\Phi$ . In this paper, we have used 161x8 ad atoms in total for each simulation describing the entire process, to provide consistency for comparison. Throughout the deposition and relaxation processes, Nosé-Hoover thermostat maintained to fix the temperature at a constant level, that is in accordance with experimental setups in which the deposition on nano crystals is realized by periodic injections of ad atoms in a solution at a fixed temperature. For interatomic interactions, we have employed an optimized Embedded Atom Model (EAM) potential[11] that is determined by fitting to experimental and first-principles data (such as lattice constants, cohesive energies, bulk modulus, elastic constants, diatomic bond lengths and bond energies) for Cu, Ni and Cu-Ni binary structures [12]. For most frequently occurring events, the energy barriers and surface adsorption energies are calculated using Nudged Elastic Band (NEB) method[13, 14].

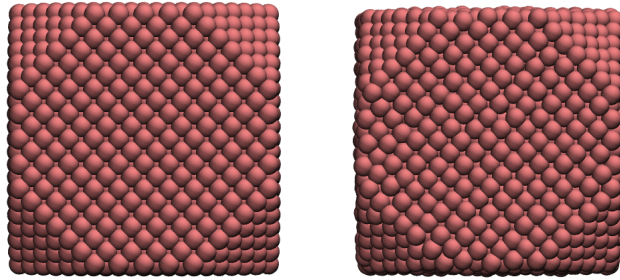


Figure 5.9: Cu nanocrystal with (111) facets at  $T=0$  K (on the left) and  $T=500$  K (on the right). Ad atom deposition are directed to the center of (111) surfaces. Same structure is utilized for Ni nano crystals with the respective lattice constant. Computational cells are non-periodic so that the entire nano cluster is standing in an isolated environment.

### 5.2.3 Results

#### Statistics

The growth modes of metallic synthesis depend on the competition between average diffusion times of ad atoms and average injection periods which in our study is uniform and referred as  $\Phi$ . The required average diffusion time  $\langle t_{diff} \rangle$  to have a valuable comparison, is basically a combination of average diffusion time of ad atoms from (111) to (100) facets  $\langle t_{diff}^{(111) \rightarrow (100)} \rangle$ , and average diffusion time on (100) facets which contains more complex mechanisms than the former and can be better understood by thermodynamics. As a first step, single-atom diffusion statistics at a specific temperature can be used for determining  $\langle t_{diff}^{(111) \rightarrow (100)} \rangle$  and the most dominant diffusion mechanisms to (100) facets. For that purpose, we have first extracted frequent diffusion schemes from simulation of ongoing deposition processes (with hundreds of adatoms) at  $T=500$  K which shows similarity for Cu-Cu, Ni-Ni and Cu-Ni synthesis while exhibiting completely different scheme for Ni-Cu synthesis.

The statistics on single-atom diffusion are obtained using 15 independent simulations for 8 ad atoms (120 atoms in total, see details in Supporting Information) sent for once (1x8) simultaneously to the 8 corners of original cubic nano seed at  $T=500$  K. Although, each simulation exhibits distinct atomic trajectories, they

have some common characteristics for diffusion mechanisms and thus we have prepared the related statistics which are essentially defining the basic features of diffusions to (100) facets in the simulation of atomic deposition with much larger amount of injected atoms such as deposition with (161x8) ad atoms in part "Growth Modes". From our observations, we have found that exchange is the only mechanism that is responsible for mass transport to (100) facets. In Fig. 5.10, we show possible exchange mechanisms to (100) facets, and their occurrence probabilities among all exchange events which shows varying characteristics for different types of synthesis, i.e., Cu-Cu, Ni-Ni, Cu-Ni. Nonetheless, for all three of them, we observe that exchange through site C is the mostly frequent event. Diffusion through corner site A is not observed for any of these cases. The closest fcc site to the corner site A is marked as site 5 (colored in red) in Table 5.3, and it is next nearest neighbor for site A while it is nearest neighbor for site B so that diffusion through site B is much more favorable. However, when (110) channels are formed on the 12 edges, diffusion to these channels through site 5 has been observed experimentally [2], and also confirmed computationally with hopping as the dominant diffusion mechanism [15]. In this study, we have run the simulations only on the cubic systems with no (110) channels at the edges, yet we observe that these channels can be formed at significant simulation time, about dozens of nanoseconds, as the atoms on the edges are the least coordinated ones. However, its effects on diffusion processes are negligible since most of the growth process are completed before formation of the edge channels. The diffusion mechanism for Ni-Cu synthesis with the given geometry in Fig. 5.10 is observed to be very slow in comparison to other synthesis. However, our simulations of Cu deposition on Ni nano cube (see Growth Modes) result in a fully covered nano structure, more rapidly than any other system. This fact implies that another type of diffusion mechanism should be dominant for Ni-Cu synthesis. In kinetic view, due to high activation energy barriers for Cu atoms to diffuse (100) facets of Ni seed, deposited Cu atoms accumulate on (111) facets in fcc stacking. With the addition of new (111) Cu layer on Ni nano crystal, activation energy barriers for ad atoms to diffuse on neighboring facets drop significantly as seen in Table 5.5, and provide much easier exchange through (100) facets. To illustrate the issue in

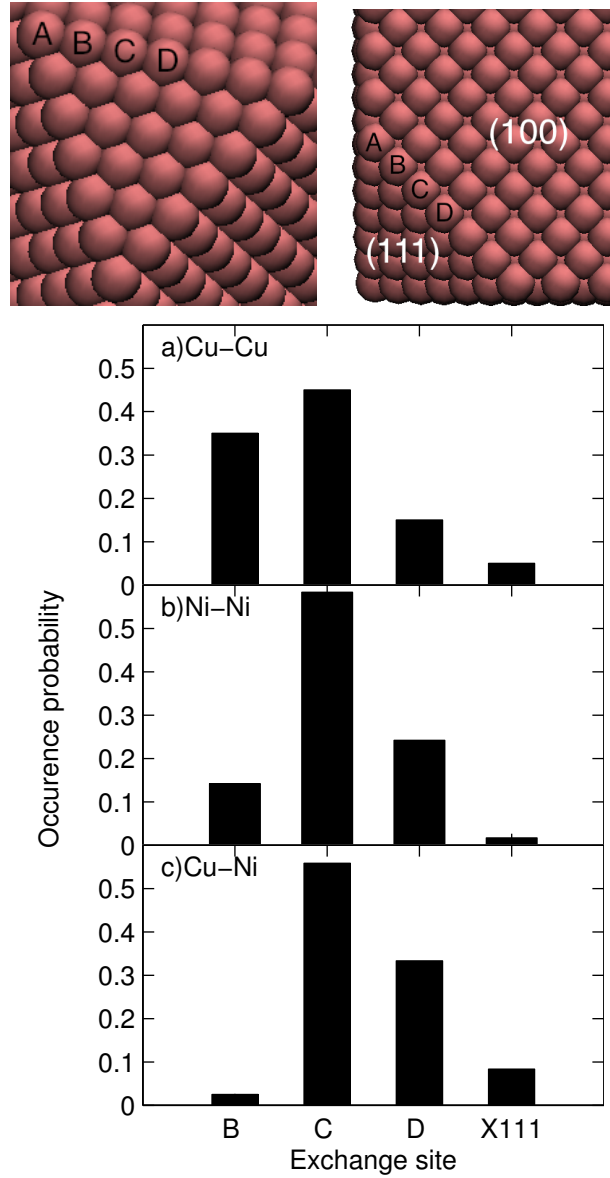


Figure 5.10: Occurrence probabilities of exchange to (100) surfaces through sites B,C,D. Exchange to (111) facets are noted as X111 for different types of synthesis. For all three systems, while exchange through site C is the dominant mechanism, exchange through site A does not appear. The average diffusion times for all the exchange events from (111) to (100) facets  $\langle t_{diff}^{(111) \rightarrow (100)} \rangle$  are found to be a) 99.2 ps, b) 187.1 ps, c) 43.4 ps. for Cu-Cu, Ni-Ni, Cu-Ni systems, respectively. For Ni-Cu synthesis, the dominant diffusion mechanism is observed to be quite different and represented in detail in Fig. 5.11.

detail, we performed statistical calculations for the case in which the original nano cube is considered to be Ni nano cube of which the (111) facets are covered with Cu atoms in fcc stacking. We deposit Cu ad atoms again on Ni nano seed that has a layer of Cu on its corner facets and observe diffusion mechanisms. In Fig.

5.11, we show the statistics for all possible diffusion mechanisms. As seen in the previous cases, we do not observe any exchange through the corner site E of the Cu covered (111) facets. On the other hand, the significant increase on the rate of exchanges on (111) facets points a new favorable mechanism for Cu ad atoms. In all exchange events, at least one Cu atom from (111) facet join to Ni (100) facets via exchange or jumping with the push of the ad atom. Here, jumping is defined as a dynamic process in which the initial position being on Cu (111) and neighboring with Ni(100) such as sites E,F,G, and final position being on top of Ni(100). Including all diffusion events of ad atoms, we have observed that these events yield to exchange of another atom with 16% and jumping of another atom with 84% occurrence.

Regarding most frequent exchange events, we have also calculated average diffusion time for all synthesis types and found  $\langle t_{diff}^{(111) \rightarrow (100)} \rangle$  to be 99.2 ps for Cu-Cu, 187.1 ps for Ni-Ni, 43.4 ps for Cu-Ni, and 16 ps for Ni-Cu. To acquire the structure in Fig. 5.11 for Ni-Cu synthesis, a constant time depending on injection period should pass in order to accumulate enough number of atoms to form Cu(111) facets. However, this is a standard procedure happening for all range of deposition rates, thus we may easily claim that the easiest diffusion from (100) to (111) facets will be for Ni-Cu synthesis.

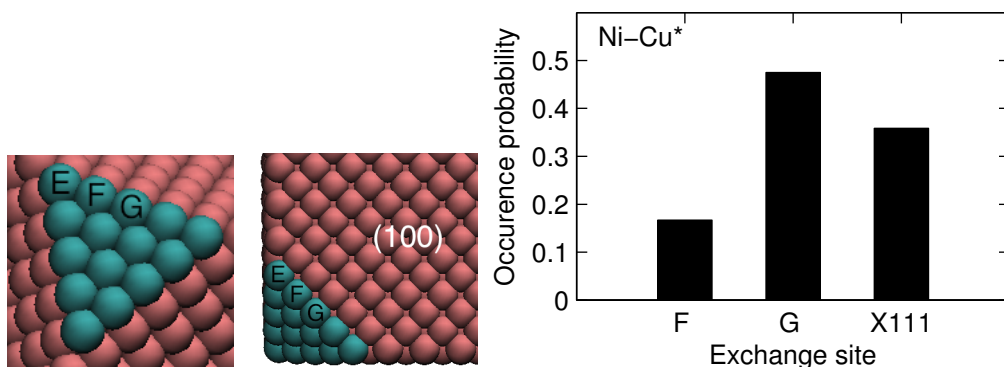


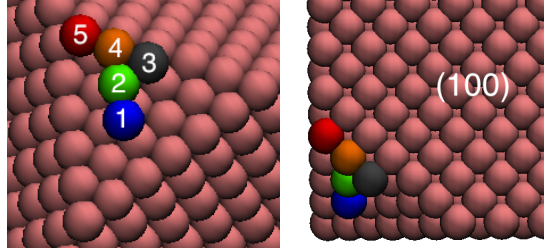
Figure 5.11: On the left, the original structure that is prepared with a truncated Ni cube with a layer of Cu atoms in fcc stacking on (111) facets. On the right, occurrence probabilities of exchange to (100) surfaces through sites F,G. Exchange to (111) facets are noted as X111. On this system, exchange through corner site E does not occur and the average diffusion time for all exchange events from (111) to (100) facets,  $\langle t_{diff}^{(111) \rightarrow (100)} \rangle$ , significantly decreased: 16 ps.

Finally, our further observations on the diffusion of second ad atom deposited right after all first (1x8) atoms had diffused is more or less resulting in the same diffusion timescales. On the other hand, if the second ad atom is sent before the first ad atom on the corner facet succeeds to diffuse to (100) facet, the diffusion times for each atom prolonge significantly, at least increased by a factor of 10, since these two free atoms bond together. In other words, if the deposition period is chosen higher than the average diffusion time we may expect to have a uniform diffusion process, while if it is lower than the diffusion timescales in the upcoming depositions can extend due to clustering. Hence, we may conclude that single-atom diffusion timescales of the first ad atom provides the characteristic timescales to control growth modes. Nevertheless, the actual characteristic timescale to control growth modes is a combination of exchange diffusion time and mobility of ad atom on (100) surface.

### **Energetics and Mechanics**

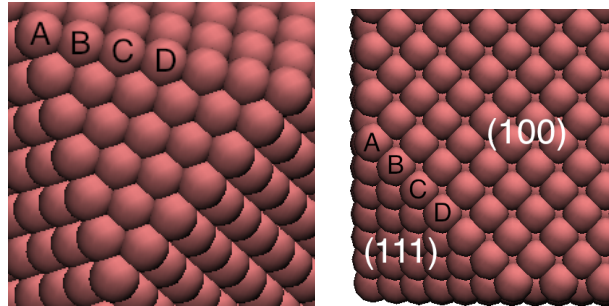
The statistics that we obtained for diffusion events and diffusion times are providing much of the information about dynamic processes responsible for diverse growth modes. In order to better understand these processes, we have also studied the energetics and mechanics of the governing diffusion events. Likelihood of diffusion events depends on vibrations of crystal atoms, adsorption energies on (111) facets and on activation energy barriers of the diffusion processes. Adsorption energies for several fcc sites (which define all possible adsorption sites) on (111) facet are shown in Table 5.3. When there is thermal energy introduced to the system, we would expect that occupancy rates of the adsorption sites to be directly related to the adsorption energies, meaning that the lower energy, i.e., higher adsorption energy sites would be more preferable than higher energy, i.e., lower adsorption energy sites. Activation energy barriers calculated at  $T=0$  K (Table 5.4), determine the energy cost of the system to make the corresponding action. However, likelihood of the type of action is not just determined by adsorption rates or energy barriers but also by effective coordination of the atoms participating in action. In other words, collective motions would be more likely to happen since workload on each atom would be less. Hence, one should interpret the statistics of the events

regarding all of these issues.



Adsorption site	5	4	3
Cu/Cu(111)	-0.120	-0.059	-0.070
Ni/Cu(111)	-0.195	-	-
Ni/Ni(111)	-0.304	-	-0.153
Cu/Ni(111)	-0.179	-0.086	-0.096

Table 5.3: Energetics of adsorption (in eV) on the corner of nanocrystal, i.e., (111) facet, with main sites of adsorption (fcc) shown as 5,4,3 and the rest can be attained by symmetry. All values are normalized by subtracting the highest adsorption energy value of sites 1 and 2 (1 and 2 are symmetric sites).



Exchange site	B	C	D
Cu/Cu(111)	0.161	0.358	0.343
Ni/Cu(111)	0.078	0.335 *	0.300 *
Ni/Ni(111)	0.121	0.460 *	0.372
Cu/Ni(111)	0.258	0.539	0.527

Table 5.4: Calculated activation energy barriers (in eV) on the corner of nanocrystal and at the intersection of (111) and (100) facets with main exchange sites shown as B, C, D and the rest can be attained by symmetry. All of the diffusive motion of ad atoms are estimated to start from the closest fcc site available to each B, C, D while for ones with asterisk, minimization of the initial configuration led the ad atom to hop to the hcp site below since there is no barrier between two configurations (for further explanation, see Supporting Information).

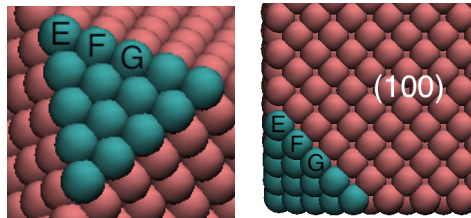
Supposing that the target surface (111) is flat with very low ionic vibrations and the energy barriers between adsorption sites are achievable so that the ad atom

is considered to be freely diffusing on the surface (111), the probability of being at adsorption site  $\gamma$  can be roughly determined from the equilibrium distribution, i.e.,  $p_\gamma \propto e^{\epsilon_{ads}/k_B T}$ . Arrhenius equation, on the other hand, suggests that transition rate  $k$  in general can be determined from

$$k = A e^{-E_q/k_B T} \quad (5.32)$$

where  $A$  is the attempt frequency which is equivalent to occupancy rates  $p_\gamma$  in our case and  $E_q$  is the activation energy barrier per atom. With increasing collectivity of atoms to accomplish an action, work load on each atom  $E_q$ , drops roughly as  $\sim 1/q$ , where  $q$  is the number of participating atoms, making the action more likely. Another factor that determines characteristics of diffusing atoms on surfaces is the attempt frequencies that are directly related to the occupancy rates  $p_\gamma \propto e^{\epsilon_{ads}/k_B T}$ . That helps us understand why diffusion on Cu-Cu synthesis is quicker than on Ni-Ni synthesis while activation energy barriers are very similar.

In Table 5.5, we present the calculated activation energy barriers for the regarding diffusion processes in Ni-Cu synthesis. For these calculations, the computational cell is constructed as shown in Fig. 5.11. It is clearly seen that the barriers are dropped significantly when the (111) facets of Ni nano cube are fully covered by Cu atoms (by accumulation of Cu atoms), and hence it becomes much easier for Cu atoms to complete the diffusion process hand in hand.



Exchange site	F	G	X111
Cu/Ni(111)	0.211 (0.539)	0.257 (0.527)	0.387

Table 5.5: Calculated activation energy barriers (in eV) on the corner of Ni nanocrystal when its (111) facets are covered by a monolayer of Cu. Exchange with an atom on (111) facet is denoted by X111. When compared to the values in Table 5.5, presented in brackets for C and D, it is easily seen that the barriers are dropped significantly, which would ease the diffusion to (100) surface.



### Growth modes

So far we have investigated the governing diffusion mechanism based on atomic level event by event analysis for all synthesis at  $T=500$  K. While our results on previous sections provide us timescales of diffusion events in detail, in this section we will be focusing on controlling growth modes by changing injection period  $\Phi$ . Simulations will be carried out at  $T=500$  K on an idealized system in which the deposition of ad atoms takes place from 8 corners of the cube simultaneously and uniform in time. Indeed, in experimental studies, surface diffusion speed is controlled by temperature, i.e.,  $v_{diff} \equiv v_{diff}(T)$  and deposition period is not identical to the injection rate of the solution which contains the ad atoms and is generally dependent on the temperature and the amount of solution introduced per unit time i.e.,  $\Phi \equiv \Phi(T, n)$  where  $n$  is the amount of ad atom solution introduced per unit time.

### Homogenous growth

In this section, we will exhibit our results for the simulations in which the deposited ad atom is of the same type with the target nano crystal. Thus, simulations are done separately for Cu deposition on Cu nano crystal and Ni deposition on Ni nano crystal.

The growth modes of Cu nano cluster are shown in Fig. 5.12. For higher deposition rates, i.e., lower injection periods, we obtain an octopod shape. For lower deposition rate, i.e., higher injection period such as  $\Phi=500$  ps, deposited Cu atoms diffuse to different facets, and forming a truncated cube with nearly flat surfaces in collaboration with the cubic seed Cu atoms as displayed in Fig. 5.12(c). Same growth modes, are also found for Ni deposition on Ni nano crystal (data not shown). Furthermore our results show that covering the surface for Cu-Cu synthesis happens for slower deposition periods than Ni-Ni synthesis, as indicated by our analysis on average diffusion times in "Statistics". Previous study on Ag deposition on Ag nano seed [15], and experimental results for Pt deposition on Pt, and Pd deposition on Pd nano crystals [3] show similar morphologies for diverse growth modes. The extensive study on atomic scale analysis of Ag deposition on

Ag truncated nano cubes via MD simulations [15], also presents the cooperativeness of ad atoms and cubic seed atoms when forming the surface of the nano cube in a single type synthesis. Using all these facts, we may argue a universality for the behavior of homogenous deposition processes, while other single type metallic synthesis should confirm our results.

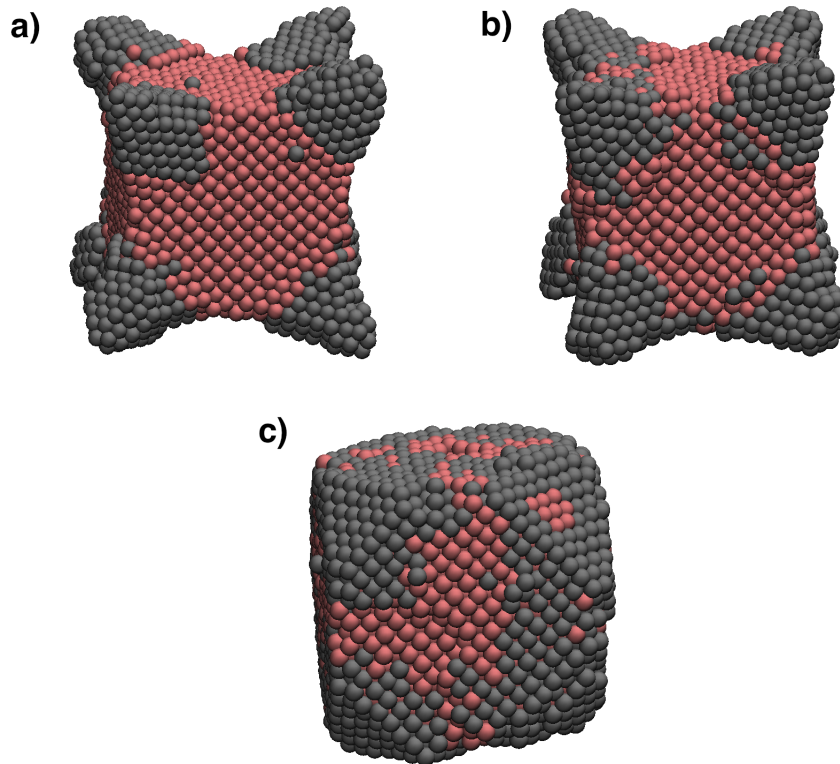


Figure 5.12: Cu deposition on Cu nanocrystal with injection period a)  $\Phi=10$  ps b)  $\Phi=100$  ps c)  $\Phi=500$  ps at  $T=500$  K. Similar growth modes are obtained for Ni deposition on Ni nanocrystals (data not shown).

### Heterogenous growth

In this section, we will exhibit our results for the simulations in which the deposited ad atom is not the same type with the target nano crystal. Thus, simulations are done separately for Ni deposition on Cu nano crystal and Cu deposition on Ni nano crystal. We obtain very different characteristics and growth modes distinctly for Ni-Cu and Cu-Ni synthesis unlike the universality that we observed in homogenous case. Since there are two type of species we will encounter a competition between

these atoms for surface formation resulting in different thermodynamic processes. Previous analysis show that the formation energy for Cu (100) and Cu (111) surfaces are lower than, respectively, Ni (100) and Ni (111) for infinitely large systems. Therefore, we may expect Cu clusters to try covering the surface of the Ni nano crystal. Deposition of Cu atoms on Ni nano crystal confirms this idea, and thus we obtain a fully Cu covered Ni nano crystal (Fig. 5.13).

In Fig. 5.13, we have results for Cu deposition on Ni nano crystal, and see two distinct growth modes one being octopod when the injection period  $\Phi=10$  ps and other being fully covered nano structure when  $\Phi=100$  ps. For lower injection period, i.e., high deposition rate ( $\Phi=10$  ps), the ad atoms do not have enough time to diffuse on (100) facets, and thus they will accumulate on (111) facets and form a cluster which is being in pyramid shape. However, for higher injection period such as  $\Phi=100$  ps, there is enough time for diffusions to take place and thus a fully covered nano structure is obtained.

With a tentative overview, we see a close relationship between relative ratio of injection period  $\Phi$  and average diffusion times obtained from single-atom diffusion statistics on formation of distinct growth modes in Cu-Cu, Ni-Ni and Ni-Cu synthesis: for all cases an equilibrium state (fully covered nano cube) is nearly maintained for the injection periods higher than the average diffusion times. The corresponding injection periods also show agreement with the hierarchy that we provide in the most previous part of this subsection for diffusion times, i.e.,

$$t_{diff}^{Ni-Ni} > t_{diff}^{Cu-Cu} > t_{diff}^{Ni-Cu*}.$$

In Fig. 5.14, we have results for Ni deposition on Cu nano crystal, which imply an asymmetric shape formation due to lack of order caused by competition between Ni and Cu clusters to form surface. Surface formation energy of Cu atoms are lower than Ni atoms, hence Cu atoms are trying to engulf big Ni islands. Thus, in fact, the equilibrium product does not suggest a Ni covered Cu nanocrystals. When the deposition rate is high (i.e.,  $v_{dep}$  is high and  $\Phi$  is low) it becomes harder for Cu atoms of the seed to keep their surface positions due to faster accumulation of Ni atoms on the surface. At the end, this may cause non-equilibrium processes to be dominant, leading to a high competition between Cu and Ni clusters, thus asymmetric shape formations.

From kinetic point of view, we can comment on these dramatically different characteristics of Ni-Cu and Cu-Ni synthesis as follows: From our statistics obtained for dominant exchange mechanisms for Cu-Ni (Fig. 5.10) and Ni-Cu (Fig. 5.11), the diffusion times are relatively shorter than homogenous synthesis. Therefore, we expect quickly occurring exchange events from (111) to (100) facets for both cases. However, as we pointed out in the previous subsections, following the diffusion to (100) facets, the rate of diffusion on (100) facets gain much importance in order to prevent accumulation on corners of the cube. The previous results on diffusion energy barriers for diffusion mechanisms for Cu, Ni synthesis show that exchange on Cu(100) surface is more preferable than hopping on Cu(100) for Ni ad atoms, while we have completely reverse scenario for Cu ad atoms on Ni(100) surfaces [12, 16]. As a result, Ni atoms reaching Cu(100) facets would not prefer to move on the surface via hopping and thus would accumulate. On the other hand, Cu atoms reaching Ni(100) facets may move on the surface much easily and form a surface layer. Notice that the energy barriers that we refer are for infinitely large surfaces and we expect to keep the same hierarchy for nano level (100) facets. In addition, our result for activation energy barriers for hopping of Cu atoms on Ni(100) facet distinctly calculated for different sites whose locations are ranging from edge to center, shows that the energy value is quickly converging to the infinitely large case value when we get closer to the center of (100) facet.

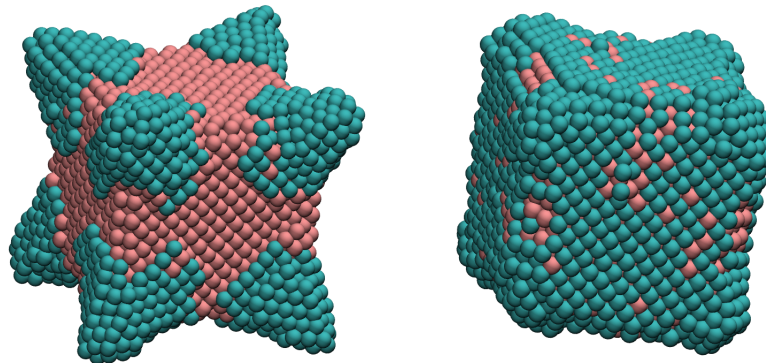


Figure 5.13: Cu deposition on Ni nanocrystal with injection period  $\Phi=10$  ps (on the left) and  $\Phi=100$  ps (on the right) at  $T=500$  K. Two distinct growth modes i.e., octopod (on the left) and fully covered cubic shape (on the right) are obtained.

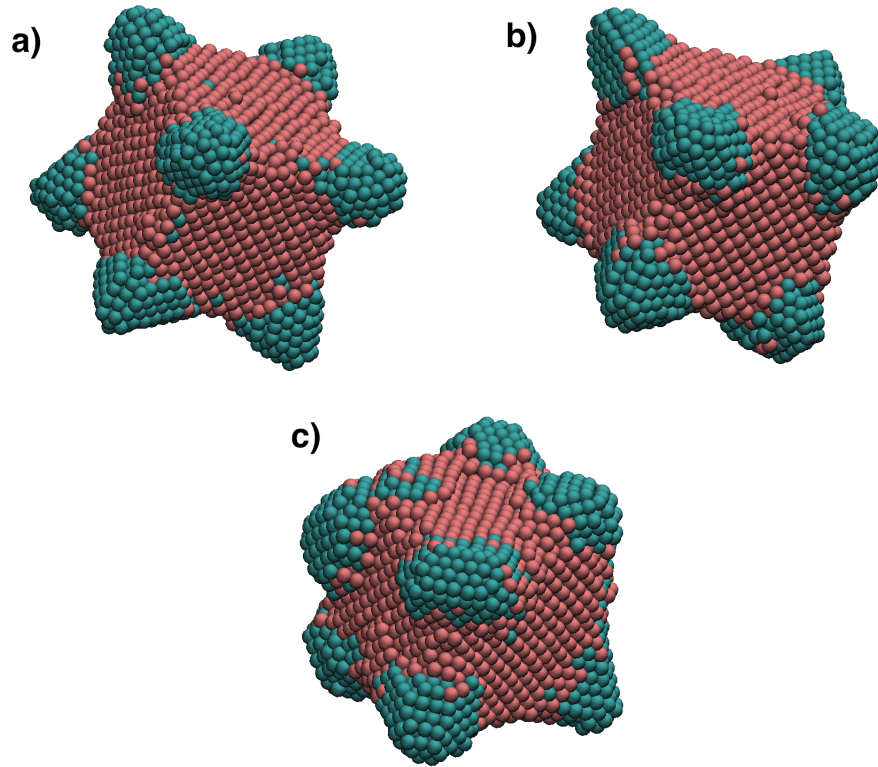


Figure 5.14: Ni deposition on Cu nanocrystal with injection period a)  $\Phi=10$  ps b)  $\Phi=100$  ps c)  $\Phi=250$  ps at  $T=500$  K.

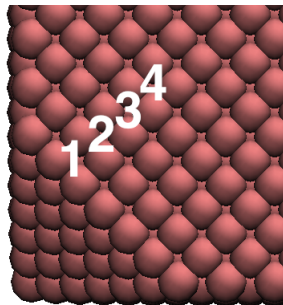
#### 5.2.4 Relaxation of non-equilibrium nanostructure

Finally, non-equilibrium nature of atomic vibrations lead to transition between steady states. Thus, we have also investigated what would happen when we leave the nano structure in a thermal bath for some time following the deposition process. To allow computationally reachable timescales, we consider the fastest diffusing synthesis, i.e. Ni-Cu, in which we have a Ni nano crystal and initially performed Cu deposition with  $161 \times 8$  ad atoms as always but now at  $T=300$  K. We would expect system to evolve to a stable state, i.e., steady state at the given temperature. From thermodynamical point of view, in order to have a transition between diverse morphologies, kinetic process should start initially from octopod shape to fully covered nano structure for which the reverse is not possible. For that purpose, we prepare the deposited crystal as an octopod, thus use a deposition period  $\Phi=10$  ps at  $T=300$  K. Inclusion of thermal energy is very crucial to push

the system out of a metastable state since ad atoms need enough kinetic energy to pass activation energy barriers for diffusion processes.

First, we consider the case where we add thermal energy to the initial octopod (Ni-Cu) structure by heating crystal until it reaches  $T=500$  K, and then leave it for relaxation. As shown in Fig. 5.15, we observe a dynamic transition from octopod shape to concave one and finally to fully covered original-like structure. The transition is induced by increasing the temperature and providing a notable relaxation time to the system without the deposition of any ad atom.

Secondly, we check the evolution of the initial octopod crystal through some relaxation time without adding thermal energy, at  $T=300$  K. In this case, we observe very few significant change even at atomistic level as is seen in Fig. 5.16. As a result, it seems that we would need infinite simulation time, i.e., from ns to hours, to observe macro changes (if possible) in the nano structure. However, real experiments can test this at room temperature, and check whether it is a stable state or not. For this situation, our further analysis on hopping mechanism of Cu atoms on Ni (100) facets, suggests that shape transformation is very unlikely at  $T=300$  K. High activation energy barriers for hopping of the atoms diffused on (100) through exchange, and very low vibrations of crystal atoms, make hopping mechanism harder to occur. Table 5.6, shows activation energy barriers for diffusion on Ni(100) facets for Cu atoms.



Hopping from	$1 \rightarrow 2$	$2 \rightarrow 3$	$3 \rightarrow 4$
Cu/Ni(100)	0.358	0.425	0.426

Table 5.6: Calculated activation energy barriers (in eV) for hopping of Cu atoms on Ni(100) surface for nano crystal. The barrier is minimum when the motion is on the edges and increases when it is close to the center of (100) facet.

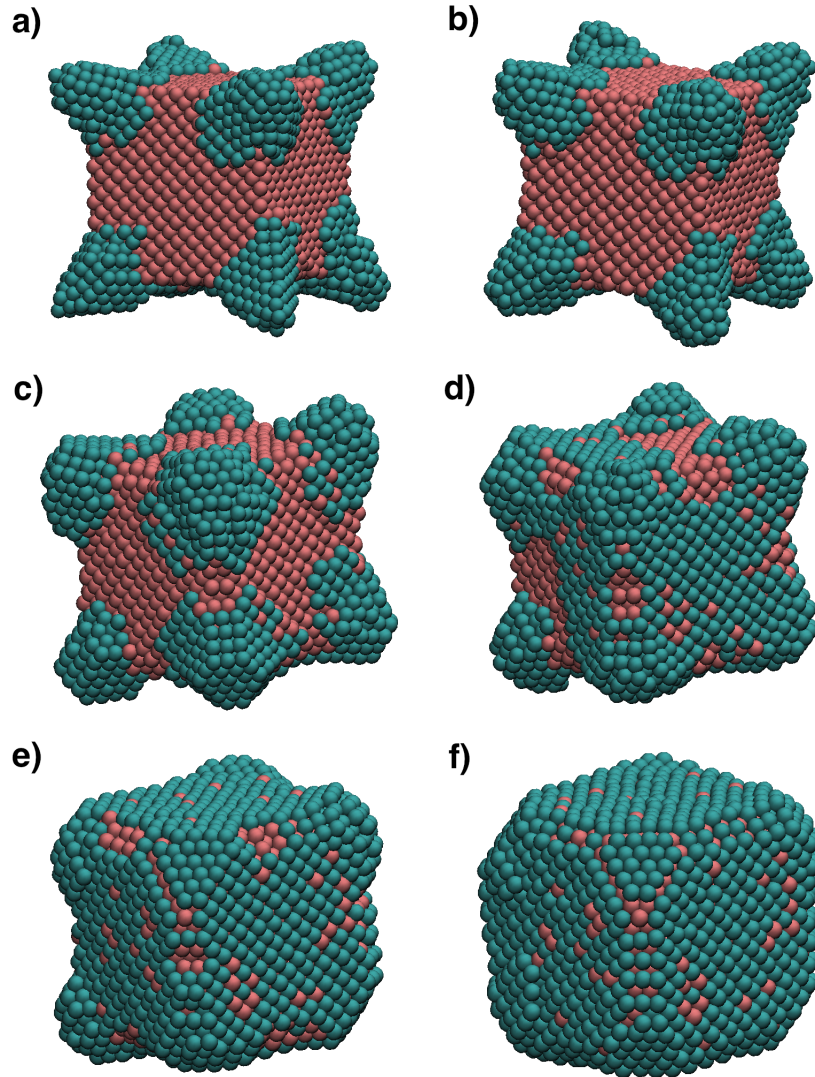


Figure 5.15: Dynamic transition from octopus shape to concave one and finally to fully covered original-like structure for Cu deposited Ni nano crystals. Deposition process is held at  $T=300$  K with  $161 \times 8$  ad atoms with injection period of  $\Phi=10$  ps. At the end of deposition process system is heated until  $T=500$  K, and then we have observed relaxation process in some significant time at  $T=500$  K. Snapshots represent the state respectively for a) end of deposition process at  $T=300$  K, b) end of increasing temperature until  $T=500$  K, and setting relaxation time on thermal bath as  $t_{bath}=0$  ns, then after relaxation on thermal bath with  $T=500$  K, c)  $t_{bath}=8.4$  ns, d)  $t_{bath}=20$  ns, e)  $t_{bath}=37.5$  ns, f)  $t_{bath}=77.5$  ns.

### 5.2.5 Conclusion

In this study, growth modes of nano crystals with synthesis of Cu-Cu, Ni-Ni, Cu-Ni, and Ni-Cu are investigated using molecular dynamics simulations and energetic calculations. Our results confirm results of the related experiments on the role of

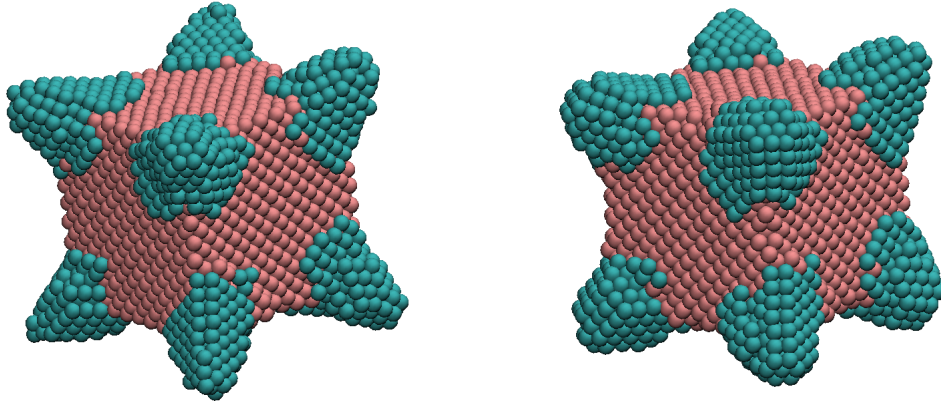


Figure 5.16: Relaxation at  $T=300$  K: right after deposition process (on the left) and after 180 ns (on right). Changes are seen on the tip of octopod while the atoms on the (100) facets are barely moved.

internal characteristics in determining the shape of the nano structure. From MD simulation of atomic deposition with different injection rates, we have observed that fastest diffusion process is occurring for Cu deposition on Ni nano crystals, i.e., Ni-Cu synthesis. In addition, statistical characteristics of repeated single-atom diffusions as well as calculated adsorption energies and activation energy barriers for most frequent diffusion events, maintain a new scope on observing atomic-scale diffusion processes and their direct relation with macro level shape formations. At macro level, distinct shape formations, dynamic transitions, and steady states are carefully observed and characterized. Dynamic transitions between steady states at  $T=500$  K, may imply more control over growth while transitions are almost impossible at low temperatures showing a trapped state for the nano structure.

## 5.2.6 Supporting Information

### Analysis of statistics

As discussed in detail in Section 5.2.3, statistics obtained from repeated single-atom diffusion simulations provide a microscale analysis on most dominant diffusion events and their occurrence probabilities (Figs. 5.10-11). In addition to that, including all types of exchange events we have observed average diffusion time from (111) to (100) facets  $\langle t_{diff}^{(111) \rightarrow (100)} \rangle$ . In order to obtain relevant statistics in



Section 5.2.3, one has to optimize number of samples for statistical accuracy.

In Fig. 5.17, we see how the average diffusion times and the standard deviations when increasing the number of simulations. As a result, obtaining a value in a 10% range of the estimated value is enough for our purposes, so that we may conclude to have an average diffusion time for Cu-Cu synthesis in 90 – 100ps range.

What interests us besides the average diffusion times of each synthesis is their relative ratios.  $\langle t_{diff}^{(111) \rightarrow (100)} \rangle$  has the hierarchy for homogeneous synthesis as  $t_{diff}^{Ni-Ni} > t_{diff}^{Cu-Cu}$  and for heterogeneous synthesis as  $t_{diff}^{Ni-Cu} > t_{diff}^{Cu-Ni}$ . However, our careful analysis on dominant diffusion mechanism for Ni-Cu synthesis showed us that diffusion on Ni-Cu synthesis becomes much more easier once (111) facets of Ni nano cube is covered by Cu atoms (referred as Ni-Cu\*), and it then has the smallest  $t_{diff}$  value among all four types of synthesis.

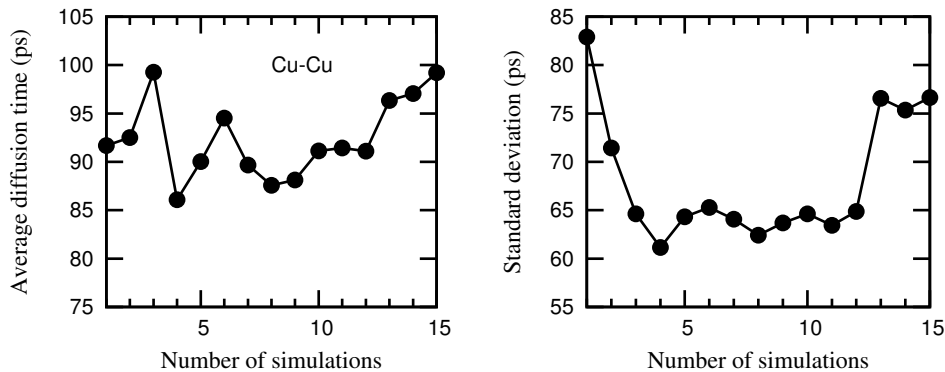


Figure 5.17: Average diffusion times and standard deviations as a function of number of simulations.

In addition to the average diffusion times, we also observed how these diffusion events are fulfilling a cumulative distribution. In Fig. 5.18, we show the number of diffused atoms normalized by total number of observed atoms, or ratio of diffused atoms  $n_{diff} = N_{diff}/N_{tot}$  as a function of time where  $N_{tot} = 120$  in our single-atom diffusion statistics.

### Energy barrier calculation

Thermodynamics suggests that at equilibrium the nano cube should be structured in a way that it minimizes the total free energy. However, in our simulations there

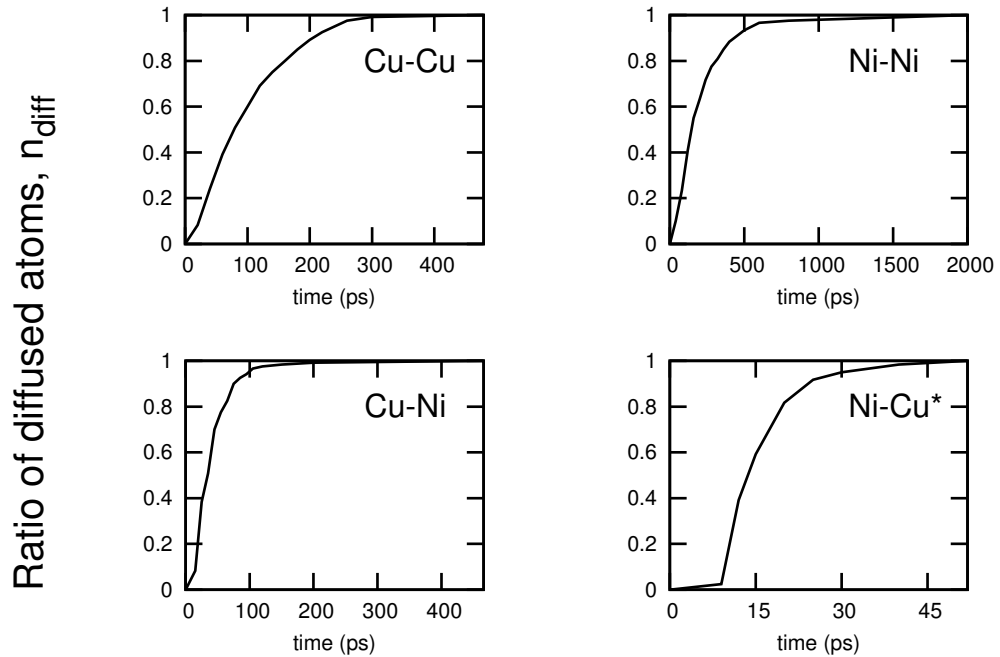


Figure 5.18: Cumulative distribution of ratio of diffused atoms as a function of time.

is a constraint on ad atoms during deposition which forces the atoms to target on (111) surfaces. So, once the ad atoms land on the corner facets, the atoms should perform a dynamic process, i.e. diffuse to (100) facets to reach a global minimum on the energy landscape, starting from a local minimum point. Thus, kinetics will gain much importance since the ad atoms generally should overcome an energy barrier to move on to the other minima. An example of energy landscape for several configurations is shown in Fig. 5.19. If  $d$  is given as global minimum for all cases, then the system is expected to evolve towards point  $d$ , starting from configuration  $b$ , and passing the energy barriers along the path. Unless enough thermal energy introduced to the system, it would not be able to overcome the energy barriers to reach the equilibrium point  $d$ , and thus stay at around a local minimum.

In Section 5.2.3, we have calculated activation energy barriers at  $T=0$  K using NEB method. For that purpose, we have selected the initial position of atom to be on nearest neighbor fcc site of target position (see figures in Tables 5.4 and 5.5

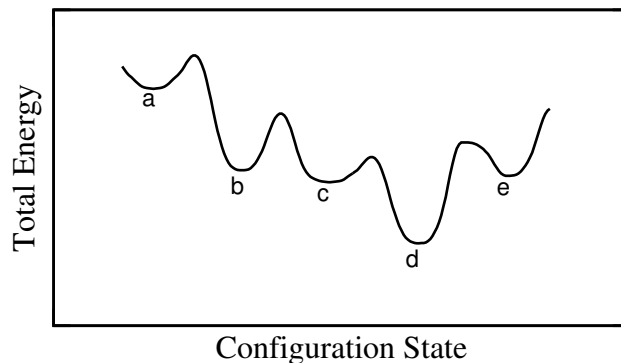


Figure 5.19: An example of energy landscape for several atom positions. Stable configurations are noted as a,b,c,d,e.

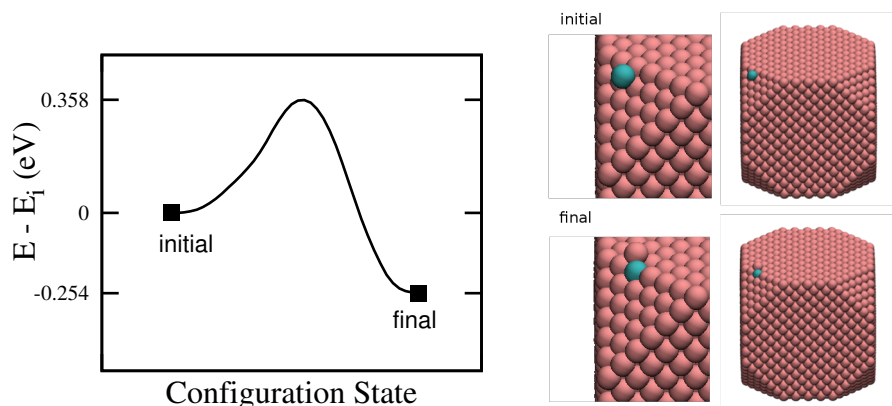


Figure 5.20: Optimized energy path of a kinetic process in Cu-Cu synthesis and specified by the initial and final configurations on the right.

for target sites), and the final position of pushed atom to be on closest minimum energy site on the top of (100) facet. We show these configurations in Fig. 5.20 along with the calculated energy path for exchange mechanism on site C in Cu-Cu synthesis. As clearly seen in the figure, the total energy of final configuration in which an extra atom is on (100) facet instead of (111) facet, is lower than the energy of initial configuration.

In Fig. 5.21 we plotted the energy path for an exchange mechanism on site C again in Ni-Ni synthesis. The process is specified by the same same configuration of the above initial and final positions but minimization of energy of the initial configuration forces the ad atom to start on hcp site below. The reason becomes clear once the energy landscape is investigated. The closest fcc site from target

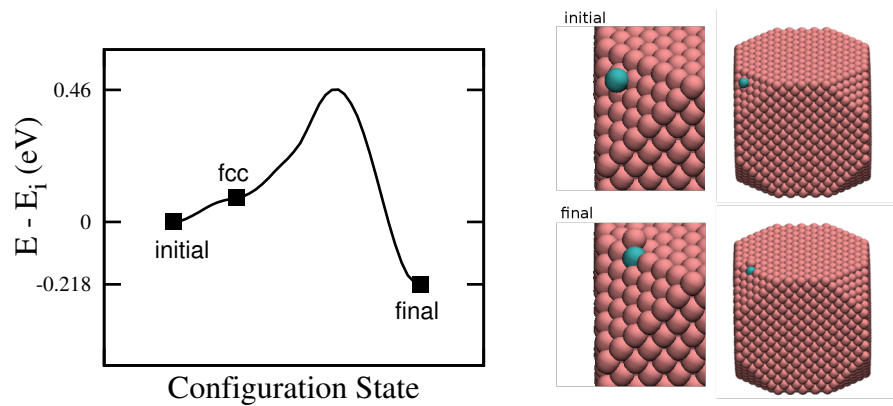


Figure 5.21: Optimized energy path for a kinetic process in Ni-Ni synthesis and specified by the initial and final configurations on the right. In this case, initial configuration is forced to be hcp by the instability of the presumed fcc site.

site C is not a stable configuration, and minimization pushes the atom on more stable location.

## REFERENCES

- [1] B. Lim, M. Jiang, J. Tao, P. H. C. Camargo, Y. Zhu, and Y. Xia, *Adv. Funct. Mater.* **19**, 189 (2009).
- [2] Y. Xia, X. Xia, and H.-C. Peng, *J. Am. Chem. Soc.* **137**, 7947 (2015).
- [3] X. Xia, S. Xie, M. Liu, H.-C. Peng, N. Lu, J. Wang, M. J. Kim, and Y. Xia, *Proc. Natl. Acad. Sci. U.S.A.* **110**, 6669 (2013).
- [4] S. Xie, S.-I. Choi, N. Lu, L. T. Roling, J. A. Herron, L. Zhang, J. Park, J. Wang, M. J. Kim, Z. Xie, M. Mavrikakis, and Y. Xia, *Nano Lett.* **14**, 3570 (2014).
- [5] H. Zhang, W. Li, M. Jin, J. Zeng, T. Yu, D. Yang, and Y. Xia, *Nano Lett.* **11**, 898 (2011).
- [6] X. Xia, L. Figueroa-Cosme, J. Tao, H.-C. Peng, G. Niu, Y. Zhu, and Y. Xia, *J. Am. Chem. Soc.* **136**, 10878 (2014).
- [7] Y. Wang, D. Wan, S. Xie, X. Xia, C.Z. Huang, and Y. Xia, *ACS Nano* **7**, 4586 (2013).
- [8] LAMMPS 2011 <http://lammps.sandia.gov>, S. Plimpton, *J. Comp. Phys.*, **117**, 1 (1995).
- [9] S. Nosé, *J. Chem. Phys.* **81**, 511 (1984).
- [10] W.G. Hoover, *Phys. Rev. A* **31**, 1695 (1985).
- [11] M. S. Daw and M. I. Baskes, *Phys. Rev. B* **29**, 6443 (1984).
- [12] B. Onat and S. Durukanoglu, *J. Phys.: Condens. Matter* **26**, 035404 (2014).
- [13] G. Mills, H. Jonsson, *Phys. Rev Lett.* **72**, 1124 (1994).
- [14] G. Mills, H. Jonsson, G. Schater, *Surf. Sci.* **324**, 305 (1995).
- [15] M. Konuk and S. Durukanoglu, preprint (2015).
- [16] G. Antczak and G. Ehrlich *Surface Diffusion: Metals, Metal Atoms, and Clusters* (Cambridge University Press, 2010).

Chapter 6

**CONCLUSION**

In conclusion, a rich variety of spin-glass systems is introduced by differing microstructural properties as presented in the thesis and solved by RG transformations on  $d = 2$  and  $d = 3$ . We have seen that ordering behavior is highly dependent on the level of frustration. Starting from the unfrustrated systems the drastic effects (but continuous as frustration is tuned continuously) such as destruction of orderings, emergence of reentrance of the phase diagrams, increasing chaos under rescaling have been observed. Furthermore, we have worked on different spin systems, i.e.,  $q$ -state clock spin-glass models in  $d = 3$ . We have shown that for odd  $q$ -state clock models, it is very improbable to sustain a spin-glass ordering due to high ground-state entropy induced by having many similar configurations to satisfy AF interactions. On the other hand, we have obtained a new universality class for even  $q$ -state clock model spin glasses, exhibiting the identical asymptotic behaviors on spin-glass phase sinks. For both even and odd  $q$ -state clock models, when increasing the number of clock states  $q$ , we obtain the identical convergence of ferro-para and antiferro-para critical temperatures  $1/J_c$  and critical exponents  $y_T$ .

Chaos spread out on clusterings, appears to be a continuation of local frustration at growing length scales. Equivalence of the distribution of chaotic visits of interactions at a specific location under rescaling trajectories with the fixed distribution of interactions at all locations is in fact very meaningful. Different clusterings at different length scales, thus different portions of the system do not seem alike and dissimilarity is qualitatively equivalent when changing the scale or changing the location. We observe an increasing chaos in spin-glass phases under rescaling upon increasing the level of frustration.

In addition to that, dynamic processes in non-equilibrium systems are investigated with two specific examples. While our results contain an original perspective for the related fields themselves, in fact, similarities with spin-glass systems can be deduced when reaching towards the equilibrium state. In ESR theory, we have seen a relatively short relaxation times by the fact that system being paramagnetic such that having a zero magnetization at equilibrium state. Ferromagnetic systems are also expected to have very short relaxation times while our knowledge on criticality suggest that it takes infinite time to the equilibrium state when a

critical (second-order) phase transition is occurring (system has fluctuations at all length scales). On the other hand, in the second example where we have a bimetallic synthesis via atomic deposition process, we have seen that relaxation times are highly sensitive to the competition between energy barriers and the thermal energy. As discussed in the Introduction, spin glasses are also under the influence of non-equilibrium dynamics for a huge time window due to the complicated free energy landscape especially at low temperatures. However, for spin-glass systems, the perturbation out of equilibrium or a steady state have more drastical results such as changing the overall configuration of the whole system.

In this thesis, we have focused on equilibrium phase transitions in diverse spin-glass systems. Our results are hoped to be instructive to a great extent for simulational and experimental preparations and on understanding better the complex nature of spin-glass systems.



## VITA

Efe İlker was born in Istanbul on December 14, 1987. He completed his high school education at the French high school, Lycée Saint-Joseph (Istanbul) and then started his undergraduate education at Koç University in 2005. While his main career plan was to be an engineer, he decided to move on to physics, after taking physics classes from Assoc. Prof. Alkan Kabakçioğlu and Prof. A. Nihat Berker in 2006-2007. He started to work with Prof. A. Nihat Berker on XY spin glasses in 2008. During his undergraduate education at Koç University, he also worked in the laser research laboratory of Prof. Alphan Sennaroğlu. He received his B.Sc. degree in 2010 (including an English preparation class for one year) with 1st place graduation from the Physics Department. Subsequently in 2010, he started to work on doctoral studies with Prof. Berker at Sabancı University. In addition to his main focus on spin-glass theory and renormalization-group treatment on diverse systems, he has also collaborated with Prof. Sondan Durukanoglu Feyiz on atomistic scale analysis of nano bimetallic synthesis. As of August 2015, he has 3 published articles in the Physical Review E, one article in refereeing process, and several others in preparation. His current research interests are in condensed matter physics, statistical mechanics, and their applications to biological and other complex systems. After his doctoral degree, he will continue as a post-doctoral researcher at Case Western Reserve University, in Ohio, U.S.